SYNTHESIS AND CHARACTERIZATION OF GeO_2-SiO_2 WAVEGUIDES

BY

DIN-GUO CHEN

A DISSERTATION PRESENTED TO THE GRADUATE SCHOOL
OF THE UNIVERSITY OF FLORIDA IN PARTIAL FULFILLMENT
OF THE REQUIREMENTS FOR THE DEGREE OF
DOCTOR OF PHILOSOPHY

UNIVERSITY OF FLORIDA

1991

ACKNOWLEDGEMENTS

I would first like to express my deepest appreciation and gratitude to my academic advisor, Dr. Joseph H. Simmons, who offered me the opportunity to work in his group several years ago and allowed me to work on various exciting research projects. His guidance, advice, patience and continued encouragement through the past few years have been indispensable. I am also indebted to Kate Simmons, for her assistance and encouragement. Much gratitude must be accorded to the members of my supervisory committee, Drs. D.B. Tanner, J.J. Mecholsky, D.E. Clark, and K.S. Jones, for their helpful discussions and suggestions concerning the work. I would also like to acknowledge Drs. G.I. Stegeman and W.E. Torruellas for conducting THG measurements on my samples.

I would like to thank Dr. Romulo Ochoa for his helpful discussion and assistance with Raman and all other matters. Special thanks are due to Dr. H.J. Cheng for his helpful suggestions and discussions on waveguide characterization. Appreciation also goes to all my friends and colleagues for their ever-present assistance.

My sincere gratitude goes to my family, especially my wife and children for their sacrifice and understanding in supporting me throughout this study.

TABLE OF CONTENTS

ACKNOWLEDGEMENTS ii

ABSTRACT v

CHAPTERS

I. INTRODUCTION 1

1.1 Importance of GeO_2-SiO_2 Waveguides 1
1.1.1 Materials for Optical Fibers 1
1.1.2 GeO_2-SiO_2 Waveguides 4
1.2 Literature Review 8
1.2.1 The Basic Concepts of Waveguiding . . 8
1.2.2 Review of the Progress of Integrated Optics 21
1.2.3 Sol-Gel Processes 24
1.2.4 Low Pressure Chemical Vapor Deposition(LPCVD) Process 31
1.2.5 Photosensitive Response in GeO_2-SiO_2 Waveguides 34
1.2.6 Frequency Doubling in Glass Waveguides37

II. RESEARCH OBJECTIVES

2.1 Statement of Problem 40
2.2 Significance of Present Study 41

III. EXPERIMENTAL

3.1 Thin Film Preparation 44
3.1.1 Sol-Gel Method 44
3.1.2 LPCVD Method 52
3.1.3 Other methods 54
3.2 Characterization 62
3.2.1 Infrared Spectroscopy 62
3.2.2 Thermal Analysis 63
3.2.3 ICP Solution Analysis 63
3.2.4 X-ray Photoelectron Spectroscopy . . 64
3.2.5 Electron microscopy 65
3.2.6 X-ray Diffraction Measurement 66
3.2.7 UV/VIS/NIR spectroscopy 66
3.2.8 Ellipsometric Measurement 66

3.2.9 Raman Spectroscopy 74
3.2.10 Planar Waveguide Characterization . . 78
3.2.11 Third Harmonic Generation(THG) Measurement 92

IV. GeO_2-SiO_2 FILMS BY SOL-GEL METHOD 101

4.1 Introduction 101
4.2 Results and Discussions 102
4.2.1 Synthesis of Alkoxide Precursors . 102
4.2.2 Sol Preparation 105
4.2.3 Film Formation 109
4.2.4 Thermal Analysis 112
4.2.5 Consolidation of the Film 115
4.2.6 Microstructure of the Film 129
4.2.7 Vibrational Spectroscopy 132

V. GeO_2-SiO_2 FILMS BY LPCVD METHOD 142

5.1 Introduction 142
5.2 Results and Discussions 143
5.2.1 Film Formation 143
5.2.2 Microstructure of the Film 147
5.2.3 XPS Chemical Analysis 151
5.2.4 UV/VIS Spectroscopy 155
5.2.5 Vibrational Spectroscopy 158

VI. PLANAR WAVEGUIDE CHARACTERIZATIONS 164

6.1 Introduction 164
6.2 Mode Index Measurement 166
6.3 Propagation Loss Measurement 177
6.4 Mode Profile Measurement 184

VII. NONLINEAR OPTICAL MEASUREMENTS 204

7.1 Introduction 204
7.2 Semi-Empirical Model: BGO Equation . . . 205
7.3 Third Harmonic Generation(THG) Measurement 213

VIII. SUMMARY AND CONCLUSIONS 228

REFERENCES 234

BIOGRAPHICAL SKETCH 246

Abstract of Dissertation Presented to the Graduate School of the University of Florida in Partial Fulfillment of the Requirements for the Degree of Philosophy

SYNTHESIS AND CHARACTERIZATION OF GeO_2-SiO_2 WAVEGUIDES

by

Din-Guo Chen

August, 1991

Chairman: Dr. Joseph H. Simmons
Major Department: Materials Science and Engineering

The growing use of single mode fibers in local-area networks and customer premises networks will increase the need for passive optical components, such as branching devices, mixers etc. Integrated optical devices are potentially ideal for these applications, provided that they can be made compatible with single mode fibers. The use of GeO_2 as the core dopant and SiO_2 as the substrate ensures that these waveguides will have virtually identical characteristics to single mode fibers. Additionally, glasses in the form of waveguides have recently been used to study various nonlinear optical phenomena, which provide great potential applications such as data storage and information processing.

The present study has for the first time demonstrated the feasibility of employing both sol-gel multiple dip-coating and low pressure chemical vapor deposition(LPCVD) in the production of GeO_2-SiO_2 waveguiding films with various germania contents. The thin film characteristics were studied by

various analytical techniques(e.g. ellipsometry, waveguiding Raman spectroscopy, FTIR, XPS, SEM/TEM). The composition dependence of the linear refractive index of GeO_2-SiO_2 films follows that predicted by the Lorentz-Lorenz model. Vibrational spectroscopy revealed the existence of Si-O-Ge linkages in GeO_2-SiO_2 glass network. The addition of GeO_2 in SiO_2 caused a decrease in the size of both the D1 and D2 defect bands in the SiO_2 Raman spectra. The structure of the LPCVD film appears to be dominated by D1 and D2 defect bands.

Using a three-prism loss measurement technique, the propagation losses were found to be 3.31 dB/cm and 2.59dB/cm for sol-gel and LPCVD films, respectively. These losses are attributed to various scattering processes in the films. The mode indices of the waveguide were measured using a prism coupling technique. The measured mode indices were found to agree with the calculated value based upon a step-index profile assumption. The theoretical electromagnetic field distribution profiles for a step-index planar waveguide has been calculated and compared to the experimentally measured mode profiles using a near field technique.

The nonlinear refractive indices of the sol-gel films (GeO_2-SiO_2, and GeO_2-TiO_2) were measured using a third-harmonic-generation(THG) interferometry fringe technique. The relation between n_{2THG} and n_l was found to follow that predicted by the empirical BGO model. An additive model was used to calculate the linear refractive indices, Abbe numbers, and n_l dispersion curves of the films.

CHAPTER I

INTRODUCTION

1.1 Importance of GeO_2-SiO_2 Waveguides

1.1.1 Materials for Optical Fibers

The transmission and processing of signals carried by optical beams rather than by electrical currents or radio waves has been a topic of great interest ever since the early 1960s, when the development of the laser first provided a stable source of coherent light for such applications. There are many aspects required for optical fiber materials. The major features to be considered are

(1). Optical loss properties: intrinsic loss properties and potentiality of extrinsic loss reduction are of vital importance.

(2). Refractive index control: precise control of refractive index profile in radial direction and the reduction of index fluctuation along the axial direction are necessary.

(3). Shape control: cross-sectional shape and size, the

surface finish and the fluctuation of the cross-sectional dimensions along axial direction of fibers strongly affect the transmission characteristics of the fibers.

Laser beams can be transmitted through the air, but atmospheric variation causes undesirable changes in the optical characteristics of the path from time to time. From the historical view point, many kinds of light-transmission waveguides were studied for their practical applications. These materials cover gas, liquid, crystal and glass. Many attempts to produce gas waveguides have been made [Ber64, Eag62]. The fatal defect in the use of gaseous materials is the difficulty of controlling the refractive index.

Some liquids are also low loss media for optical waveguides [Mar64, Ston72]. However, the refractive index of a liquid changes considerably so that it is fairly hard to maintain the precise waveguide characteristics. Furthermore, only step-index waveguides can be fabricated for practical use.

Solid state materials have stronger interaction with light waves than gases and liquids. Therefore, in general, the transmission loss may be higher; however, the optical properties are much more stable compared to gases and liquids.

Solid state materials have strong absorption at ultraviolet wavelength and infrared wavelength regions, which

are attributed to electronic transitions and molecular vibrations, respectively. These absorption peaks affect the absorption loss in the visible and near-infrared wavelength regions. In order to find low-loss materials, it is better to select materials whose strong absorption wavelengths are far from each other,i.e. having a wider transmission window.

Solid state materials are classified into two groups: crystalline state and amorphous state. The optical characteristics of the two states are quite different, even if the atomic composition is the same. Crystalline materials, such as quartz, sapphire, and alkaline halides have essentially very low loss compared to amorphous materials, because Rayleigh scattering loss, which originates from the density fluctuations, is less than one-tenth that of amorphous materials. Therefore, it can be said that the best materials may be found in single crystals from the viewpoint of intrinsic loss. However, high speed crystal growth or mass production of single crystal fibers is very difficult [Tang80, Bri80, Mim80, Oka80], and, moreover, the refractive index control of crystalline materials is also difficult. High doping of a refractive index modifier to the host crystal sometimes makes it difficult to grow a large single crystal. Furthermore, as-grown crystals have specific crystal surfaces, this leads to roughness on the surface and core/clad interface of the waveguide introducing a large scattering loss. The major loss increase in polycrystalline materials is caused by

light scattering at the grain boundary. The scattering intensity is very strong. Therefore, the transmission loss of polycrystalline waveguide is larger than expected from the intrinsic material property.

Amorphous materials are ideal for optical waveguides, because some glasses are highly transparent in visible and infrared wavelength regions. These glasses permit comparatively easy fabrication of fibers without introducing extrinsic scattering sources such as specific crystal surface roughness or grain boundary. Moreover, the refractive indices of these glasses can be easily controlled by changing the constituent composition, which does not severely affect the glass formation condition. Rayleigh scattering loss, originating from the density and composition fluctuations of amorphous materials, is larger than that of crystalline materials. However, the Rayleigh scattering loss is much smaller than the loss caused by grain boundary scattering in polycrystalline materials.

1.1.2 GeO_2-SiO_2 Waveguides

Oxide glasses, especially silicate glass, have high transparency in the visible and near-infrared wavelength region. Chemical and mechanical durabilities are also high. The refractive index of silicate glass can be changed easily by doping with other oxides such as GeO_2, Al_2O_3, and TiO_2. Furthermore, the raw materials are relatively cheap.

Therefore silica glass is one of the most suitable materials for low loss optical waveguides and has been widely used in various optical technologies today.

With regard to the possible refractive index modifiers that can be used in fabricating low-loss waveguides, most transition metal oxides in oxide glass introduce strong absorption in the visible and near-infrared wavelength region. Therefore, transition metals should be removed from the waveguide materials, in order to make low-loss waveguides. Some compounds of S, Se, Te, and P tend to form colloids, which may cause coloration of the materials; therefore, they are not preferable as waveguide material either. Alkali metal oxides are sometimes used to decrease the glass softening temperature. Chemical durability of the glass containing alkali metal oxides is comparatively poor, because alkali ions in the glass dissolve in water. The use of alkali-metal and alkaline-earth metal and heavy metal atoms increases the difficulty of reducing the possible transition metal contaminants to low levels.

The kinds of oxides suitable for making low-loss waveguides are limited strongly by the reasons mentioned above. GeO_2 glass has an atomic structure similar to that of silica glass and has a strong absorption band at 11.4 μm [Bor69] due to the ν_3 vibration mode. The absorption peak for GeO_2 on the UV side is around 185nm[Yue82]; an absorption band at 245nm has been frequently observed, which is attributed to

defect structures within the glass [Jac85]. Addition of germania to silica doesn't affect optical characteristics too much except for a slight shift of absorption peaks to longer wavelength. Therefore, germania-doped silicate glasses are the most important materials used in optical fiber today.

One of the major reasons why the high silica glass systems are the most preferable materials for optical fiber is that high purity glass can be easily prepared from chloride raw materials through vapor reaction and deposition processes. The vapor phase process has an important feature: the refractive index control or dopant concentration control is comparatively easier. It is also easy to make a precise control in shape and size of fiber preforms obtained.

Today, GeO_2 is used as a dopant to increase the refractive index of the silica core because it seldom produces light absorbing ions in the process of glass fabrication. The one disadvantage of using GeO_2 is that its vapor pressure at high temperatures is too high to control the concentration precisely. When GeO_2-SiO_2 glass is heated up to high temperatures, GeO_2 evaporates from the surface. Therefore, it is very difficult to make a transparent glass directly from the raw material vapors.

This difficulty was solved by the development of a two step process or soot process. The soot process is the method of making a transparent article, which includes vaporizing hydrolyzable compounds of silicon and doping element into a

flame of combustible gas to decompose the vapor and to form finely comminuted doped silica and then vitrifying the silica to a transparent body by subsequent heat treatment. There are three major practical soot processes for making preforms: Modified Chemical Vapor Deposition(MCVD) [Mac80], Outside Vapor Deposition(OVD) [Sch80], and Vapor-phase Axial Deposition(VAD) [Iza79]. High silica fibers are made by drawing down a preform, which has a structure and composition similar to that of the fiber to be obtained.

The difference between these three processes lies in the geometrical growth direction of the fine glass particles or soot. Glass particles are deposited on a substrate tube in the radial direction in case of MCVD and OVD processes. On the other hand, glass particles are deposited on a substrate rod in the axial direction in the VAD process. Another difference is the heat source. Although usually oxy-hydrogen gas flames are used for the chemical reaction, hydrocarbon gas flames such as CH_4-O_2, C_3H_8-O_2 or RF discharge gas plasma torches can be substituted for oxy-hydrogen gas flames.

The sol-gel method has been one of the promising methods for synthesizing high purity silica glass[Hen90, Sak80] which should be applicable to fiber optics[Han80]. In addition, the method has an advantage in saving energy over conventional CVD processes.

It has been shown that the method is also useful for the fiber optics application, using undoped silica glass [Sus82,

Mat84]. However, the processing of doped silica has not been successful because of poor transmission loss properties [Puy82]. The 8%GeO_2 doped SiO_2 fiber prepared from the preform made by the sol-gel method possesses a loss minimum around 22 dB/km at 830nm. The high overall loss was believed to be due to transition metal impurities from the germanium ethoxide precursor or from the residual water in the fiber. Both preform rods with uniform refractive index as well as gradient refractive index[Shi86] have been reported. Susa et al.[Sus90] also discussed the foaming problem upon heating glasses at high temperatures after consolidation of gels, which has to be solved before fabricating low-loss fibers.

1.2 Literature Review

1.2.1 The Basic Concepts of Waveguiding

Dielectric waveguides are the structures that are used to confine and guide light in guided-wave devices and circuits of integrated optics. Several examples of waveguide geometries are shown in Figure 1.1. A well-known dielectric waveguide is the optical fiber which usually has a circular cross-section as shown in (a). In contrast, the guides of interest to integrated optics are usually planar structures, such as planar films or strips, as shown in (b)-(d). The simplest dielectric waveguide is the planar waveguide shown in Figure 1.2, where a planar film of refractive index nf is sandwiched between a substrate and a cover material with lower refractive

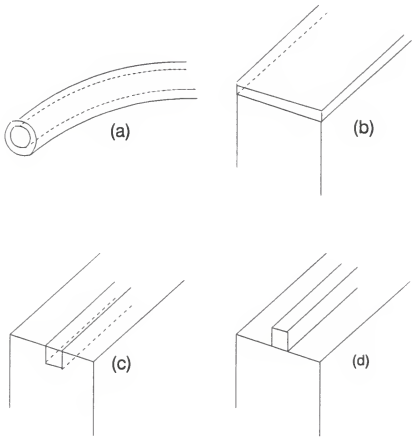

Figure 1.1 Examples of guided wave geometries. (a) fiber waveguide, (b) planar or slab waveguide, and (c) (d) channel waveguides.

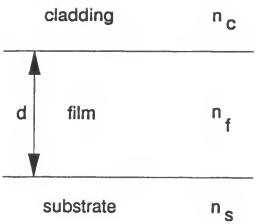

$n_f > n_s, n_c$

$\Delta n \approx n_f - n_s = 0.001 \sim 0.1$

$n_c = 1$ for air

$d \approx 1 \mu m$

Figure 1.2 Schematics of a planar waveguide.

indices n_s and n_c ($n_f > n_s > n_c$). Often the cover material is air, in which case $n_c = 1$. Typical differences between the indices of the film and the substrate range from 0.001 to 0.1, and a typical film thickness is 1 μm. The light is confined by total internal reflection at the film-substrate and film-cover interfaces.

Since light is a form of electromagnetic wave, its properties must be explained in terms of Maxwell's equations. Therefore the rigorous way to calculate the intensity and phase of a light wave is to derive the wave equation from Maxwell's equations and solve directly. However, because the wavelength of light is very short, it is often convenient for demonstration purposes to use the concept of a "light ray" and geometrical optics, or the ray equations, which are obtained by starting from Maxwell's equations and then taking the approximation $\lambda \Rightarrow 0$ (where λ is the wavelength). With the simplification of ray approximation, the refraction of the light at an interface separating two lossless, isotropic, homogeneous dielectric media of refractive index n_1 and n_2, as shown in Figure 1.3, can be described by Snell's law and Fresnel formulas, respectively.

When a coherent light wave is incident at an angle θ_1 between the wave normal and the normal to the interface. In general, the wave, having a complex amplitude **A**, is partially reflected and refracted. The exit angle θ_2 of the refracted wave C is given by Snell's law

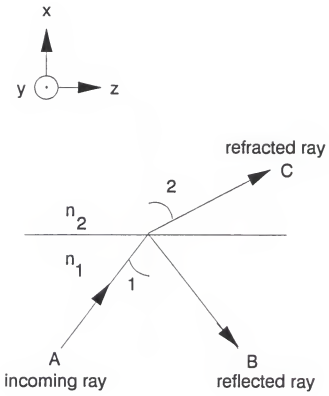

Figure 1.3 Ray picture of light at the interface of two media of different refractive indices.

$$n_1 \sin\theta_1 = n_2 \sin\theta_2 \tag{1.2.1}$$

The reflected wave has a complex amplitude **B** at the interface linearly related to **A** by a complex reflection coefficient **R**

$$B = R\,A \tag{1.2.2}$$

The reflection coefficient depends on the angle of incidence and the polarization of the light, and is given by the Fresnel formulas [Kni76]. For TE polarization(i.e. electric fields perpendicular to the plane of incidence spanned by the wave normal and the normal to the interface)

$$\begin{aligned} R_{TE} &= \frac{n_1 \cos\theta_1 - n_2 \cos\theta_2}{n_1 \cos\theta_1 + n_2 \cos\theta_2} \\ &= \frac{n_1 \cos\theta_1 - \sqrt{n_2^2 - n_1^2 \sin^2\theta_1}}{n_1 \cos\theta_1 + \sqrt{n_2^2 - n_1^2 \sin^2\theta_1}} \end{aligned} \tag{1.2.3}$$

The corresponding formula for TM polarization (with the magnetic fields perpendicular to the plane of incidence) is

$$R_{TM} = \frac{n_2\cos\theta_1 - n_1\cos\theta_2}{n_2\cos\theta_1 + n_1\cos\theta_2} = \frac{n_2^2\cos\theta_1 - n_1\sqrt{n_2^2 - n_1^2\sin^2\theta_1}}{n_2^2\cos\theta_1 + n_1\sqrt{n_2^2 - n_1^2\sin^2\theta_1}} \qquad (1.2.4)$$

At the critical angle of incidence, θ_c, transmission of the light wave into medium 2 ceases completely, and all the energy is totally reflected at the boundary; where

$$\theta_c = \sin^{-1}\left(\frac{n_2}{n_1}\right) \qquad (1.2.5)$$

When the input angle exceeds the critical angle, no light rays propagate into the medium 2; that is, there is no refracted ray. Region 2 then contains only an evanescent component which is guided along the boundary surface in the z direction. The totally reflected light has value $|\mathbf{R}|=1$, $\mathbf{R}$ is complex and a phase shift, ϕ, is imposed on the reflected light.

$$R = e^{(2j\,\phi)} \qquad (1.2.6)$$

According to the Fresnel formulas the phase shifts ϕ_{TE} and ϕ_{TM}

corresponding to the two polarization states can be expressed as[Kog79]

$$\tan\phi_{TE} = \frac{\sqrt{n_1^2 \sin^2\theta_1 - n_2^2}}{n_1 \cos\theta_1} \qquad (1.2.7)$$

$$\tan\phi_{TM} = \frac{\frac{n_1^2}{n_2^2}\sqrt{n_1^2 \sin^2\theta_1 - n_2^2}}{n_1 \cos\theta_1} \qquad (1.2.8)$$

This phase shift is dependent on the angle of incidence θ_1 and the refractive index of both media, n_1 and n_2.

Consider a three-layer system as in asymmetric planar waveguide structure, as shown in Figure 1.2. In general, it requires $n_f > n_s > n_c$ and two critical angles of interest, θ_s for total reflection from the film-substrate interface and $\theta_c < \theta_s$ for total reflection from the film-cover interface. When the angle of incidence θ is increased, three distinct cases will happen as shown in Figure 1.4[Kog79].

For small angles $\theta < \theta_s, \theta_c$, light incident from the substrate side is refracted according to Snell's law and escapes from the guide through the cover, see (a). There is no confinement of light, and the electromagnetic mode corresponding to this picture is called a "radiation mode".

When θ is increased such that $\theta_s > \theta > \theta_c$, the situation (b)

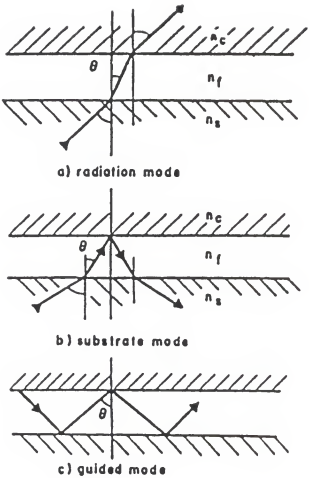

Figure 1.4 Zig-zag wave pictures for the radiation modes(a), the substrate modes(b), and the guided modes(c) in a slab waveguide[Kog79].

can be observed. The light incident from the substrate is refracted at the film-substrate interface, totally reflected at the film-cover interface, refracted back into the substrate through which the light escapes from the structure. In this case, there is no confinement either, and is called a "substrate radiation mode".

Finally, when θ is large enough that θ_s, $\theta_c<\theta$, the case (c) will occur, i.e. total internal reflection at both interfaces. The light, once it is inside, is trapped and confined in the film and propagates in a zig-zag path. This case corresponds to a "guided mode" of propagation.

An optical wave guided successfully by total internal reflections may be represented by bundles of rays called "modes". By using the idea of a mode, the phenomenon of light guidance can also be treated as a wave motion. The formation of a mode in a dielectric waveguide can be shown schematically as in Figure 1.5.

The physical picture of guided light propagation is that of light traveling in zig-zag fashion through the film; each ray represents an uniform plane wave from the wave point of view. More precisely, it is a picture of two superimposed uniform plane waves with wavenormals which follow the zig-zag path indicated in the figure and which are totally reflected at the film boundaries. These waves are monochromatic and coherent with angular frequency w, free-space wavelength λ, and they travel with a wavevector **k** in the direction of the

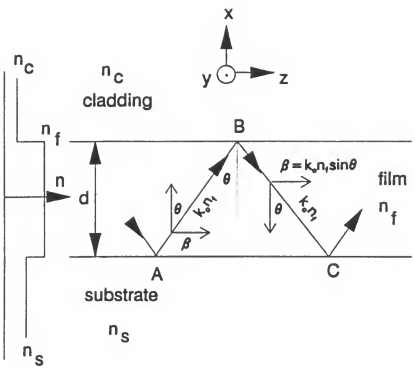

Figure 1.5 Ray diagram of a guided mode in the planar waveguide.

wave normal, This wave vector **k** of the wave within the film can be expressed as

$$\boldsymbol{k} = \boldsymbol{k}_o \, n_f \tag{1.2.9}$$

where the absolute value of $\mathbf{k}_o$ is

$$k_o = \frac{2\pi}{\lambda} = \frac{\omega}{c} \tag{1.2.10}$$

where k_o is the propagation (or phase) constant of the plane wave in a vacuum, ω is the angular velocity of light, and c the velocity of light in vacuum.

This plane wave can be decomposed into two component plane waves, propagating in the axial (or z) and transverse (or x) directions, as shown in Figure 1-5. the component of the propagation constant in the axial direction is β, that is

$$\beta = \frac{\omega}{v_p} = k_o \, n_f \sin\theta \tag{1.2.11}$$

On the other hand, the transverse component of the propagation constant γ can be given by

$$\gamma = \pm\, k_o\, n_f \cos\theta \tag{1.2.12}$$

As the ray travels through path A-B-C in Figure 1.5, it suffers phase shifts at both interfaces due to total internal reflection as well as a phase change while propagating inside the film. If the total accumulated phase change is an integral multiple of 2π, the phase front after total internal reflection at A as it advances to C comes in phase with the phase front which is reflected at C, resulting in a constructive interference. Under these conditions, the film supports a ray corresponding to a specific incident angle θ, a standing wave is established in the transverse direction therefore, the field distribution in the transverse direction does not change as the wave propagates in the axial direction. This transverse resonance condition can be represented as [Tie71, Kog79]

$$2k_o\, d\, n_f \cos\theta - 2\phi_s - 2\phi_c = 2m\pi \tag{1.2.13}$$

where d is the film thickness, m is an integer and the phase shifts ϕ_s and ϕ_c for TE mode(i.e the electric field polarization perpendicular to the plane of incidence) can be expressed in terms of film parameters

$$\phi_s = \tan^{-1}\left[\frac{\sqrt{(n_f^2 \sin^2\theta - n_s^2)}}{n_f \cos\theta}\right] \qquad (1.2.14)$$

$$\phi_c = \tan^{-1}\left[\frac{\sqrt{(n_f^2 \sin^2\theta - n_c^2)}}{n_f \cos\theta}\right] \qquad (1.2.15)$$

while for TM mode(i.e. the electric field polarization parallel to the plane of incidence)

$$\phi_s = \tan^{-1}\left[\left(\frac{n_f}{n_s}\right)^2 \left\{\frac{\sqrt{(n_f^2 \sin^2\theta - n_s^2)}}{n_f \cos\theta}\right\}\right] \qquad (1.2.16)$$

and

$$\phi_c = \tan^{-1}\left[\left(\frac{n_f}{n_c}\right)^2 \left\{\frac{\sqrt{n_f^2 \sin^2\theta - n_c^2}}{n_f \cos\theta}\right\}\right] \qquad (1.2.17)$$

For a given set of film parameters, the ray propagates at specific discrete angles (or sometimes none).

1.2.2 Review of the Progress of Integrated Optics

The guiding of light beams along dielectric layers, first realized in the early sixties [Mil69], has stimulated the growth of a new class of passive and active components

using light guided by films. By utilizing various masking and/or lithography techniques, a variety of integrated optical components capable of performing a wide range of operations on light waves have been realized. Because of their small dimensions, light weight and low-power requirements, it was then projected that such optical components could replace electrical circuitry in integrated electronic equipment. In addition, the optical elements would provide the advantages of greater bandwidth and immunity from electromagnetic interference. These advantages provided by integrated optics can benefit areas such as telecommunications, spectrum analyzer, gyroscopes, digital correlators, optical switches multiplexers, and signal processors etc. [Hal86, Car87, Hut88, Alf86, Gar86]. However, the major disadvantage of the optical integrated circuits is the high cost of developing new fabrication technology.

The research can be generally divided into two categories:

(1). Development of waveguide materials and fabrication processes.

(2). Development of new devices or new configuration for the existing devices.

A variety of waveguide materials such as polymers, fused silica, silicate glasses, lithium niobate, lithium tantalate, zinc oxide, III-V semiconductors etc., have been used to fabricate waveguides. The associated fabrication processes

includes ion diffusion, ion-exchange, ion-implantation and various thin film deposition methods, such as plasma polymerization, sputtering, dipping(or spinning), epitaxial layer growth etc.

Kaminow and Carruthers[Kam73] have used out-diffusion of Li ions to form waveguiding layers in $LiNbO_3$ and $LiTaO_3$ crystals. In-diffusion of various transition metal elements has been used by Schmidt and Kaminow[Sch74] to prepare low-loss planar waveguides in $LiNbO_3$. Low-temperature proton-exchange process has been used to fabricate stable low-loss $LiNbO_3$ waveguides by Suchoski et al.[Suc88]. Various researchers have fabricated glass waveguides with different ion-exchange processes on silicate glasses[And73, Iza72, Poy90, Ram88]. Schneller et al. have applied a proton-implantation process to create waveguiding layers in fused silica[Sch68]. Several polymer materials have been processed into different waveguide structures by solution-deposited method[Ulr72], plasma-polymerization method[Tie72, Vas72, Tie73], and Photo-induced polymerization process[Die90, Boo89]. Goell and Standley have reported using an RF sputtering technique to form a waveguiding layer of Corning 7059 glass on a microscope slide[Goe69].

In all these cases, the propagation loss of the waveguide and ease of fabrication have been the major criteria for accepting or rejecting a waveguide material. To date, Ti-indiffused $LiNbO_3$ waveguides and the various silicate glass

waveguides are two of the most important systems under studied.

1.2.3 Sol-Gel Processes

1.2.3.1 Background

The history of sol-gel processing begins in the 1800's with the studies by Ebelman [Ebe46, Ebe47] and Graham [Grah64]. These early investigations observed that the hydrolysis of tetraethylorthosilicate, $Si(OC_2H_5)_4$, at low pH resulted in the formation of SiO_2. It was recognized by Geffcken [Gef51] in the early 1930's that alkoxides could be used in the preparation of oxide films. This process was soon developed by the Schott glass company in Germany as reviewed by Schroeder [Sch69]. Around the same time, mineralogists became interested in the use of sols and gels for the preparation of homogeneous powders in studies of phase equilibria [Ewe35, Barr50]. This method was popularized in the ceramic community by Roy [Roy56, Roy69, McC71] for the preparation of homogeneous powders. They used this technique and synthesized a number of oxide compositions that cannot be produced by the traditional powder methods. The concurrent work of Iler [Ile55] and Stober [Sto68] revealed the importance of catalysts, alkoxide types and concentration, solution pH and reaction temperature as processing parameters.

During the past decade, an enormous growth of literature has been associated with the development of the sol gel

process. This was stimulated largely by the works of Phalippou and Zarzycki[Pha82] as well as Yoldas [Yol75]. They demonstrated the feasibility of preparing large ,dense, monolithic objects of silica and alumina, respectively. Sol-gel processing is a method for producing glass or ceramics from solutions of metal-organic or inorganic compounds through a series of chemical reactions (e.g. hydrolysis and condensation) which cause the formation of the polymeric species (or colloids) dispersed in solution(or called sol). This sol then gels into a three-dimensional network. The final products could be obtained after drying and densifying the gel. At the functional group level, three general reactions can be used to describe the sol-gel process:

(1). Hydrolysis versus esterification

$$\equiv M\text{-}OR + H_2O \;\langle===\rangle\; \equiv M\text{-}OH + ROH$$

(2). Alcohol condensation versus alcoholysis

$$\equiv M\text{-}OR + HO\text{-}M\equiv \;\langle===\rangle\; \equiv M\text{-}O\text{-}M\equiv + ROH$$

(3). Water condensation versus hydrolysis

$$\equiv M\text{-}OH + HO\text{-}M\equiv \;\langle===\rangle\; \equiv M\text{-}O\text{-}M\equiv + H_2O$$

where R is an alkyl group, C_xH_{2x+1}; M is metal such as Si or Ge.

Such a technology offers enormous opportunity for preparing crystalline ceramics and glasses with high purity,

chemical homogeneity, and novel composition and microstructure at relatively low temperatures. Applications for sol-gel materials cover optical, electronic, structural ceramics, and recently discovered ceramic superconductors, in the form of fibers, coatings, powders, and shaped monolithic parts [Uhl84, Bri88a].

1.2.3.2 Film formation

One of the most technologically important aspects of sol-gel processing is that, prior to gelation, the fluid sol or solution is ideal for preparing thin films by dipping, spinning, or spraying. Compared to conventional thin film forming processes, such as CVD, evaporation, or sputtering, sol-gel film formation requires considerably less equipment and is potentially less expensive. However, the most important advantage of this process is the ability to control precisely the composition and the microstructure of the deposited film, i.e. the pore volume, pore size, and surface area.

Scriven[Bet88] described the dip-coating process into five stages: immersion, start-up, deposition, drainage, and evaporation. Figure 1.6[Bri91] is a schematic representation of the steady state deposition stage of the dip-coating process. Dilute, non-interacting, polymer species that make up the coating bath are concentrated on the substrate surface by gravitational draining accompanied by vigorous evaporation

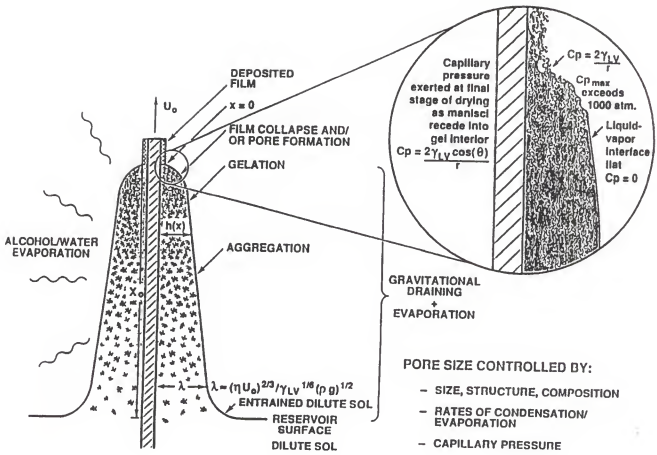

Figure 1.6 Schematics of the sol-gel film deposition during the dip-coating process[Bri91].

and further condensation reactions. Correspondingly, the viscosity progressively increases due to the increasing concentration and further condensation reactions promoted by the increasing concentration. This polymer growth process is believed to proceed similarly to a cluster-cluster aggregation model proposed by Meakin[Mea83]. Gelation occurs at the moment when the condensing network is sufficiently stiff to withstand flow due to gravity yet is still filled with solvent.Several factors distinguish structural evolution in films from that of bulk gels[Bri88b].

(1). Overlap of the deposition and evaporation stages establishes a competition between evaporation (which compacts the structure) and continuing condensation reactions (which stiffen the structure). In bulk systems, the gelation and drying stages are normally separated.

(2). Compared to bulk systems, aggregation, gelation, and drying occur in seconds to minutes during dipping or spinning rather than days or weeks.

(3). The short duration of the deposition and drying stages causes films to experience considerably less aging (crosslinking) than bulk gel. This generally results in a more compact dried structure.

(4). Fluid flow, due to draining, evaporation, or spin-off, combined with attachment of the precursor species to the substrate, impose a shear stress within the film during deposition. After gelation, continued shrinkage due to drying and further condensation reactions creates a tensile stress within the film. Bulk gels are not constrained in any dimension.

1.2.3.3 Attempts at making GeO_2-SiO_2 gel glass

As mentioned earlier, a lot of research has been conducted on making GeO_2-SiO_2 glass preforms for fiber drawing in the past few years. Puyane et al.[Puy82] first prepared silica-germania gels, containing up to 30wt% GeO_2. Sols were made up of 10% TEOS, 43% ethanol, 4% methanol, 33% H_2O, and a variable percentage of germanium ethoxide depending on the final oxide composition required.

Mukherjee[Muk84] prepared GeO_2-SiO_2 gels up to 80wt% GeO_2 with two gel preparation approaches:

(1). The starting compounds were TEOS (or TMOS) and germanium ethoxide. The general procedure consisted of the following steps: (a). mix alkoxysilane with three times its volume of anhydrous ethanol at 40°C. (b). partial hydrolysis at 40°C with 1 mole water per mole of silicon alkoxide, acidified with HCl (0,003 mole per mole $Si(OR)_4$), stir for two hours at 40°C, pH=2. (c). cool to room temperature and add

dilute ethanolic solution of germanium ethoxide, stir for 0.5 hour to 1 hour at room temperature. (d). add 4 moles of H_2O(diluted with ethanol) per mole of $M(OR)_4$. (e). stir at room temperature for 0.5 to 1 hour then cast for gel formation.

(2). The starting compounds were TMOS and germanium ethoxide. The general procedure consisted of the following steps: (a). mix TMOS with methanol at room temperature. (b). add aqueous NH_4OH solution (0.0002 mole NH_4OH per mole TMOS and 1 mole H_2O per mole TMOS). (c). stir for 0.75 hour at room temperature, pH=8. (d). add ethanolic solution of $Ge(OC_2H_5)_4$ and stir for 0.25 to 0.5 hour. (e). add water diluted with ethanol, 4 moles per mole M(OR)4, mixed with 0,0001 mole NH_4OH per mole alkoxide. (f). stir for 0.25 to 0.5 hour at pH=7. (g). cast for gelation.

Consolidated samples could not be produced with these methods. Crystallization of α-cristobalite phase in high silica gel and GeO_2 hexagonal phase in gels containing GeO_2 larger than 56wt% were observed.

Preparation of graded-index(GRIN) GeO_2-SiO_2 glasses by sol-gel method was reported by Shingyouchi et al.[Shin86]. The wet gel was prepared by using TMOS, germanium ethoxide, ethanol, water, and use HCl as catalyst. The gel was then leached in a water bath, followed by washing, drying, and the

subsequent heat-treatment.

Shibata et al.[Shi86] fabricated GeO_2-SiO_2 core optical fibers by using TEOS and germanium butoxide as starting compounds. The starting compounds were diluted with ethanol of commercial grade, and ammonium hydroxide was added as catalyst. Pure silica cladding was formed on the GeO_2 doped SiO_2 core glass by a conventional VAD process. The minimum optical loss of the fiber was measured as 9 dB/km at 1.07μm, which was attributed to the remaining OH impurity (>200ppm).

1.2.4 Low Pressure Chemical Vapor Deposition Process(LPCVD)

1.2.4.1 Background

The growth of thin silicon dioxide as well as doped silica layers by chemical vapor deposition has been one of the most important methods for semiconductor microelectronic device processing and has been investigated intensively [Ben87, Pav86, Tob80, wah75, Ker77]. These oxide layers are used mainly for interlayer dielectrics, protective, and passivation layers.

The reasons for the widespread acceptance of LPCVD for producing thin dielectric film are reduced processing cost and superior product quality that can be achieved, i.e. good uniformity, low particulate inclusions and low pin hole density [Mat80] .

Two basic parameters govern the deposition rate and uniformity of films grown by all CVD processes:

(1) rate of mass transfer of reactant gases to the substrate surface.

(2) rate of surface reaction of the reactant gases at the substrate surface.

The mass transfer of gases involves their diffusion across the slowly moving boundary adjacent to the substrate surface. The thinner this boundary layer and the higher the diffusion rate, the greater the mass transport that results [Ros77]. Surface reaction rates, on the other hand, depend mainly upon reactant concentration and deposition temperature. By lowering the pressure in the reactor, the diffusivity for LPCVD is several orders of magnitude (≈1000) higher than that of an atmospheric reactor. The LPCVD boundary layer is thicker by a factor of 3 to 10 which, however, does not offset the huge diffusivity difference. Thus low-pressure deposition conditions enhance mass transfer greatly, making close-spaced substrate positioning a practical and highly economical technique[Ker79]. Moreover, low-pressure deposition minimizes the formation of homogeneously gas nucleated particles, i.e. soot formation is depressed, and surface reactions(or heterogeneous reactions) become dominant which make high quality thin film deposition possible. Vertically-positioned substrates may eliminate codeposition of fine particles in the reactor into the film.

The key limitation of this process is its inherently low

deposition rate due to the fact that the operating total pressure is low (≈0.001 atm). However, higher deposition rates are attainable by using more concentrated reactive gases.

Several different reactant gases have been used to form silica in various CVD processes. The deposition temperature in the reactor determines the extent of oxide conversion efficiency, and sometimes the kinds of the reaction products formed. Some reactions are described as follows:

(1). Halide process(or soot process)

$SiCl_4 + O_2 \Longleftrightarrow SiO_2 + 2\ Cl_2$ T≈1000-1300°C

(2). TEOS process

$Si(OC_2H_5)_4 + O_2 \Longleftrightarrow SiO_2 + 8CO_2 + 10H_2O$ T≈700°C

(3). Hydride process

$SiH_4 + O_2 \Longleftrightarrow SiO_2 + 2H_2$ T≈300-500°C

$SiH_4 + 2O_2 \Longleftrightarrow SiO_2 + 2H_2O$ T≈600-1000°C

Among the reactions described above, the hydride process is a low temperature process, and the high concentration of bonded hydrogen can be eliminated in the oxides if deposition of the material is conducted in the appropriate temperature range. H-bonds in the SiO_2 films, existing in the form of Si-OH and Si-H, can produce recombination centers and cause deep

trapping[Kim88] for electronic applications, and cause undesirable optical absorption in the near-infrared range.

1.2.4.2 Deposition of GeO_2-SiO_2 Film by LPCVD Method

Conventionally, most of the GeO_2-SiO_2 binary systems were prepared by either a melting process or various soot processes for fiber preform applications.

There are very few studies of the preparation of GeO_2-SiO_2 glass by the LPCVD process. Huffman et al.[Huf86] attempted to prepare GeO_2-SiO_2 binary amorphous films by LPCVD method, using SiH_4, GeH_4, and O_2 as reactants. The $O_2/(SiO_2+GeO_2)$ ratio was 1:1, and a reactor pressure of ≈400 mtorr and deposition temperature of 430°C was used. The film was made to a thickness of about 3μm on stainless steel substrates. The film contains 3.6 mole% GeO_2. Owing to the low deposition rates, films containing higher GeO_2 content could not be made. The film quality was poor according to the reported SEM micrographs.

1.2.5 Photosensitive Response in GeO_2-SiO_2 Waveguides

It was first discovered by Hill et.al.[Hil78] that certain germania-doped glass optical fibers can show a photosensitive response to a single longitudinal mode Argon laser beam, leading to the formation of light-induced Bragg-matched phase grating. This phenomenon has been observed in both germanium silicate fibers[Hil78] and pure germania planar

waveguides[Yin83]. Despite a recent resurgence of interest in this phenomenon, there are still many questions surrounding the growth of these gratings. Two types of models have been proposed to explain this phenomenon.

An early experiment provided evidence that the process begins with two photon absorption(TPA) of the Argon laser beam [Lam81]. Later it was suggested by Meltz et.al.[Mel89] that this TPA results in the bleaching of an ultraviolet defect absorption band (~240 nm) of the glass, resulting in a modification of the index of refraction in the visible region of the spectrum. It was experimentally demonstrated by Simmons et al. [Sim90] that a similar wavelength dependent response for both the generation of Ge E' centers and the formation of photoresponsive gratings in germania-doped silica fibers. This supports the model [Mel89] for the grating formation whereby TPA of laser radiation into the UV bleachable absorption band (~240 nm) of an oxygen-deficient germania site creates hole traps, modeled as Ge E' center, which can be detected by Electron Spin Resonance(ESR). Recent work by Hand and Russell [Han90] suggested that new absorption bands(Ge(1):281nm, and Ge(2):213nm) are formed which contribute to the index change, perhaps even dominating over the simple effect of bleaching the 240nm band. These models are referred to as local bleaching models, in which the modification of the index of refraction of the glass is a function only of the local intensity of the light. This type

of model was demonstrated by Mizrahi et.al.[Miz90] to suit experimental results better.

The other type of model is a photorefractive-like model, as was suggested recently by Payne[Pay89], which involves carrier transport over macroscopic distances. As Mizrahi et.al.[Miz90] pointed out such a model predicts a modulation depth of the grating(in steady state) independent of the intensity of the laser that formed it. This is in sharp contrast with experiment[Lam81].

In the local bleaching model[Miz90b], a change in the real part of the dielectric constant, $\Delta\varepsilon(z,t)$, in the visible region of the spectrum with respect to the local intensity of the light in the waveguide, I(z,t), can be written as

$$\frac{\partial\Delta\epsilon(z,t)}{\partial t} = AI^2(z,t) \qquad (1.2.18)$$

where A is an material-related factor, which is related to the two photon absorption(TPA) cross-section of the 245nm band, as well as other material parameters which are at present unknown.

The absorption band at about 245nm is often attributed to an oxygen vacancy defect of the GeO_2[Gar58b, Yue82]. However, the precise microscopic origin of this band is still the subject of discussion[Sku84, Rau87, Tsa87]. Moreover, silica glass itself may also contribute two absorption bands near

248nm(~5.0eV), namely 247nm(5.02eV) for $B_{2\alpha}$ band and 240.7nm(5.15eV) for $B_{2\beta}$ band. Both of them were observed in oxygen-deficient samples and can be distinguished with photoluminescence measurement as well as optical absorption spectra obtained from samples heat-treated under different atmospheres[Toh89]. This has complicated the analysis of the 245nm absorption band for GeO_2-SiO_2 glass system.

1.2.6 Frequency Doubling in Glass Waveguides

The anomalous photoinduced second harmonic generation in germania-doped silica fiber was first observed by Osterberg and Margulis[Ost86]. A similar phenomenon was also later seen in pure GeO_2 waveguides[Kas89]. This phenomenon is still largely unexplained today.

Second harmonic generation(SHG) is one of the best known of the nonlinear optical effects. First observed in 1961 from a quartz crystal[Fra61], it is the basis of the most important nonlinear optical devices. But the observation of efficient second harmonic generation from "glass" was totally unexpected. Very general symmetry arguments prove that a material with a center of inversion symmetry cannot exhibit dipole-allowed second harmonic generation. A number of models have been proposed to explain this effect. Some models suggest that dipoles already present in the glass are somehow reoriented by interaction between infrared radiation and the glass to break its average inversion symmetry[Sto87, Les90].

Recent experimental evidence[Miz90a, Hib90a, Hib90b] of temperature dependence study, polarization study of SHG, and infrared erasure of self-organized $\chi^{(2)}$ gratings in germania-doped silica fiber argues against dipole orientation models, and favors carrier transport models. Several carrier transport models have been proposed by various research groups[And89, Que88, Dia89, Luc90]. These authors suggest that efficient SHG from an initially isotropic glass fiber implies a laser-induced modification in the glass structure, which involve some form of carrier transport, perhaps by a hopping process or by diffusion, leading to an internal d.c. electric field which acts on the $\chi^{(3)}$ of the glass and results in an effective $\chi^{(2)}$. The carriers might come from charges released from certain defect sites in the glass, and trapped at other sites due to the interaction between laser and waveguide. Tsai et.al.[Tsa89] have observed an apparent increase of the concentration of the Ge E' defect center in fibers which are conditioned for SHG.

The "defects" in the glass have been thought to play an important role in the process. Defect (as distinct from impurity) densities depend on such parameters as raw materials, processing method, processing temperatures, fiber drawing conditions, and atmosphere, which can vary between nominally similar fibers made by different manufacturers. This in part explains the problem of the conflicting or confusing experimental results found in the literature to be

due to the wide variety of optical fibers actually being studied in different laboratories around the world. Another source of the complication is that it would be desirable to conduct this study in waveguides that are always single mode at both the fundamental and the second-harmonic wavelengths, but standard telecommunication fibers are never single mode in the visible region.

CHAPTER II

RESEARCH OBJECTIVES

2.1 Statement of Problem

As mentioned earlier, the fabrication of high quality thin films and devices has received much attention in recent years. The increasing penetration of single mode fibers into local-area networks(LAN) and customer premises networks(CPN) will inevitably increase the requirement for *low cost* passive components, such as branching devices, mixers, etc.. Integrated optical devices are potentially ideal for these applications, provided that they can be made compatible with single-mode fibers. One of the factors which inhibits the widespread use of integrated optical(IO) devices is the incompatibility of the materials used (e.g. $LiNbO_3$, GaAs) with silica-based optical fibers. This leads to problems of Fresnel reflection and mode mismatch at the interface, and generally makes it very difficult to achieve low-loss permanent coupling between IO devices and optical fibers. The use of germania as the core dopant and silica as the substrate ensures that these waveguides will have virtually identical characteristics (optical, mechanical, thermal, etc.) to single-mode fibers. Moreover, glasses in the form of

waveguides, both fiber and planar, have recently been used to study various nonlinear optical phenomena, such as all-optical switching[Blo89] and spatial soliton propagation[Ait90]. Interesting phenomena such as photosensitive grating effect and anomalous photoinduced second harmonic generation (SHG), have been observed in various germanium silicate waveguides. The further understanding of these nonlinear optical phenomena will be of great scientific interest and may lead to an important technological impact in fields such as data storage and information processing.

2.2 Objectives of Present Study

The objectives of this work are to

(1). explore new and reliable methods to fabricate GeO_2-SiO_2 thin films which can be used as planar waveguides: The thin film characteristics were studied by various analytical techniques(e.g. ellipsometry, wave-guiding Raman spectroscopy, XPS, electron microscopy, etc.). Two thin film deposition methods were successfully applied to achieve this goal; the details of thin film deposition set-ups and procedures are described in Chapter III.

(a). Sol-Gel method: This involves synthesis of the germanium alkoxide precursors, sol preparation, film formation, and densification of the films. The details of this study and the various characteristics of the films are presented in Chapter IV. With this method, planar waveguides

of high GeO_2 content can be easily controlled and fabricated.

(b). Low pressure chemical vapor deposition(LPCVD) method: This involves investigation of appropriate film formation conditions(e.g. temperature, flow rate, pressure, etc.). By using this method, GeO_2-doped waveguides, with low GeO_2 contents, can be prepared at very low temperature compared to conventional methods. The details of this part of the study are described in Chapter V.

(2). characterize waveguide properties: The planar waveguides were characterized by a prism coupling technique. the propagation characteristics (number of modes supported and their propagation constant, propagation loss, etc.) were measured. Near-field mode profiles of the waveguides were measured and compared to the calculated results using a model calculations for planar waveguide with a step-index profile. The details of experimental set-up are given in Chapter III and the results are discussed in Chapter VI.

(3). measure nonlinear optical properties of the films: Two methods were used to characterize the nonlinear optical property of the films.

(a). Empirical approach: nonlinear optical coefficient n_2 can be related to Abbe number and linear refractive index through an empirical equation derived by Boling[Bol78]. The Abbe number of the films was calculated by using an additive

model developed by Huggins and Sun(Hug43).

(b). Third harmonic generation(THG) measurement: This is an ideal technique for the measurement of relatively small values of $\chi^{(3)}$, such as for thin films deposited on a much thicker substrate, as was the case in this study. By measuring the changes in the THG Interferometry Fringes, both the magnitude and the phase of $\chi^{(3)}$ can be obtained. The details of the experimental set-up and results will be described in Chapter III and VII, respectively.

CHAPTER III

EXPERIMENTAL

3.1 Thin Film Preparation

3.1.1 Sol-Gel Method

3.1.1.1 Synthesis of germanium alkoxides

Because of the extremely moisture-sensitive characteristics of the germanium alkoxides, all reactions and manipulations were carried out under dry nitrogen using standard Schlenk techniques[Shr86]. Ethanol, 2-propanol and n-butanol were distilled before use. 2-methoxyethanol and n-hexane were used as received.

Germanium ethoxide, $Ge(OC_2H_5)_4$, used in this study is prepared using an ammonia method described by Bradley et.al [Bra56], or is commercially available from Alfa Products. In a typical reaction, 25 g of germanium tetrachloride, $GeCl_4$ (Alfa), is initially mixed with 160 ml of hexane, 250 ml of ethanol is then added to the mixture with stirring to obtain a clear solution. Since $GeCl_4$ does not react with alcohol automatically, the reaction needs to be triggered by passing anhydrous ammonia, NH_3, through the reaction vessel to act as a proton acceptor. Germanium ethoxide forms according to the reaction expressed as follows:

$$GeCl_4 + 4\ C_2H_5OH + NH_3 \text{ ===> } Ge(OC_2H_5)_4 + NH_4Cl_{(ppt)}$$

This reaction is exothermic, so the bubbling of ammonia is continued until the reaction mixture cools down to room temperature. Precipitates of NH_4Cl are removed by filtration. The filtrate is then refluxed to expel excess ammonia and then is concentrated by removing the excess solvent and alcohol under ambient pressure. Vacuum distillation of the solution gives a colorless liquid of germanium ethoxide (boiling point: ~80 °C at 3 torr).

Various germanium alkoxides with higher alkyl groups, such as propyl, butyl, and methoxyethyl groups etc., were synthesized by an alcohol-interchange method[Bra56], using germanium ethoxide as a starting compound. In a typical reaction, the mixture of germanium ethoxide, higher alcohol, and hexane, in a molar ratio of 1:25:60, was refluxed in a column packed with glass beads as shown in Figure 3.1. An azeotropic distillation was followed to expel the azeotrope which contains 21 wt% of ethanol and 79 wt% of n-hexane and boils at 58.68°C at ambient pressure. The formation of a low boiling point azeotrope facilitates the reaction in the alcohol-interchange, which can be expressed as follows:

$$Ge(OR')_4 + 4\ ROH \text{ <===> } Ge(OR)_4 + 4\ R'OH$$

where R'is $-C_2H_5$, R is a higher alkyl group, such as $-C_3H_7$,

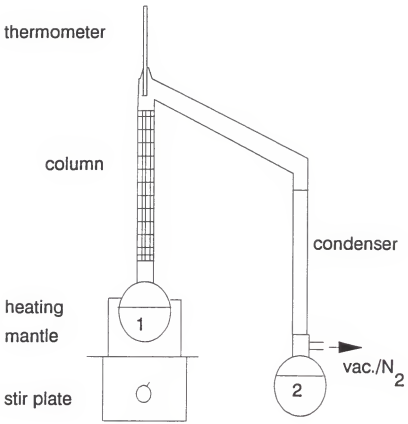

Figure 3.1 Experimental setup for alcohol-interchange reaction.

$-C_4H_9$, or $-CH_3OCH_2CH_2$ etc.. After removal of solvent, the germanium ester was vacuum distilled to produce high purity alkoxide for the preparation of GeO_2-SiO_2 sols. The replacement of the ethyl groups in germanium ethoxide with higher alkyl groups is expected to increase the stability of the germanium alkoxide against hydrolysis/condensation reactions due to steric effects. These modified germanium alkoxides are expected to increase the controllability of hydrolysis reactions during sol preparation and thereby enhance the possibility of obtaining stable and clear sols for the coating process.

3.1.1.2 Sol preparation

The GeO_2-SiO_2 sols were prepared by mixing a prehydrolyzed tetraethylorthosilicate, TEOS(Fisher), and germania sol together. The procedure for preparing the coating solution is shown in Figure 3.2. In a typical procedure, TEOS is dissolved in ethanol and then prehydrolyzed using water in the concentration range of 0.2-4 mole of water/mole of alkoxide. A small amount of hydrochloric acid, HCl, was added as catalyst. Reactions were allowed to continue for approximately one day after the water/HCl addition. Germania sols were prepared simply by dissolving the desired amount of germanium alkoxide, for the multicomponent sol of predetermined composition, in ethanol. The multicomponent sol was obtained by adding germania sol to silica sol under

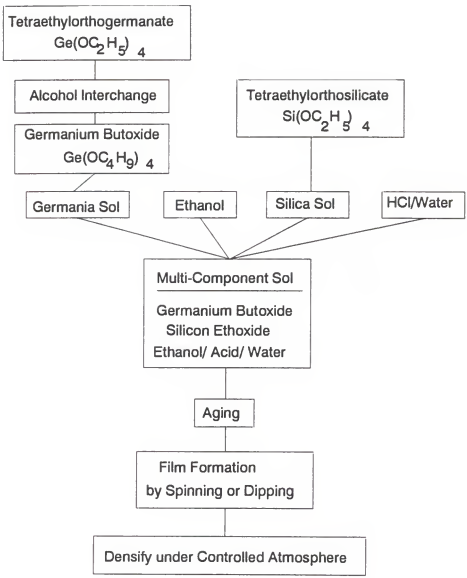

Figure 3.2 Flow diagram for the preparation of binary GeO_2-SiO_2 thin films using sol-gel method.

vigorous stirring. The coating solution is then aged for 8~12 hours before the coating process. Typical formulations for the preparation of various GeO_2-SiO_2 sols, using germanium methoxy-ethoxide as precursor, in the present study are given in Table 3.1. Clear and stable coating solutions may be obtained for an alkoxide content lower than 0.5 M, and water to alkoxide molar ratio(R) smaller than 3.

3.1.1.3 Film formation

Thin films were prepared by a dip coating method, in which a precleaned fused silica substrate was immersed into the sol followed by an immediate withdrawal in the vertical direction. Figure 3.3 shows a schematic of the dip-coater used in our laboratory. The withdrawal speed used in the current study was typically 2 to 7 cm/min.

After each coating, the film was dried in air for a short time before applying the next coating to allow for evaporation of the solvent from the film. After several dipping cycles, the film was then heat-treated in the temperature range of 300 °C to 1110°C to remove the organic residues as well as to densify the film. The thickness of the film can be built up by repeating the multiple dipping and firing cycles.

Several organic additives, such as polyvinylpyrolidone (PVP K-30, GAF Chemicals Co.), cp2(Daxad cp2, W.R. Grace & Co.), and hydroxypropylcellulose(HPC, Aldrich Chemicals Co.), were used in an attempt to adjust the viscosity of the coating

Table 3.1 Typical Compositions for the Preparation of GeO_2-SiO_2 sols.

SAMPLE	EtOH(ml)	TEOS(ml)	$Ge(OR)_4$(ml)	WATER (ml)	pH
10GS	20	2	0.4	0.3	1.58
30GS	20.5	0.9	0.7	0.2	3.63
50GS	21	0.3	0.6	0.1	1.91
75GS	19	0.5	2.6	0.1	1.07
100GS	21	0	1.1	0	2.71

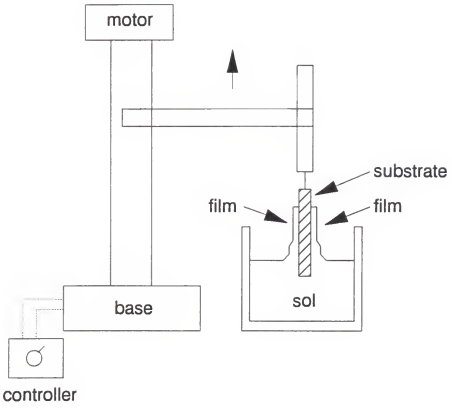

Figure 3.3 Schematic diagram of the dip-coating system.

solution to enhance thin film formation. The amount of organic additive used in the sol is usually less than 2 wt%.

3.1.2 LPCVD method

A Low Pressure Chemical Vapor Deposition System(LPCVD, Thermco) was used to prepare samples for this study. The system is shown schematically in Figure 3.4. In this study , ~1 mm thick high purity grade fused silica slides were used as substrates. The substrates were cleaned according to the following procedures:

(1) rinsed with soaped water, and immediately dried with N_2.
(2) sonicated in a deionized water bath and immediately dried with dry N_2.
(3) rinsed in electronic grade acetone and dried in dried N_2 gas jet.
(4) rinsed in absolute ethanol and dried immediately in dry N_2 jet.

The precleaned substrates were positioned vertically in a quartz boat with a separation of 3~5 mm between substrates. The boat was then placed in the center of the three-zone resistively-heated furnace, which acts as a hot wall reactor, and the temperature was allowed to equilibrate. Usually 30~40 substrates were loaded in the boat for each run.

In the apparatus used, the input gas flow rates were

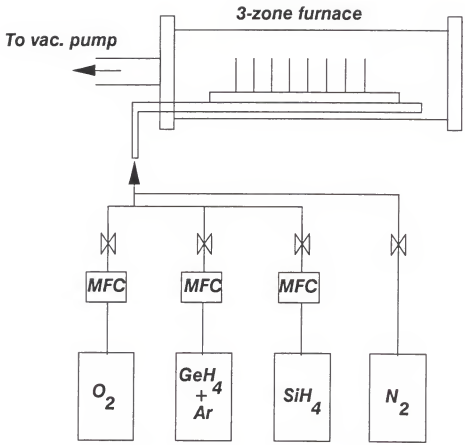

Figure 3.4 Schematic diagram of the low pressure chemical vapor deposition(LPCVD) system.

measured and controlled by mass flow controllers(MFC). The gases used for the GeO_2-SiO_2 film deposition were 0.2% GeH_4/Ar, SiH_4, and O_2. The reagent gases were introduced into the reactor independently through different injectors located below the quartz boat. Nitrogen gas was used to purge the reactor.

In a typical run, the reactor was first pumped down to a pressure below 50 mtorr, then the entire reactor was back-filled with nitrogen. Before starting deposition, the N_2 background atmosphere was replaced by O_2 gas and then the hydride gases were passed into the reactor at predetermined flow rates. Films were usually deposited at a reactor pressure below 500 mtorr. Table 3.2 shows the deposition parameters used for the GeO_2-SiO_2 film deposition in this study.

3.1.3 Other methods

According to the literature, many other thin film deposition techniques have been used to produce GeO_2-SiO_2 planar(or channel) waveguides. A brief description of each technique will be given in the following sections.

3.1.3.1 VAD soot particle method(or glazing method)

Mori and Shimizu[Mor82] have reported the use of a VAD soot process(using halide precursors) to deposit a doped silica glass particle(SiO_2-GeO_2-P_2O_5) layer as a core material

Table 3.2 LPCVD Deposition Parameters for the GeO_2-SiO_2 Film Formation.

Sample	Deposition temp.(^{O}C)	Pressure (mTorr)	Flow ratio $O_2/(MH_4)$	Dep. rate (A/min.)	Other
LP1	450	245±20	1.305	13.75	light brown
LP2	430	380±10	1.381	95.16	slightly hazy
LP3	450	330±10	1.494	95.67	clear

on a fused quartz substrate. In this process, silicon tetrachloride is used as the main raw material. Halides, such as $GeCl_4$, PCl_3, and BBr_3, are used as dopants which adjust the refractive index, softening temperature, and thermal expansion coefficient for the deposited glass.

The oxidation reactions take place in a three-zone furnace, which acts as an hot wall reactor. The gas flows and the substrates are positioned in a horizontal reactor configuration. The oxidation reactions are usually complete around 1200°C. The glass particles' deposition rate depends on the raw material supply, furnace temperature, and total O_2 gas flow rate. Since the deposition of these soot particles occurs via a thermophoresis process[Sim79, Wal80], the deposition rate depends most on the temperature gradient along the gas flow direction.

The deposited glass particle layer was made transparent by heating above the glass softening temperature. In this process P_2O_5 is usually added to lower the softening temperature of the core layer. For a glazing temperature above 1450°C, the waveguide loss around 1 dB/cm at 633 nm was achieved. The typical deposition rate of this process is 0.3~1 μm/min, therefore it is suitable for multimode waveguide fabrication. The fabricated waveguides can be further processed into various desired devices, by going through techniques such as masking, patterning with reactive-ion-etching, depositing cladding layer(e.g. SiO_2-B_2O_3) etc..

By using this process, the relative refractive index difference between core layer and fused silica substrate is typically less than 1%.

3.1.3.2 Flame-hydrolysis deposition(FHD) method

Flame hydrolysis deposition is one of the promising techniques for mass-production of cost effective integrated optical waveguide devices for telecommunication because of its compatibility with optical fiber technology. Several high-silica based waveguides have been fabricated by this method [Kaw83, Kom90, Max89, Bar90].

Kominato et.al.[Kom90] has fabricated SiO_2-GeO_2-P_2O_5-B_2O_3 waveguides on Si substrates. In this method, a gaseous mixture of $SiCl_4$-$GeCl_4$-BCl_3-PCl_3 of predetermined flow proportion is fed into an oxy/hydrogen torch. Fine glass particles synthesized by flame hydrolysis are deposited on the substrates placed on a turn table. During the deposition, the torch transverses the table repeatedly in the radial direction.

Small amounts of BCl_3 and PCl_3 are needed in the raw material gas composition to lower the softening temperature of the synthesized glass particles. The refractive index of the glass particles is controlled by the $GeCl_4/SiCl_4$ flow ratio. After the deposition, the substrates with porous glass layer are heated up to 1250°C for one hour in an electric furnace for densification. Deposition parameters have to be optimized

to obtain the proper glass composition, particle sizes, and packing, in order to facilitate the subsequent sintering step to achieve bubble free, transparent, low-loss waveguides without warping the substrate. A typical refractive index difference between core layer and the substrate is 0.2-1%. The propagation loss of the waveguides can be as low as 0.01~0.03 dB/cm at 1.55 μm. The typical deposition rate of this process is as high as ~1 μm/transverse.

3.1.3.3 Plasma-activated chemical vapor deposition(PACVD) method

Nourshargh et.al. used a plasma activated technique to produce GeO_2-SiO_2 and Si_3N_4 waveguides[Nou86, Nou89]. Because it is a plasma process, the introduction of a wide range of dopants into the silica guide is possible. Like other halide CVD processes, this method uses $SiCl_4$, $GeCl_4$, and O_2 as reactants. The reactor consists of a heated reaction zone maintained at a low pressure(≈0.75 Torr), into which are fed vapors of $SiCl_4$, $GeCl_4$, and oxygen through independent injectors from one end of the reactor. Ar gas is used to purge the reactor and to form the plasma, because of it is easily ionizable. A microwave generator(≈500 W at f=2.45 GHz) is used to excite a plasma in the reaction zone. A fused silica substrate is resistively heated and situated horizontally within the plasma region. Over the surface of the substrate, a layer of glassy doped silica is deposited.

Because this is a low pressure process, formation of particulates is avoided and homogeneous waveguiding layers are grown on the substrate by oxidation of the halide reactants. The detailed reaction mechanisms are not well understood.

The refractive index of the film can be varied by adjusting the ratio of the flow rates of $GeCl_4$ and $SiCl_4$. The thickness of the deposited layer is a function of both the deposition time and total chemical flow rates. The waveguides may be fabricated at a temperature ranging from 1100°C down to room temperature. Typically a waveguide prepared at 1100 C with the flow rates of O_2 through the $SiCl_4$ and $GeCl_4$ bubblers being 50 and 30 sccm respectively. The deposition rate is around 0.5 μm/min and a refractive index change about 0.011 was reported. The propagation loss is about 0.3 dB/cm at 0.633 μm.

This technique is capable of operating at low temperatures(≈400°C), however the waveguides produced at low temperatures possess a higher loss rate(~3 dB/cm).

Single mode pure GeO_2 waveguides were successfully deposited at a deposition rate of 0.03 μm/min and with a loss of approximately 1~2 dB/cm.

3.1.3.4 Reactive sputtering method

Both GeO_2-SiO_2 and pure GeO_2 waveguides have been prepared by using rf reactive sputtering deposition technique [Yin82, Hua85]. In this method, gases Ar and O_2 are introduced into

the vacuum chamber through the control of two gas flowmeters. Proper flow ratio between Ar and O_2 is needed to compensate for the inherent oxygen-deficient characteristic of the oxide films prepared by this vacuum deposition technique. With insufficient O_2 present in the vacuum chamber during film deposition, a highly-reduced film with a dark yellow appearance will be obtained.

To start the deposition process, the sputtering system is pumped down to a pressure in the region of 4x10-6 Torr and then backfilled with gases of Ar and O_2(O_2/Ar=1:1) to a total gas pressure of 2x10-3 Torr. Colorless low-loss GeO_2 thin film optical waveguides were prepared using rf reactive sputtering with a GeO_2 target and a low deposition rate (< 12.7 Å/min). The deposited films were annealed at 250°C for 6 hours. Films with a thickness up to 3800Å have been prepared with a waveguide attenuation of <0.7 dB/cm at 0.6328μm. The average refractive index of the GeO_2 films was measured to be 1.6059 at λ=5461Å by an ellipsometry technique.

3.1.3.5 Laser-induced CVD method

Photoinduced chemical vapor deposition has been used to form various kinds of films[Sol81, Boy82, Joh82, Sol83], including GeO_2-SiO_2 glass films[Tat86]. In this method, a pulsed 193nm ArF excimer laser provided a rectangular beam focused by a cylindrical lens telescope. The laser was operated at a 3 Hz repetition rate. This optical setup

provided a sheet of photons parallel to and at a small distance(typically 1mm) above the SiO_2 substrate surface. Substrates were positioned horizontally and were maintained at temperatures between 200 to 300°C by resistance heating. Gaseous reactants were 5% SiH_4/N_2, 5% GeH_4/N_2, and pure N_2O. The input window was purged with N_2 or He gas to prevent opaque deposition from forming, but the output window was not purged. Typical gas flow rates used for the deposition are Si source:200 sccm, Ge source: 0~50 sccm, N_2O: 1000~1500 sccm, N_2:800~1500 sccm, and He:800~2000 sccm. In a typical run, the partial pressure of N_2O ranges between 4 to 8 Torr.

The flow ratio of the reactant gases was determined based upon a consideration of the absorption cross-section of the laser light and the quantum yield of the photodissociation of each reactant used. Germane gas appears to have a similar cross-section to N_2O, and has a nearly ten times larger cross-section compared to that of silane gas. N_2 is almost "transparent" in this reaction. Furthermore, based upon these consideration, it is believed that SiO_2 is mainly produced by a direct oxidation reaction between SiH_4 and photodecomposed oxygen from N_2O. On the other hand, GeO_2 is generated by a reaction between photodecomposed oxygen from N_2O and Ge atoms from GeH_4. Therefore, in this deposition method, it is thought that the GeO_2-generating process is limited by the GeH_4 supply and that the SiO_2-generating process is limited by the O supply.

With this method single-mode GeO_2-SiO_2 waveguides have been prepared and a propagation loss as low as 1 dB/cm at 0.6328μm for low GeO_2 doped film was achieved. However, the propagation loss increases drastically for higher GeO_2 content films.

3.2 Characterization

3.2.1 Infrared Spectroscopy

Fourier-transformed infrared(FTIR) spectroscopy (Nicolet 20SXB FT-IR Spectrometer) was used to examine the synthesized alkoxides, GeO_2-SiO_2 gels and the thin film samples.

Transmission spectra of germanium alkoxides were obtained using a liquid cell(circle cell, Spectra Tech Inc.) with a ZnSe crystal which gives a transmission range from 4000 to 600 cm^{-1}. The spectra were obtained in a nitrogen atmosphere with 32 accumulation scans.

Transmission spectra were also obtained from the GeO_2-SiO_2 gels, heat-treated at different temperatures, using a diffuse reflectance stage(Spectra Tech Inc.) and 128 accumulation scans. The gel was ground to fine powder, packed loosely and leveled to the top of the stage for the measurement.

The transmission spectra of thin films produced from both LPCVD and sol-gel methods were obtained by using an attenuated total reflectance(ATR) stage(Spectra Tech Inc.) with a KRS-5 crystal(a mixed crystal of ThI_2-$ThBr_2$ eutectics). The KRS-5 crystal was sonicated in a methanol bath for ten minutes and

dried in a N_2 jet before use. Each thin film sample was cleaned with ethanol and held against the crystal for the measurement. 128 scans were used to obtain each spectrum.

3.2.2 Thermal Analysis

Thermal behavior of the gels, including the behavior of organic burn-out, was studied using differential thermal analysis(DTA), and thermogravimetric analysis(TGA)(Model STA-409, Netzsch Inc., Exton, PA.). The gels were dried at 120°C under vacuum for 8 hours and ground to fine powder. Powdered samples were preferred in this study not only to assure a good thermal contact between sample and crucible to increase the accuracy of DTA measurement, but also to ease drying and removal of physical adsorbed water which might be easily trapped within the pores in a bulk sample. For these measurements, 20 mg of the sample was placed in an Al_2O_3 crucible and heated up to 900°C in O_2 atmosphere at a heating rate of 5°C/min.

3.2.3 ICP Solution Analysis

Inductively coupled plasma(ICP) emission spectroscopy (Instrumentation Lab. Plasma 200) was used to study the composition of the gels prepared in present study. After removing excess solvent from the gel, solution samples were prepared by dissolving a predetermined amount of wet gel in 100 ml of deionized water. A few drops of hydrofluoric

acid(HF) was added for dissolving gels of lower germania content, e.g. 10GS. The solution was then diluted for the measurement. Some common contaminants of the silicate system, such as Na, Mg, Al, Fe, and Cu, were analyzed to check the purity of the gels. All the samples and standard solutions were prepared just before conducting the measurement.

In the measurement, the solution sample was fed at a constant rate into the system by a peristaltic pump. The solution was then atomized by a nebulizer and sprayed through an Ar plasma area, sustained by a rf coil. The electrons of the elements in the solution were excited by the plasma, followed by various atomic transition processes which emit characteristic photons corresponding to the excited state energy structure of different elements. The light was detected by an assembly of monochromater and photomultiplier tube(PMT).

3.2.4 X-ray Photoelectron Spectroscopy(XPS)

XPS(Perkin-Elmer PHI 5100 ESCA System) was used to analyze the composition of the thin films prepared by both sol-gel and LPCVD processes. A magnesium anode(Mg $K\alpha$=1253.6 eV) was used as X-ray source. Photoelectrons were collected at a take off angle of 45° and spatially-dispersed with a hemispherical electron energy analyzer and detected with a multichannel detector.

All of the samples were examined in the survey scan,

which is the low resolution high sensitivity mode, with a pass energy of 89.45 eV, a resolution of 0.35 eV/step, and an accumulation time of 50 ms/step, to determine whether there were any impurities present on the analyzed surface after achieving a vacuum of 10^{-9} Torr. The regions of interest were studied with high resolution multiplex scans, with a pass energy of 8.95 eV, a resolution of 0.05 eV/step, and a accumulation time of 100 ms/step. The peak areas of Ge3d and Si2p band were calculated to represent the atomic concentrations of Ge and Si respectively in the film.

3.2.5 Electron Microscopy

Scanning electron microscopy(SEM) (JOEL JSM-6400 Scanning Microscope) was used to study the surface morphology of the waveguides.

Transmission electron microscopy(JEOL 200CX TEM) was used to investigate the microstructure of the films. Plane samples were prepared for this study by mounting the sample on a fused silica slide with crystal bond. The sample was then polished from the side of the substrate to a thickness of ~150 μm. Several disk samples were cut from the polished thin sample. The disk was then dimpled(Dimpler, VCR Group, San Francisco, CA) to a thickness of around 10 μm. An ion-milling(Gatan Dual Ion Mill Model 600) step was followed to perforate the sample for TEM observation. Selected area electron diffraction (SAD) was used to study the possible formation of

small crystallites in the film.

3.2.6 X-ray Diffraction(XRD) Measurement

Phase identification was performed using room temperature X-ray powder diffraction with Cu Kα radiation (Phillips APD 3720 X-ray Diffractometer). The Cu Kα radiation was generated using a fine focus tube and a graphite monochromator at 40 KV and 20 mA. 2θ peaks between 5° to 100° were scanned at a rate of 3°/min.

3.2.7 UV-VIS Spectroscopy

Optical characteristics of the LPCVD thin films in the ultra-violet range were investigated by using a UV-VIS-NIR spectrophotometer (Perkin-Elmer Lambda 9).

3.2.8 Ellipsometric Measurements

An ellipsometer(Gaertner L117 Manual Ellipsometer) was used to measure the refractive index and the thickness of the deposited films. Reflection ellipsometric measurements involve illuminating the surface of a sample with monochromatic light of known wavelength and polarization at a fixed angle of incidence, and then analyzing the change of polarization that takes place on reflection due to the difference in attenuation amplitude and phase shift experienced by the p(parallel) and s(perpendicular) components.

Figure 3.5 shows the schematic of the system set-up. The light source used in this study is a He-Ne laser(632.8nm). The beam is circularly polarized at the laser output and passes through a polarizer. In passing through the polarizer the beam polarization is converted from circular to linear. This constant intensity, linearly polarized beam is then converted to one of elliptical polarization by a quarter-wave compensator (wave plate oriented at +45°). Upon illuminating the surface of the sample, the reflected light, with its polarization altered by the properties of the sample, passes through an analyzer and an optical interference filter and is sensed by a photodetector. Certain azimuth settings(P) of the polarizer cause the light reflected from the sample to become completely linearly polarized. When the polarizer is rotated to one of these settings, the analyzer can then be rotated to a position(A) where almost no light reaches the detector, thereby indicating the lowest reading on the extinction meter. This is the condition at which polarizer and analyzer readings are recorded.

When an elliptically polarized light is reflected from a surface, its polarization direction is changed by the refractive index and absorption coefficient of the reflecting surface. If the surface is a thin film, as shown in Figure 3.6 of a three medium system, then the film thickness also enters into the reflection equation[Azz77]. The Fresnel

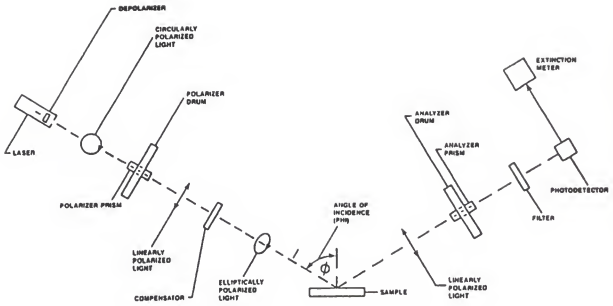

Figure 3.5 Optical system functional diagram for the reflection Ellipsometry measurement[Gae86].

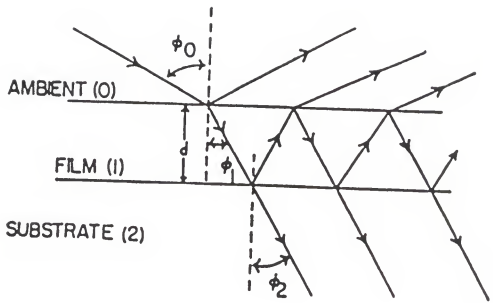

Figure 3.6 Oblique reflection and transmission of a plane wave by an ambient(0)-film(1)-substrate(2) system with parallel-plane boundaries[Aza79].

equations are shown as follows:

$$r_{01p} = \frac{N_1 \cos\phi_0 - N_0 \cos\phi_1}{N_1 \cos\phi_0 + N_0 \cos\phi_1} \qquad (3.2.1)$$

$$r_{12p} = \frac{N_2 \cos\phi_1 - N_1 \cos\phi_2}{N_2 \cos\phi_1 + N_1 \cos\phi_2} \qquad (3.2.2)$$

$$r_{01s} = \frac{N_0 \cos\phi_0 - N_2 \cos\phi_1}{N_0 \cos\phi_0 + N_1 \cos\phi_1} \qquad (3.2.3)$$

$$r_{12s} = \frac{N_1 \cos\phi_1 - N_2 \cos\phi_2}{N_1 \cos\phi_1 + N_2 \cos\phi_2} \qquad (3.2.4)$$

where r_{01p}, r_{01s}, r_{12p}, r_{12s} are interface Fresnel reflection coefficients. In general N_i is a complex number, but for a non-absorbing medium it is real number n_i. N_o is the refractive index of the incident medium(usually air), N_1 corresponds to the unknown film and N_2 to a known substrate. ϕ_i are the angles in each medium and they are related by Snells' law.

$$n_0 \sin\phi_0 = n_1 \sin\phi_1 = n_2 \sin\phi_2 \qquad (3.2.5)$$

Figure 3.6 shows that multiple reflections will occur in the thin film, thus the reflected beam is a sum of infinite contributions and the complex amplitude reflection coefficients (for both polarizations) can be found to be[Azz77]

$$R_p = \frac{r_{01p} + r_{12p} e^{-i2\beta}}{1 + r_{01p} r_{12p} e^{-i2\beta}} \qquad (3.2.6)$$

$$R_s = \frac{r_{01s} + r_{12s} e^{-i2\beta}}{1 + r_{01s} r_{12s} e^{-i2\beta}} \qquad (3.2.7)$$

where β is the phase change that the multiply-reflected wave inside the film experiences as it trverses the film from one boundary to the other. It is given by

$$\beta = 2\pi \left(\frac{d}{\lambda}\right) n_1 \cos\phi_1 \qquad (3.2.8)$$

where d is the film thickness, and λ the wavelength of the incident light.

The complex-amplitude reflection coefficients may be written in terms of their absolute values and angles[Azz77]:

$$R_p = |R_p| e^{i\Delta_p} \quad ; \quad R_s = |R_s| e^{i\Delta_s}$$

From measurements of the incident and reflected polarizations (i.e. ellipsometry) the ratio

$$\rho = \frac{R_p}{R_s}$$

of the overall system is determined. Expressing ρ in terms of the ellipsometric angles Φ and Δ,

$$\rho = \tan\Phi \; e^{i\Delta} = \frac{R_p}{R_s} \qquad (3.2.9)$$

where Φ and Δ are ellipsometric angles: amplitude ratio change

$$\tan\Phi = \frac{|R_p|}{|R_s|} \qquad (3.2.10)$$

and change in phase difference

$$\Delta = \Delta_p - \Delta_s \qquad (3.2.11)$$

In the ellipsometric measurement, two sets of polarizer and analyzer readings, i.e. P_1, P_2, A_1, A_2, were taken. They are related by the following relations

$$P_2 = P_1 + 90 \tag{3.2.12}$$

$$A_2 = 180 - A_1 \tag{3.2.13}$$

Thus by tracing the two sets of data systematic errors are reduced and better statistics are obtained. These measured data can be used to calculate ellipsometric angles using the following relations:

$$\Psi = \frac{[180 - (A_2 - A_1)]}{2} \tag{3.2.14}$$

$$\Delta = 360 - (P_1 + P_2) \tag{3.2.15}$$

Parameter Psi(Ψ) varies from 0 to 90, while Delta(Δ) can assume values from 0 to 360.

Equations (3.2.7)~(3.2.11) can not be solved analytically for n_1 and d, but numerical methods have to be applied. In this study, a computer program was developed by Ochoa to calculate the n_1 and d. By using the program, a quick determination of n_1 can be made by graphically comparing the Δ and Ψ measured to calculated values.

Once N_1 is found, d can be calculated using the following

equation[Azz77]

$$d = d_0 + [\frac{1}{2}(N_1^2 - N_0^2 \sin^2\phi_0)^{-1/2}]m\lambda \qquad m = 0, \pm 1, 2, 3.. \quad (3.2.16)$$

Thus, the thickness calculated is not an unique value. However, if one knows the approximate thickness, so that m may be defined, then an accurate value can be obtained. The thickness of the films were checked by using other techniques, such as profilometry, SEM, and interferometry, whenever necessary.

3.2.9 Raman Spectroscopy

3.2.9.1 Raman scattering

In a Raman scattering experiment, visible light from a polarized monochromatic laser is passed through the sample. A small fraction of light is scattered by atoms, and some of this fraction of light interacts with the sample in such a way as to excite a vibrational mode. When this occurs the energy of the scattered light is reduced(e.g. for Stokes) by an amount corresponding to the energy of the vibrational transition. This type of inelastic scattering is known as Raman scattering. The energy of the scattered light is analyzed using a spectrometer. Raman lines appear as weak peaks shifted in energy from the Rayleigh line. The positions of these Raman peaks about the incident line correspond to the

frequencies of Raman active vibrations as illustrated as in Figure 3.7[McM88].

3.2.9.2 Measurement on thin film samples

Raman scattering is a useful method to get information about vibrational or rotational modes in molecular systems. The scattered flux which enters the spectrometer is proportional to the intensity of the exiting beam and to the number of molecules which are included in the illuminated sample volume which is defined by the image of the entrance slit of the spectrometer.

In order to study efficiently Raman scattering in a thin film, the scattering from the film must be maximized, while scattering from the substrate must be minimized. Several Raman scattering measurement techniques, such as the waveguide method[Lev74], the total reflection coupling method[Dup74], and the Raman microprobe[She88] etc., have been used to study thin film samples. Among them, the waveguiding method is the most effective and has been successfully used in the studies of various waveguiding films[Ste88, Tal88, Levy74, Gal78].

In this study, the Raman spectra of GeO_2-SiO_2 films were obtained by using the waveguiding technique. The Raman spectra were obtained by using the experimental set-up as shown in Figure 3.8. An Ar^+ ion laser beam(514 nm) was prism-coupled into the thin film by using a high index glass prism (n=1.8054). The polarization of the laser beam was parallel

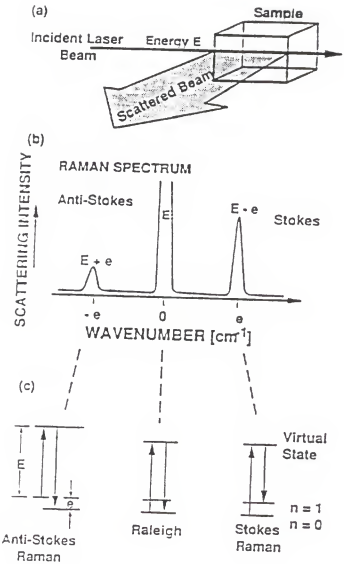

Figure 3.7 (a) The Raman scattered light, (b) The Raman spectrum consists of a Rayleigh scattering peak, and the much weaker Raman shifted lines. (c) The energy level diagram for the Raman scattering [McM88].

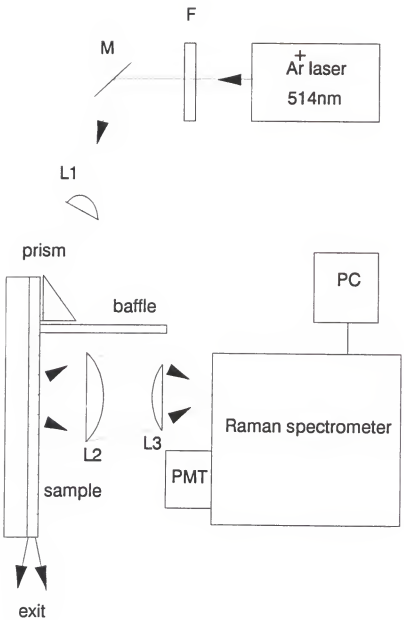

Figure 3.8 Experimental setup for waveguide Raman spectroscopy.

to the plane of the film, i.e. TE mode, and the power incident on the coupling prism was typically 400mW. The scattered light was collected, in a nearly 90° configuration with respect to the direction of propagation of guided wave in the film, into the slit of the spectrometer (Instruments S.A. Ramanor U1000 Monochomator). The spectrometer has a computer-controlled 1.0m double monochromator equipped with two gratings(1800 grooves/mm) and a photomultiplier tube. For this study, the spectral resolution of the system is 5 cm^{-1}, slit size is 500 μm and a integration time of 20 sec. is used.

For the films that do not possess waveguiding quality, the Raman spectra were obtained by using a microprobe configuration as shown in Figure 3.9. A small portion of the green light was reflected by a beam spliter(BS), passing through a microscope objective(40x) and directed to the film and the substrate. The scattered light was then collected by the same microscope objective. The objective was finely adjusted to focus on the surface, so that the signal from the substrate was minimized and the film signal was maximized. The power of the laser light directed to the sample is 15 mW, the spectral resolution used was 2 cm^{-1}, integration time was 5 sec., and a silt size of 500 μm was used.

3.2.10 Planar Waveguide Characterization

3.2.10.1 Prism coupling

Prism coupling is one of the primary diagnostic tools for

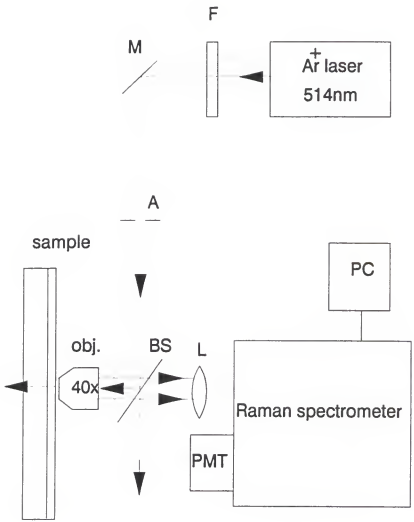

Figure 3.9 Experimental setup for Raman microprobe spectroscopy.

studying the propagation characteristics of dielectric waveguides. The theory of prism coupling has been treated extensively in the literature[Tie71, Ulr70, Tie70], and the basic concepts will be summarized here. In its simplest form, the coupler makes use of a high refractive index prism placed in close proximity (air gap< $\lambda/4$) to a planar waveguide as shown in Figure 3.10. In order to excite all possible waveguide modes, the phase matching condition between prism and film has to be met. This require the index of prism(n_p) to be larger than that of the film(n_f).

When an optical beam passing through the prism is incident upon its bottom face at an angle exceeding the critical angle, the beam will be totally reflected at the base of the prism. Because of the total reflection, the electromagnetic field in the prism is a standing wave that may be described by an exponentially decreasing function below the base of the prism. The part of the field that extends below the prism base is called the evanescent field. Since it decreases rapidly away from the prism, it does not represent free radiation. The evanescent fields that extend below the prism base can penetrate into the waveguide by a process called optical tunneling. These fields are capable of transferring power between the incident beam and a waveguide mode. By appropriate choice of the angle of incidence and proper coupler design, a significant portion of the power in the incident beam may be transferred into a single chosen

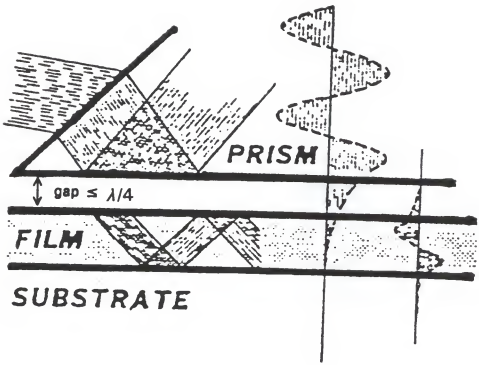

Figure 3.10 Overlap of evanescent fields causes the excitation of waveguiding mode[Tie71].

waveguide mode(called excitation of a mode). Further, by reciprocity, if a second identical prism is placed in close proximity to the waveguide at some distance away from the input prism, each propagating mode will be coupled out of the guide at an angle that is characteristic of the particular mode.

3.2.10.2 Mode index measurement

By utilizing a prism coupling technique, the light may be coupled into the waveguide, as shown in Figure 3.11. Because the transverse resonance condition[Tie71] has to be satisfied in order to guide the light, as has been described in section 1.3.1, the coupling occurs at specific discrete angles. The maximum coupling takes place when the phase matching condition between the light within the prism and the specific propagation mode within the waveguide is met. This will be discussed in more details in section 6.2. The mode index of the propagating mode may be obtained by measuring the incident angle of the laser beam into the coupling prism, which efficiently excites that specific mode in the waveguide.

To measure the angle of incidence to the coupling prism, a precision rotation stage(Klinger), as shown in Figure 3.12 is used. The waveguide (substrate refractive index=1.4579 at 632.8nm) was held in a holder with a high index glass prism(SF-6 n= 1.8052) closely attached to its surface. The waveguide was placed so that the corner of the prism was at

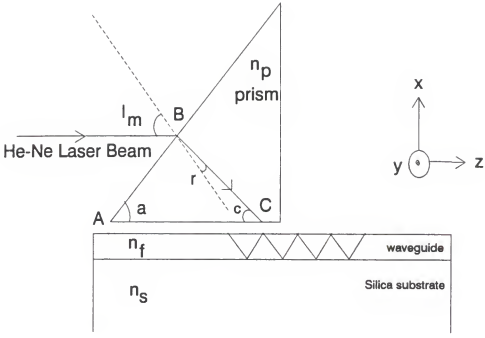

$$n_p > n_f > n_s$$

Figure 3.11 Ray diagram for the prism coupler.

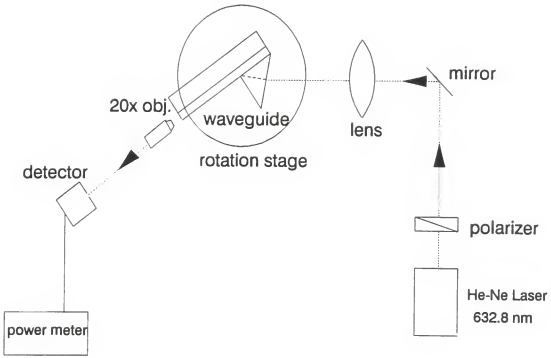

Figure 3.12 Experimental setup for mode index measurement, P: polarizer, L: lens, and D: photodetector.

the center of the rotation stage. A He-Ne laser(λ=632.8nm, 20mW, Spectra-Physics) was focused into the prism with a lens of long focal length. The point of maximum coupling, determined as the input incident angle is slowly increased by rotating the stage. The light passing through the film is collected at the end of the waveguide by a microscope objective(20x) and detected by a photodetector(Newport 818-SL). The incident angle that gives the maximum light output is recorded.

3.2.10.3 Propagation loss measurement

There are two types of losses which contribute to the propagation loss in optical waveguides: absorption losses and scattering losses.

The absorption losses, at various specific wavelengths, are primarily caused by the presence of impurities; especially the transition metal and hydroxyl ions. These losses may be kept small by controlling the composition of the waveguide materials. The scattering losses are of two types: volume scattering and surface scattering. Volume scattering is caused by imperfections such as pores, inclusions(i.e. density and/or composition fluctuation regions) etc., within the volume of the waveguide. The type of loss depends very strongly on the relative size of the imperfection in comparison with the wavelength of light in the material as well as its concentration. Surface scattering loss can be

significant particularly for the fundamental mode in an asymmetrical waveguide because most of the guided energy in this case is confined to the region that is closer to the surface. The estimation of propagation loss is important in the waveguide design and fabrication, because from an application point of view, the waveguide should have as low an insertion loss as possible, and propagation loss is one component of the insertion loss.

Several methods of measuring the attenuation have been reported[Tie71]. First, laser light is coupled into the film, e.g. with a prism coupler, and then it propagates freely in the form of a streak in the film. Usually , for an non-absorbing material, as long as the attenuation is 1 dB/cm or more, the attenuation in the film can be determined by measuring the intensity of the scattered light as a function of distance along the guided beam. This method has been successfully used for measuring attenuation as low as 0.3dB/cm[Nou85]. The intensity of the scattered light is a product of the local intensity of the scattering efficiency. Because the latter is not necessarily homogeneous along the guide, the results from this technique become ambiguous for lower losses.

The most widely used method for measuring the attenuation of a waveguide is to measure the transmitted power as a function of waveguide length[Tie71]. In this method, all the energy flowing through the guide must be collected in the

detector. If one does not want to cut the waveguide and polish the end face, one has to use an output coupling prism to extract the energy out of the guide at different positions.

The plot of output power vs. distance has a negative slope as some power is either absorbed by the impurities or lost by scattering. The magnitude of the slope is the attenuation of the waveguide. To have a reliable measurement, however, it is necessary to keep the same coupling for each of the prism at all positions of the output prism. This condition is rather restrictive as the input prism tends to get disturbed while moving the output prism.

Various methods have been used to assure a high extraction efficiency: Weber et al.[Web73] used index matching liquid between prism and guide. But when several modes are present, the output light of individual mode tends to overlap, which makes difficult measurements of individual mode loss.

When no index matching liquid is used, the prisms must be strongly clamped to the guide, and care must be taken not to disturb the input coupling, not to spoil the guide surface at the contact point, and not to locally change intermodal coupling.

In this study, an improved three prism loss measurement method[Won80], in which the results are independent of the prism coupling coefficients, is used to measure the propagation loss. The experimental setup is shown in Figure 3.13. Prism 1, 2, and 3 are independently clamped to the

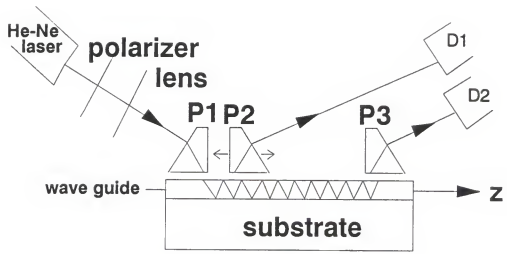

Figure 3.13 Experimental setup for three-prism loss measurement; P1, P2 and P3 is glass prism, D is photodetector.

waveguide. Small glass prisms(base length 5 mm, n=1.85) are used, The air gap between the film and the prism is adjusted to be small compared to the wavelength of the incident light. The sample is mounted on a rotational stage. The whole system is adjusted by an xyz translation stage so that the coupling point remains practically stationary on the prism base when the stage is rotated through an angular range, where the coupling is possible. The linearly polarized laser beam(parallel polarization, He-Ne, 632.8nm) was focussed into the input prism 1, so that the beam coincides with the coupling spot at the prism base to obtain an efficient coupling. During the measurement, prisms 1 and 3 are fixed, while prism 2 is moved along the guide in the z direction. The output power from prisms 2 and 3 are detected by photodetectors.

3.2.10.4 Mode profile measurement

Measurement of the mode profile is of great importance in waveguide characterization. When two waveguides are connected end to end for coupling, the efficiency of power transfer depends upon overlap of the fields in these waveguides. Thus a variety of coupling problems arise, such as fiber to fiber, laser to waveguide, fiber to waveguide, and waveguide to waveguide coupling etc. It is therefore necessary to undertake an experimental determination of the mode profile. Moreover, in the cases such as the performance of the

directional coupler, and bend-induced losses, all depend on the mode profile.

Two methods are commonly used to carry out the mode profile measurement. Both use an imaging lens of short focal length placed near the waveguide(i.e. near field method) to magnify(250x-500x) the mode profile. For the detection system, one method uses a vidicon camera placed at the image plane and an oscilloscope to view the video signal[Kor82], while the other way employs a suitable semiconductor photodetector with a small aperture to scan along the image plane manually[Kei79]. The latter is slower, while using the video-oscilloscope combination allows the entire profile to be viewed continuously and the signal to noise ratio of the signal to be increased by averaging the signals from several successive frames.

In this study, the second method was used to measure the mode profile of the waveguides, as shown in Figure 3.14. The multimode planar waveguide is polished at the output end, down to 0.25um diamond paste, to avoid scattering. The waveguide is excited using a prism coupler at the input end. The modes are individually excited and the waveguide output is collected by a high quality planar objective(20x) lens and imaging the waveguide end after approximately a distance of 150cm on a photodetector(Newport 883-UV) with a digital power meter (Newport Model 815). A 10um slit was mounted at the front end of the detector. The intensity profile of the image is

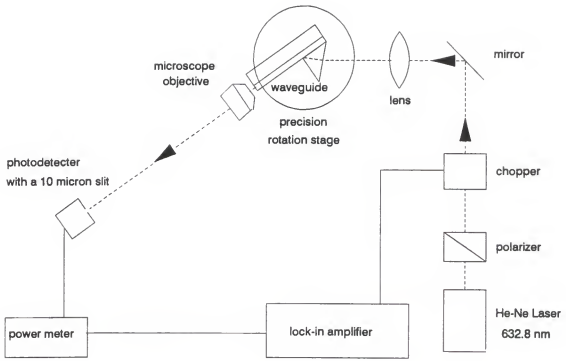

Figure 3.14 Experimental setup of the near field method for mode profile measurement.

measured by scanning the slit/detector combination using a precision translator along the image plane. The magnification of the image is determined by imaging an electron microscope aperture(10um size) at the detector face and scanning the detector. For a working distance of 150cm the magnification of the near field image is around 350.

To improve the sensitivity of the method, the beam is mechanically chopped at a frequency of 50 Hz, and the detector output is measured in conjunction with a precision lock-in amplifier (EG&G Princeton Applied Research 5208 Two Phase Lock-in Analyzer) to detect the intensity profile along the image plane.

3.2.11 Third Harmonic Generation(THG) Measurement

Due to the increasing importance of understanding the origin of the nonlinear optical susceptibility of glasses and its dependence on the constituents present in the material, the nonlinear optical property of high index glass films of both GeO_2-SiO_2 and GeO_2-TiO_2 systems was investigated. A Third harmonic generation(THG) Maker fringe measurement was used to measure the value of $\chi^{(3)}$ of films prepared by the sol-gel method. The measurement was conducted and analyzed in Dr. George Stegeman's laboratory at the University of Arizona.

THG is an ideal technique for measurements of relative small values of $\chi^{(3)}$ in films deposited on transparent substrates. The samples considered here consist of a thin

film (~1μm) deposited on a much thicker substrate. The expected THG signal from the thin film is too small to be measured by optical techniques such as Degenerate Four Wave Mixing (DFWM), or Kerr rotation for incident directions outside the film. The THG technique also has the advantage that it probes purely electronic contribution to the nonlinearity when the third harmonic frequencies are far from resonance. Therefore, orientational and thermal effects as well as other dynamic nonlinearities derived from excitations under resonance conditions are eliminated.

3.2.11.1 Third harmonic generation

When an intense laser pulse is focused into an isotropic medium, the total polarization of the material can be expanded into a power series of the applied optical field. Because of the existence of center of symmetry in a macroscopic sense, the first nonlinear process to occur varies as the cube of the electric field [Blo65]

$$P(\omega_o) = P_L + P_{NL} = \varepsilon_o [\chi^{(1)} E_o'' + \chi^{(3)} (E_o'')^3] \qquad (3.2.17)$$

The nonlinear polarization cubic in the field can lead to many nonlinear processes. Typically one nonlinear process dominates over the others because phase matching occurs, for example in DFWM or the optical Kerr effect. In the case where the experimental geometry does not produce a nonlinear phase

matched effect, Maker fringes(i.e. an interference fringes) can be obtained by varying the optical path in the nonlinear material, either by thickness or refractive index changes. Figure 3.15 shows the schematic of the formation of THG interference fringes in a three-layer system. Kajzar et al.[Kaj83] studied the nonlinear susceptibility of polydiacetylene films, deposited by the Langmuir-Blodgett(LB) technique on both sides of the substrate, using the THG interference fringes method(similar in shape to the Maker fringes but of a different origin). These authors proposed that the interference pattern results from interference between the harmonic light emitted by the film on the forward face with that emitted by the film on the backward face. The dispersion of the refractive index of the silica substrate introduces a dephasing factor between harmonic waves generated at both sides of the substrate. This dephasing factor varies as the plate is rotated and the interaction length in the substrate varied.

According to Kajzar and Messier's analysis[Kaj86, Kaj87], the resultant harmonic field for linearly polarized incident light is equal to the sum of contributions from consecutive nonlinear media:

$$E_R^{3\omega} = T_1 E_1^{3\omega} + T_2 E_s^{3\omega} + T_3 E_2^{3\omega} = \Sigma\ T_j E_j^{3\omega}(\mathbf{r}_j, t) \qquad (3.2.18)$$

To calculate the radiated harmonic field strengths, $E_1^{3\omega}$, $E_s^{3\omega}$,

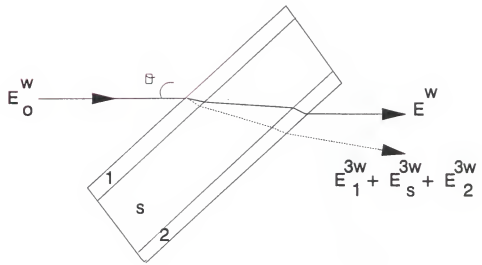

Figure 3.15 The schematic of THG interferometry measurement.

and $E_2^{3\omega}$, associated with each of the three media, multiple reflections of both the fundamental and harmonic fields are ignored. This can be justified for angles of incidence away from the normal. Each harmonic field at the output of a nonlinear plane parallel slab of thickness d is given by[Kaj86]:

$$E^{3\omega} = 4\pi \left(\frac{P_{NL}}{\Delta\epsilon}\right) ATe^{i\psi_*}[e^{i\Delta\psi} - 1] \qquad (3.2.19)$$

where $P_{NL}=1/4\ \chi^{(3)}\ (E_o^{\omega})^3$ is the nonlinear polarization inside the slab, $T(T_1, T_s, T_2)$ is a total transmission factor, $A(A_1, A_s, A_2)$ is a coupling factor determined by boundary conditions, E_o^{ω} is the fundamental laser beam electric field, $\Delta\varepsilon$ is the dielectric constant dispersion($\Delta\varepsilon = (n^{\omega})^2 - (n^{3\omega})^2$, where n^{ω} and $n^{3\omega}$ are the refractive indices at the fundamental and harmonic frequencies respectively), and $\Delta\psi$($\Delta\psi_f$ and $\Delta\psi_s$), is the phase mismatch between the fundamental(F) and harmonic(H) waves inside the slab:

$$\Delta\psi = \psi_F - \psi_H = \frac{6\pi d\,(n^{\omega}\cos\theta^{\omega} - n^{3\omega}\cos\theta^{3\omega})}{\lambda_{\omega}} \qquad (3.2.20)$$

where θ^{ω}, and $\theta^{3\omega}$ are the propagation angles of the fundamental and harmonic waves, respectively, inside the slab, and $\chi^{(3)}$(-

$3\omega,\omega,\omega,\omega$) is the third-order susceptibility tensor. All these quantities will be complex in an absorbing medium for both the fundamental and harmonic waves.

Further, the resulting harmonic light intensity can be expressed as follows[Kaj85]:

$$I^{3\omega} = \frac{c\epsilon(3\omega)}{8\pi} \left| \sum T_j \, E_j^{3\omega}(r_j, t) \right|^2 \qquad (3.2.21)$$

therefore,

$$I^{3\omega} = \frac{64\pi^3}{c^2} \left| \left(\frac{\chi^{(3)}}{\Delta\epsilon}\right)_s e^{i\psi}\left[\rho T_1 e^{i\phi}(1-e^{-i\Delta\psi_f}) + T_2(e^{i\Delta\psi_s}-1) + \rho T_3 e^{i(\Delta\psi_s+\phi)}(e^{i\Delta\psi_f}-1)\right] \right|^2 (I_o^{\omega})^3 \qquad (3.2.22)$$

which leads to a complex interference spectrum as a function of the angle of incidence when the substrate is rotated along an axis perpendicular to the incident light. In equation (3.2.22):

$$\rho = \frac{(\chi^{(3)}/\Delta\epsilon)_f}{(\chi^{(3)}/\Delta\epsilon)_s}$$

$$\psi = \psi_F^f + \psi_H^f + \psi_H^s$$

$T_{1,2,3}$ are transmission factors arising from the boundary conditions, ϕ is the phase of film susceptibility provided that of substrate is equal to zero (in the opposite case, it is the difference), and I_o^{ω} is the incident light intensity.

Because of the small film thickness($l<<l_c$, where $l_c=\pi/|\Delta\mathbf{k}| =\lambda_\omega/6(n^{3\omega}-n^{\omega})$), the phase of $\chi_f^{(3)}$ relative to that of silica does not significantly change the harmonic light intensities but only the positions of the interference maxima and minima.

Equation (3.2.22) was used to fit the experimentally recorded interference fringes. From the shift and the offset of the interference fringes between the clean silica substrate and the sample(i.e. films with substrate), both the magnitude and the phase of $\chi^{(3)}$ could be obtained[Tor91a].

3.2.11.2 THG interferometry measurement

The THG experimental setup is shown in Figure 3.16. The fundamental beam of light obtained from a Q-switched Nd:YAG laser operating at 1.064μm is frequency doubled to 0.532μm by a phase-matched KDP single crystal. The frequency of the outgoing laser beam is subsequently shifted in a high pressure(~56bars) hydrogen cell by 4155cm^{-1} or its multiple through a stimulated Raman scattering process. The dispersive prism permits a separation between other Raman frequencies and the fundamental one. A system of filters allows elimination of the parasitic light. In order to obtain the Maker fringes, the vertically polarized near infrared radiation generated by

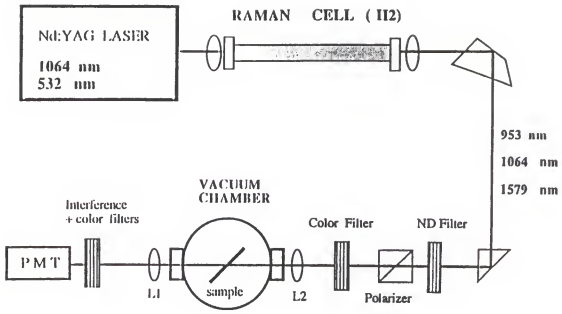

Figure 3.16 Experimental setup for THG interferometry measurement.

the H_2 shifter(i.e. 953nm, 1064nm, and 1579nm) was focused with a 20cm long focal length lens at the center of a 200 mTorr vacuum chamber. The sample was rotated with an IBM PC-controlled Oriel stepper-motor rotation stage. The pump beam was filtered with K65 Schott filters and a 1/4 m Jarrell-Ash spectrometer. The signal was detected with a Hamamatsu R-928 photomultiplier tube, preamplified, and sent to a SRS Boxcar integrator. The data was taken by typically averaging 30 pulses per data point and scanning every half degree between -30 and 30 degrees measured relative to the normal direction to the film. The DC output signal of the Boxcar was digitized and recorded by the IBM PC as a function of angle.

Two sets of Maker fringes were typically recorded for each sample at every wavelength. After fringes of the clean SiO_2 substrate were recorded, the sol-gel film(e.g. $30GeO_2$-$70SiO_2$, $50GeO_2$-$50SiO_2$, $30GeO_2$-$70TiO_2$, and $50GeO_2$-$50TiO_2$) was deposited on both sides of the substrate, and the fringes of the sample were taken. The measurement was performed in vacuum to eliminate the influence of the harmonic field that can also be generated from surrounding air during the measurement.

CHAPTER IV

GeO_2-SiO_2 FILMS BY SOL-GEL METHOD

4.1 Introduction

The sol-gel process offers a new approach to the synthesis of oxide coatings. In such a process, molecular precursors are transformed into an oxide network via inorganic polymerization reactions. The molecular precursor is usually a metal alkoxide, $M(OR)_4$, and polymerization occurs via hydrolysis and condensation. The overall reaction can be described as follows:

hydrolysis: $M(OR)_4 + x\ H_2O \Longrightarrow M(OH)_x + x\ ROH$

condensation: $M(OH)_x \Longrightarrow MO_{x/2} + (x/2)\ H_2O$

When working with a multicomponent sol, the reaction rates of various components have to be comparable to prevent preferential reaction of one component which could lead to premature precipitation of one component from the homogeneous sol. In order to obtain a homogeneous GeO_2-SiO_2 sol, the germania sol was prepared using germanium alkoxide which was modified by higher alkyl groups using an alcohol-interchange reaction as described in section 3.1.1. It was then mixed

with the silica sol which was prehydrolyzed with HCl/H_2O, according to the procedures given in Figure 3.2.

This chapter will focus on fabrication of the GeO_2-SiO_2 films, which may be used as planar waveguides, using the sol-gel method. Results related to the preparation of films as well as to various film characterizations will be presented.

4.2 Results and Discussions

4.2.1 Synthesis of Alkoxide Precursors

(1). Ammonia method: preparation of germanium ethoxide[Bra56].

Anhydrous ammonia gas was slowly bubbled into a solution of germanium-tetrachloride, ethanol and hexane as described in section 3.1.1. There was immediate formation of ammonium chloride, in both vapor phase and in solution, and an appreciable amount of heat was liberated. The supply of gas was discontinued and when the reaction mixture cooled to room temperature. After filtration and distillation, a colorless liquid of germanium ethoxide was obtained. The identification of the compound was performed by using FTIR and a ZnSe liquid cell, the spectra of germanium ethoxide and pure ethanol are shown in Figure 4.1 and Figure 4.2, respectively. Most of the absorption peaks in ethanol match those in germanium ethoxide except the broad band that occurs at ~3360 cm^{-1} corresponding to a vibration mode related to -OH groups, which does not exist in germanium ethoxide, $Ge(OC_2H_5)_4$.

(2). The alcohol-interchange method: preparation of germanium

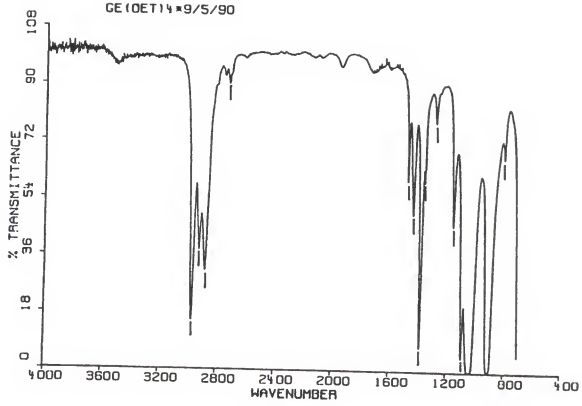

Figure 4.1 FTIR transmittance spectrum of germanium ethoxide.

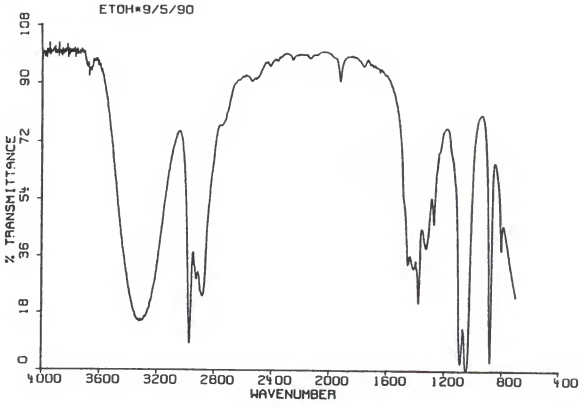

Figure 4.2 FTIR transmittance spectrum of absolute ethanol.

compounds with higher alkyl groups.

The alcohol interchange method has been used by Bradley et al.[Bra53] to prepare various germanium esters. This technique was utilized to modify the starting germanium ethoxide to replace the smaller groups by higher alkyl groups. The experimental procedure was described in detail in section 3.1.1. The replacement of the ethyl groups with higher alkyl groups is expected to increase the stability of the germanium alkoxide against hydrolysis/condensation reaction due to steric effects. The success of this modification was analyzed by using FTIR with a ZnSe liquid cell. Figure 4.3 and Figure 4.4 show the transmittance spectra of germanium ethoxide modified by 2-methoxyethanol and pure 2-methoxyethanol, respectively. When compared with the spectrum of germanium ethoxide, the absorption bands corresponding to ethyl groups were replaced by the features related to 2-methoxy-ethyl groups, indicating the high efficiency of the alcohol interchange reaction. In the present study, propanol, n-butanol, 2-methoxy-ethanol, and 2-ethoxy-ethanol have been used as modifying alcohols.

4.2.2 Sol Preparation

The GeO_2-SiO_2 sols were prepared by mixing a prehydrolyzed TEOS, and germania sols together. The germania sols have been prepared using various modified germanium alkoxides as shown in Table 4.1. Because of the reduction of the hydrolysis/

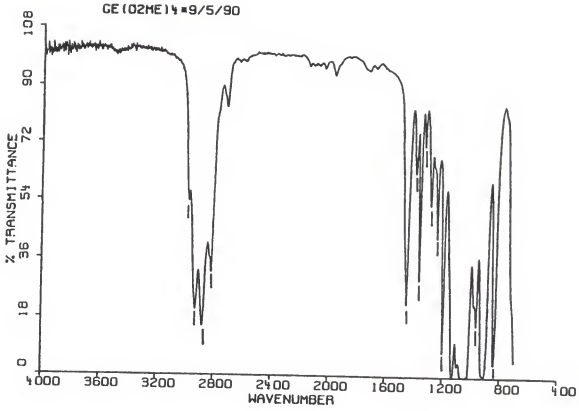

Figure 4.3 FTIR transmittance spectrum of germanium 2-methoxy-ethoxide.

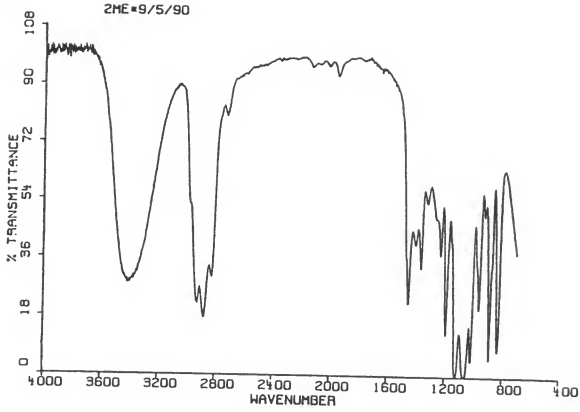

Figure 4.4 FTIR transmittance spectrum of 2-methoxy-ethanol.

Table 4.1 The Effect of Alcohol Interchange to the Quality of Germania Sols.

STARTING COMPOUND	MODIFYING ALCOHOL	SOLVENT	CATALYST	WATER	REMARK
$Ge(OC_2H_5)_4$	No	Ethanol	No	No	Cloudy
$Ge(OC_2H_5)_4$	Propanol	Ethanol	No	No	Clear Unstable
$Ge(OC_2H_5)_4$	Butanol	Ethanol	No	No	Clear Stable
$Ge(OC_2H_5)_4$	2-methoxy-ethanol	Ethanol	HCl	Yes	Clear Stable
$Ge(OC_2H_5)_4$	2-ethoxy-ethanol	Ethanol	HCl	Yes	Clear Stable

condensation reaction rates by using alkoxides with larger alkyl groups, i.e. steric hindrance effect, clear and stable germania sols can be obtained by using germanium compounds with higher alkyl groups. The achievement of a clear sol that remains stable for a long enough time is important for a multiple dip-coating process. This ensures the homogeneous composition of the sol, which in turn allows depositing films of uniform composition without degrading the film quality. In the current study, germanium 2-methoxy-ethoxide was used as the germanium precursor to prepare germania sols for making GeO_2-SiO_2 waveguides of different compositions. The preparation of the multicomponent sol was conducted according to the procedure given in Figure 3.2 as described in section 3.1.1.

4.2.3 Film Formation

One of the major limitations of the sol-gel coating process for practical application is the small thickness of each coating, which makes multiple coatings necessary for building up the required thickness for specific applications. Therefore, doing multiple coatings without degrading the film quality is the major challenge of the sol-gel coating process. In the dip-coating process, the withdrawal speed of substrate and viscosity of sol are usually low. The deposited film thickness(h) can be expressed, according to the relationship derived by Landau and Levich[Lan42] as follows:

$$h = \frac{0.94(\eta U_o)^{2/3}}{\gamma_{LV}^{1/6}(\rho g)^{1/2}} \qquad (4.2.1)$$

where η=sol viscosity, U_o=withdrawal speed, γ_{LV}=liquid-vapor surface tension, ρ=density of the sol, and g=acceleration of gravity. The thickness of the coating, therefore, can be increased by increasing the sol viscosity and/or pulling speed. In the present study, the maximum pulling speed of the dip-coating system is usually used (i.e. 3.8 cm/min.), and several organic additives, such as polyvinylpyrrolidone(PVP k-30, GAF), cp2(Daxad cp2, W.R. Grace Co.) and hydroxypropyl-cellulose(HPC, Aldrich), were used in an attempt to adjust the viscosity of the sol. Among them, only HPC was found to be compatible with the GeO_2-SiO_2 sols, thus it can be added to the sol without causing precipitation or degradation of the sol. The amount of HPC used is usually less than 2 wt%. A thicker film with improved uniformity was obtained by using HPC as an independent viscosity adjusting agent. Good quality films made with 20-72 dippings were obtained by this method. The coatings were fired after every 10 to 12 dippings depending on the sol composition.

Table 4.2 shows the results of composition analysis by using ICP solution analysis of the gels that obtained from the sols used for depositing thin films. The compositions measured are close to the target compositions except for

Table 4.2 ICP Solution Analysis of Various SiO_2-GeO_2 Gels and Trace Impurities in These Gels.

(a)

SAMPLE	COMPOSITION(mole%)	
	SiO_2	GeO_2
10GS	90.5	9.5
30GS	71.7	28.3
50GS	57.4	42.6
75GS	33.0	67.0

(b)

SAMPLE	TRACE IMPURITIES (ppm/ml)				
	Na	Mg	Al	Fe	Cu
10GS	<0.7	<0.01	<1.8	<0.2	<0.1
30GS	"	"	"	"	"
50GS	"	"	"	"	"
75GS	"	"	"	"	"

higher germania contents, e.g. 50GS and 75GS. The major reason for the deviation is believed to be due to the weighing error during sol preparation, because very small amounts of alkoxides were used for mixing the sol. Another possible source of error is the existence of a small amount of residual solvent in the germanium precursor, which was not removed completely during vacuum distillation.

Several possible common contaminants(Na, Mg, Al, Fe, and Cu) that exist in silicate glass were analyzed. All of the elements analyzed were below the detection limit of the ICP system used. The value reported in the Table 4.2(b) is 100 times of the detection limit, therefore, these impurities are in the ppb level, if present.

The composition of the films was also analyzed by XPS which confirms the results obtained by ICP analysis. Fig 4.5 shows the XPS spectrum of the 30GS GeO_2-SiO_2 thin film. No extra peak except Si, Ge, O, and trace amount of C, which commonly exist on material surfaces, was observed.

4.2.4 Thermal Analysis

Thermal behavior of the gels, including the behavior during organic burn-out, was studied using TGA/DTA analysis. The result of TGA analysis on 30GS is shown in Figure 4.6(a). The TGA curve clearly shows two distinct stages of weight loss from the sample while heating from room temperature to 1175° C. About 8% weight loss occurs upon heating to 150° C. The

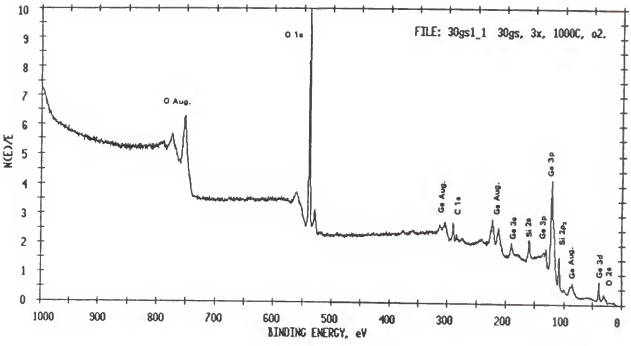

Figure 4.5 XPS composition analysis of 30GS film.

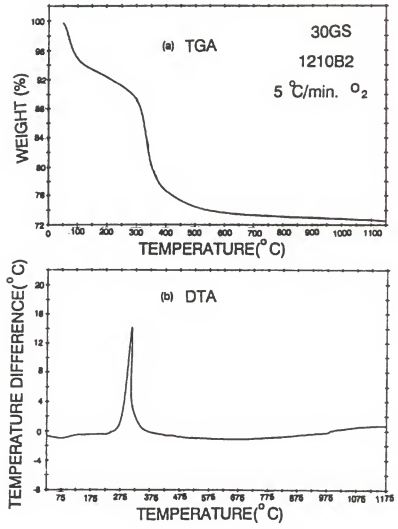

Figure 4.6 (a) TGA and (b) DTA results for 30GS gel prepared with 1.5 moles water per mole of alkoxide.

DTA curve(Figure 4.6(b)) shows a broad and small endotherm in the same temperature range, suggesting that the weight loss in this temperature range is primarily due to the elimination of residual solvent(ethanol), physically adsorbed water and possibly chemically bound water(i.e. dehydroxylation). At higher temperatures, a strong exotherm is observed which peaks around 335° C. The TGA curve shows a corresponding weight loss, i.e. 18.5%, in the same temperature range and it is believed that this peak is primarily associated with combustion of the organic binder(i.e. HPC) as well as carbonaceous material that may be present due to incomplete hydrolysis of the alkoxide. This interpretation is consistent with the observation that powder(or films) removed from the furnace in this temperature range, i.e. 200 to 600° C, has a slight brown color characteristic of material with carbon chars. This organic burn-out process should be completed when the sample is heated up to 600° C. The TGA curve shows basically a flat line in the temperature range above 600° C, and the sample removed from furnace after being heated above 600° C has a clear appearance. Similar thermal behavior was observed for 10GS gel as shown in Figure 4.7.

4.2.5 Consolidation of the Film

In order to achieve a coherent film without cracking during organic removal and densification processes, the films were heat treated following a program as shown in Figure 4.8.

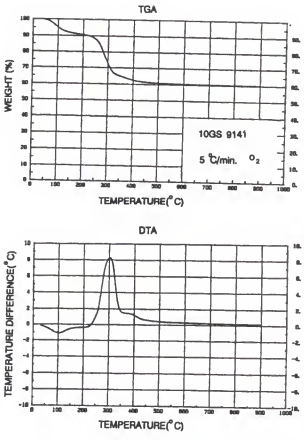

Figure 4.7 (a) TGA and (b) DTA results for 10GS gel prepared with 2 moles of water per mole of alkoxide.

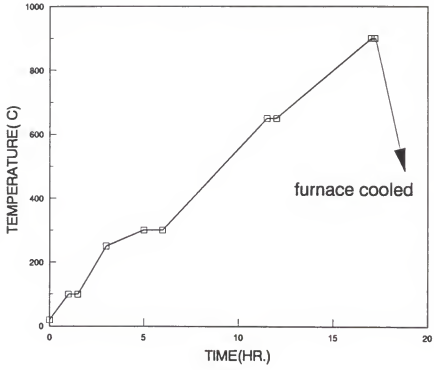

Figure 4.8 Typical temperature profile for heat-treating 30GS sol-gel film.

The upper densification temperature ranges from 700°C to 1110°C depending on the composition of the film. Figure 4.9 shows the DTA curve of 50GS gel, heat treated using the same temperature profile as shown in Figure 4.8. Following the small endotherm below 100°C, the combustion of organic additive occurs in approximately three distinct temperature ranges, between around 180°C and 600°C, with a total weight loss of about 45%.

Since the porosity and the refractive index of the porous film can be related[Yol80], the consolidation of the films with various germania contents was monitored by measuring the change of refractive index, after heat treatment in oxygen at various temperatures for 10 minutes, using a heating rate of 4°/min. The consolidation curves for all GeO_2-SiO_2 films studied, as shown in Figure 4.10, show a decrease in the index of refraction in the temperature range between 200°C and 600°C, following an initial increase by heating to 200°C. This is consistent with the thermal analysis data. The decrease in index in this temperature range is due to the loss of organic additives, before the beginning of sintering. The index increases slowly after 600°C and peaks at different temperatures for different film compositions. The film with higher germania content appears to densify at a lower temperature. The reason for the subsequent small drop in index, in films of higher GeO_2 content, at high temperatures (>800°C) is not well understood. However, according to FTIR

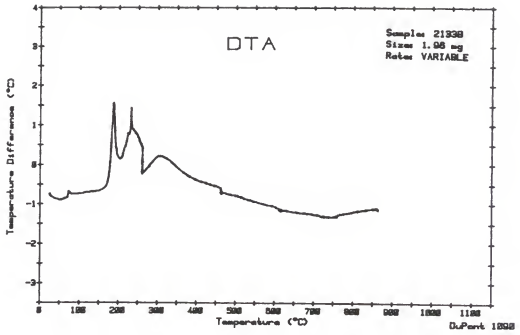

Figure 4.9 DTA result for 50GS gel.

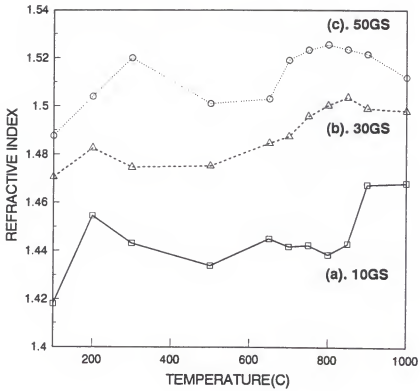

Figure 4.10 Consolidation of the GeO_2-SiO_2 films with different GeO_2 contents.

studies, as shown in Figure 4.11, it may be related to the loss of a large amount of hydroxyl groups(i.e. dehydroxylation process) which occurs between 800° and 900°C in the 30GS gel.

If the film were heat treated at excessively high temperatures or held too long at high temperatures, crystallization would take place. Figure 4.12(a) shows the X-ray diffraction spectrum of the 50GS waveguiding film (treated between 650°C~850°C for 6 hrs.), which appears to be amorphous. The GeO_2 hexagonal phase crystallizes, as shown in Figure 4.12(b), following a heat-treatment in the same temperature range for 19 hours. The observation of the formation of the hexagonal phase agrees with Mukerjee's work [Muk84, Muk86] on GeO_2-SiO_2 monolithic gel glasses, in which he observed the appearance of hexagonal GeO_2 at high GeO_2 concentrations.

Figure 4.13 shows the variation in refractive index of the film as a function of germania content. This large change in refractive index allows the preparation of waveguides with various numerical apertures, which are compatible with single mode optical fibers. The experimentally measured values are in good agreement with the values calculated by using the Lorentz-Lorenz equation[Huan78], as shown by the line in Figure 4.13, to be described in the following sections.

In general, the density of glass depends upon the type of ion present, the way these ions are arranged and the thermal history of the glass[Hug43]. In the case of silica glass, the

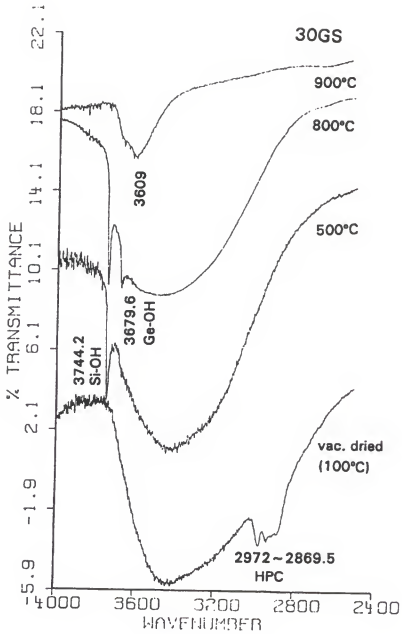

Figure 4.11 FTIR transmittance spectra showing the variation of hydroxyl content in the 30GS gel with heat treatment temperature.

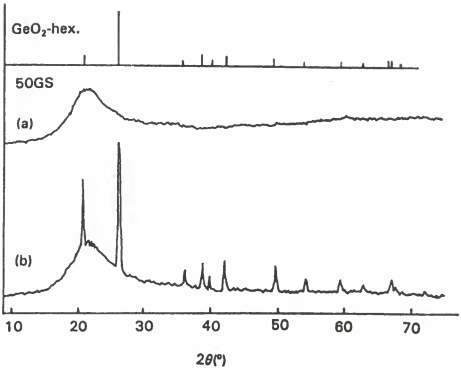

Figure 4.12 XRD spectra of 50GS film heat-treated between 650°-850°C for (a) 6 hr. and (b) 19 hr., compared to that of GeO_2 hexagonal crystal.

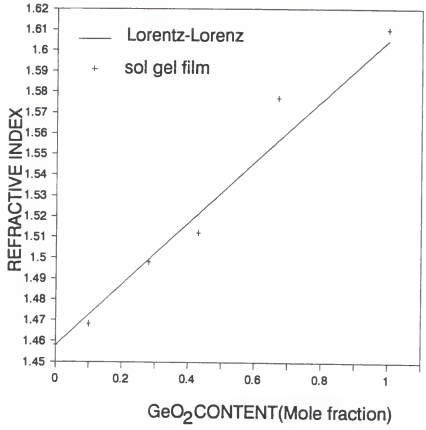

Figure 4.13 Variation of refractive index of GeO_2-SiO_2 films with GeO_2 content. +: Ellipsometry data, solid line:calculated values using the Lorentz-Lorenz model.

oxygen and silicon atoms are linked together by ionic forces, with the silicon ion electrostatically balanced by four bridging oxygen ions forming a tetrahedral structural unit[Bor69]. Germania glass has the same atomic arrangement[Rie68]. To a first approximation, it is reasonable to assume that for the entire composition range of binary germania-silica glasses, the SiO_4 and GeO_4 units within the glass retain their tetrahedral structure and form a solid solution, and the effective volume of the ions contained in the glasses remains invariant. Consequently the specific volume of germania-silica glass is additive and thus the density can be written as[Huan78]:

$$d = N_1\left(\frac{M_1}{N}\right) + N_2\left(\frac{M_2}{N}\right) \qquad (4.2.2)$$

where M_1=molecular mass of SiO_2, M_2=molecular mass of GeO_2, N=Avogadro's number, and N_1 and N_2 are the numbers of molecules per cubic centimeter of SiO_2 and GeO_2, respectively. The concept of structural compactness leads to the following expression:

$$\left(\frac{N_1M_1}{d_1N}\right) + \left(\frac{N_2M_2}{d_2N}\right) = 1 \qquad (4.2.3)$$

where d_1 and d_2 are the densities of SiO_2 and GeO_2, respectively. For a glass composition that is expressed in terms of mole fraction of germania, x,

$$x = \frac{N_2}{N_1 + N_2} \tag{4.2.4}$$

From equation (4.2.2) (4.2.3) and (4.2.4) the density of the GeO_2-SiO_2 glass can be written as

$$d = \frac{[M_2 x + (1-x)M_1]}{[M_1(1-x)/d_1] + xM_2/d_2} \tag{4.2.5}$$

The refractive index n is of prime importance, when the glass is used as a dielectric waveguide. The dielectric constant of glass contains contributions from four polarization processes: (1) space charge(or interfacial polarization) (2) orientation polarization (3) atomic polarization and (4) electronic polarization. The Clausius-Mosotti equation, which describes the relationship between the dielectric constant, ϵ, of a material and electronic α_e, atomic α_a, orientational α_d, and interfacial α_i, polarizability can be expressed as

$$\frac{\epsilon - 1}{\epsilon + 2} = \left(\frac{4\pi}{3}\right)\left(N_e\alpha_e + N_a\alpha_a + N_d\alpha_d + N_i\alpha_i\right) \qquad (4.2.6)$$

where N_e, N_a, N_s, and N_i are the number per unit volume of polarizable electronic, atomic, orientational and interfacial species, respectively.

In the optical frequency range, the dielectric constant arises entirely from the electronic polarizability, because the atomic, orientational and interfacial polarizations are unable to respond to the frequency of the external field due to the inertia of the atoms and molecules[Pye72]. Furthermore, utilizing Maxwell's relation $\epsilon=n^2$, equation (4.2.6) becomes

$$\frac{(n^2-1)}{(n^2+2)} = \left(\frac{4\pi}{3}\right)N_e\alpha_e \qquad (4.2.7)$$

Equation (4.2.7) is the Lorentz-Lorenz equation and is valid only for values of the n and molecular electronic polarizabilities at the same optical frequency. By applying the additive model for binary GeO_2-SiO_2 glasses, equation (4.2.7) can be expressed[Con67] as

$$\frac{(n^2-1)}{(n^2+2)} = \left(\frac{4\pi}{3}\right)\left(\alpha_{e1}\,N_1 + \alpha_{e2}\,N_2\right) \qquad (4.2.8)$$

where α_{e1} and α_{e2} are, respectively, the molecular electronic polarizability of v-SiO_2 and v-GeO_2; N_1 and N_2 are the numbers of molecules per cubic centimeter of SiO_2 and GeO_2, respectively. The refractive index of the binary glass system can be expressed as [Huan78]

$$n = \sqrt{\frac{2c+1}{1-c}} \qquad (4.2.9)$$

where

$$c = \frac{4\pi}{3}\left[\frac{N(1-x)\alpha_{e1}}{\left(\frac{M_1}{d_1}\right)(1-x)+\left(\frac{M_2 x}{d_2}\right)} + \frac{Nx\alpha_{e2}}{\left(\frac{M_1}{d_1}\right)(1-x)+\left(\frac{M_2 x}{d_2}\right)}\right]$$

where N is Avogadro's number($N=6.02\times10^{23}$/mole). The refractive indices for binary GeO_2-SiO_2 glass films were calculated from equation (4.2.9), using d_1 = 2.202 g/cm^3 , d_2 = 3.604 g/cm^3, $\alpha_{e1}=2.952\times10^{-24}$ cm^3, $\alpha_{e2}=3.962\times10^{-24}$ cm^3, M_1=60.09 g/mole, and M_2=104.59 g/mole[Huan78].

The formation of hexagonal GeO_2 structure from the binary GeO_2-SiO_2 glass, especially for the ones of higher GeO_2 contents, suggests the possibility of coexistence of both four-coordinated and six-coordinated Ge species in the material. The possible existence of six-coordinated Ge

species indicates an increased packing efficiency of O about Ge to a coordination of 6 which in turn would be expected to raise the index. This effect may be the reason for the data of higher GeO_2-content samples being higher than the above Equation.

4.2.6 Microstructure of the Film

The surface morphology of the waveguiding film(e.g. 50GS) was examined under SEM. Figure 4.14 is the SEM micrograph of the 50GS film surface. Two types of 'defects' were observed: (1) There are many humps, as shown in Figure 4.14(a) on the film, which may be caused by the fact that the film was deposited in an open environment where dust or other extrinsic particulates may be introduced into the sol or the film during the multiple coating process. Most of these humps are around 0.1 μm size range. (2) A few pinholes, as shown in Figure 4.14(b), were also observed in the film, although the concentration is very low. These defects of the film can cause scattering of light when the film is used for waveguiding.

The microstructure of the sol-gel prepared thin film were investigated using TEM. The film consists of very fine particles in the size range below 10nm as shown in Figure 4.15. In some areas, very small crystallites were observed which show up as dark spots in the bright field image, Figure 4.16(a). These small crystalline clusters(≤10nm) are better shown in a

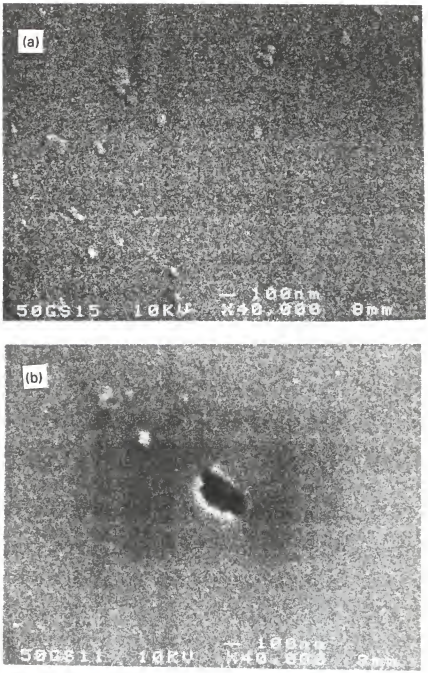

Figure 4.14 SEM micrographs of 50GS waveguiding film showing "defects" in film formation, (a) surface humps, and (b) pinhole.

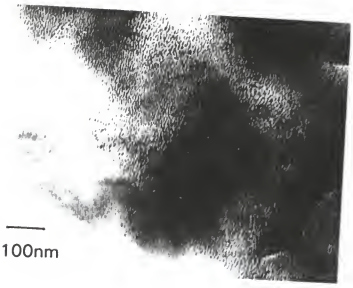

Figure 4.15 TEM micrograph of 50GS waveguiding film, showing the film consists of very fine structures at the scale of ~10nm.

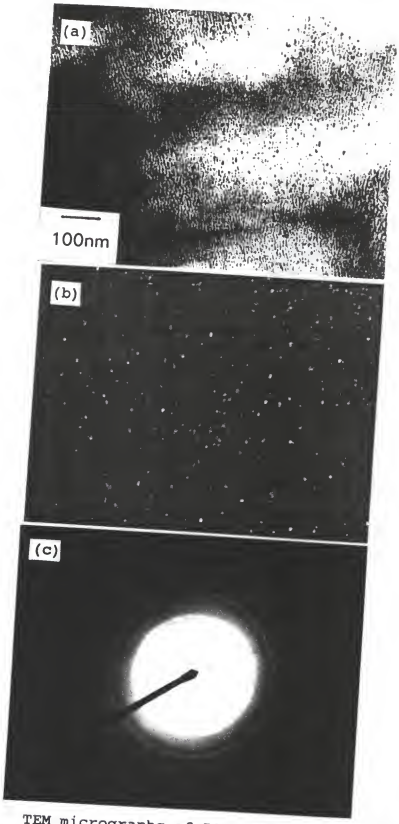

Figure 4.16 TEM micrographs of 50GS film; (a) bright field image, (b) dark field image of the (200) ring, and (c) SAD pattern.

dark field image of the (200) ring in SAD pattern, Figure 4.16(b), in which case these crystallites appear as bright spots due to intense diffraction which occurs at the small crystallites. Selected area electron diffraction(SAD) was used to analyze these crystalline phases. The SAD pattern was given in Figure 4.16(c), and shows several diffuse rings, indicating the formation of a crystalline phase in the 50GS film, although it was not detectable by X-ray diffraction studies as shown Figure 4.12(a). The analysis of the SAD ring pattern is summarized in Table 4.3. These crystallites are identified to be the GeO_2 hexagonal phase[JCP88].

4.2.7 Vibrational Spectroscopy

Infrared and Raman spectroscopy were used to investigate the structure of GeO_2-SiO_2 gel glasses as well as thin films. Figure 4.17 shows the FTIR transmittance spectra of GeO_2-SiO_2 gels with various GeO_2 contents, namely 10GS, 30GS, and 50GS, after being heat treated to 900°C in O_2. The peaks around 580cm^{-1}, which were identified[Bor69] as the Ge-O-Ge stretching modes increase with increasing GeO_2 content. The peaks around 670 cm^{-1} and 1020cm^{-1}, which were identified by Borrelli as Si-O-Ge bond stretching modes, also increase with increasing GeO_2 content, indicating the formation of a homogeneous solid solution of GeO_2-SiO_2 glass with Si-O-Si, Si-O-Ge, and Ge-O-Ge linkages that interconnect into a continuous 3-dimensional network, instead of segregation of the SiO_2 and GeO_2 phases.

Table 4.3 The Analysis of SAD Pattern of 50GS waveguide

ring	diameter(r) (cm)	d spacing (A)	GeO_2-hex. (h k l)
1	0.975	2.159	2 0 0
2	1.125	1.870	1 1 2
3	1.590	1.324	1 0 4
4	1.860	1.133	2 2 2

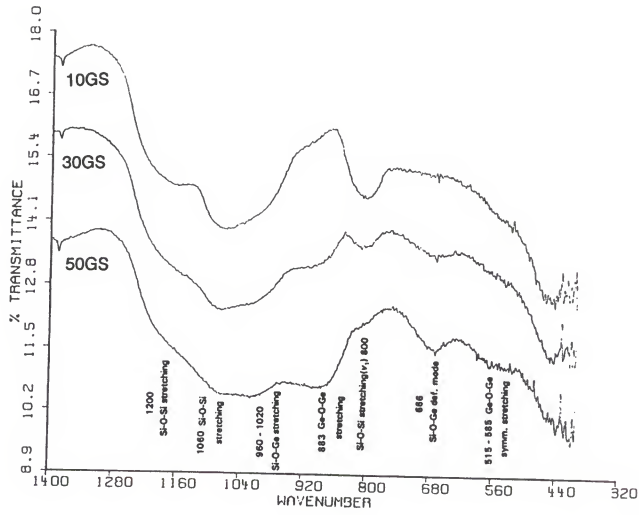

Figure 4.17 FTIR transmittance spectra of GeO_2-SiO_2 sol-gel glass after being fired to 900°C.

Another interesting feature of these spectra is the reduction of the intensity of the 800cm^{-1} band due to Si-O-Si bond stretching which appears more pronounced than the reduction of both the 1180cm^{-1} and 1090cm^{-1} bands, which are assigned to the Si-O-Si LO anti-symmetric stretching mode and TO anti-symmetric stretching mode respectively. The implications of this finding are not fully understood. In the present study, the GeO_2-SiO_2 gel with ~75% GeO_2 shows some crystallization of the GeO_2 hexagonal phase after it is heat treated to 900°C in O_2. For pure GeO_2 gel, the formation of GeO_2 crystalline clusters was found in as-prepared samples. The pure germania gel retains a large amount of hydroxyl groups even after being heat treated to 1000°C in O_2.

FTIR transmittance spectra of GeO_2-SiO_2 waveguides of various GeO_2 content were obtained using a ATR stage. The results were shown in Figure 4.18. Comparing to a pure SiO_2 film, the germania-doped film has absorption bands at around 670cm^{-1} and 1020cm^{-1} corresponding to different Si-O-Ge stretching modes, suggesting the formation of a homogeneous glass network of interconnected SiO_4 and GeO_4 tetrahedra instead of segregation of the SiO_2 and GeO_2 phases in the coatings. A limitation to the measurements using the ATR stage results from the film being so thin that interference from the SiO_2 substrate is possible. Moreover, the films, which were used as waveguides, have different thicknesses for different GeO_2 content. Therefore, only qualitative

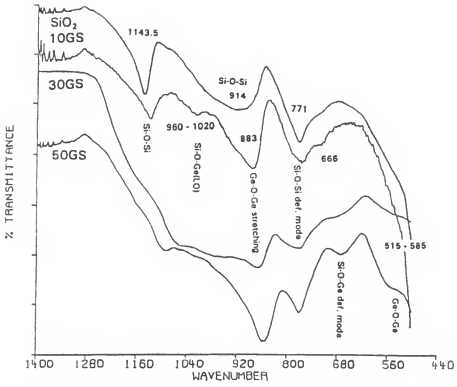

Figure 4.18 FTIR transmittance spectra of GeO_2-SiO_2 sol-gel thin films.

information may be obtained from these measurements.

Raman spectroscopy was also used to investigate the distribution of tetrahedra in multicomponent network structures in the GeO_2-SiO_2 glass films. The results are shown in Figure 4.19. When compared to the spectrum of pure SiO_2 film, several differences are observed in GeO_2-doped silicate films:

(1). The intensity of sharp bands of the SiO_2 glass spectrum at 490 cm^{-1}(D1 band) and 606 cm^{-1}(D2 band) decreases with increasing GeO_2 content.

(2). The strong, broad and asymmetric SiO_2 glass envelope with the maximum at ~430cm^{-1} appears to narrow down in band width and develop a weak shoulder at ~580 cm^{-1}; the band maximum shifts to ~418 cm^{-1}.

(3). The ~800 cm^{-1} envelope, which is a doublet composed of bands at 797cm^{-1}(TO) and ~830cm^{-1}(LO) due to the Si-O-Si stretching mode, decreases in intensity with increasing GeO_2 addition.

(4). A small weak band appears at ~675 cm^{-1} due to the Si-O-Ge stretching mode, which increases with increasing GeO_2 content.

The identification of Raman spectra in the current study was based on the work of Sharma et al.[Sha84] and Shibata et al. (Shi81). Sharma et al. studied GeO_2-SiO_2 bulk glasses with

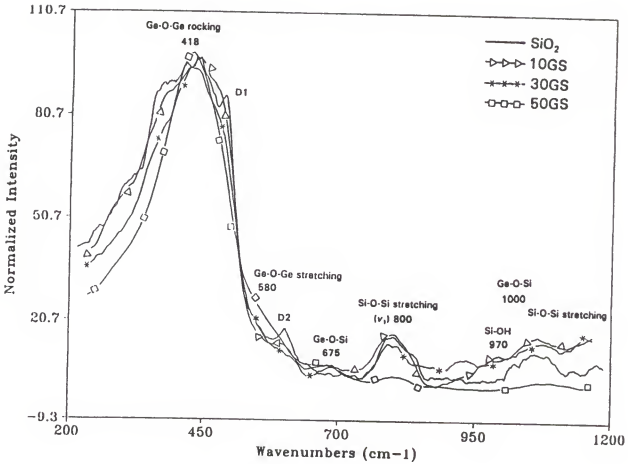

Figure 4.19 Raman spectra of GeO_2-SiO_2 thin films prepared by sol-gel process.

different GeO_2 contents, prepared by a melting technique, while Shibata et al. made their samples using a VAD technique.

The disappearance of D1 and D2 silica defect bands in GeO_2-SiO_2 Raman spectra has been observed by many researchers [Bat72, Sch73, Spr81, Chm89]. The 490cm^{-1} band in the spectrum of SiO_2 glass has been assigned to the presence of four-membered rings of SiO_4 tetrahedra stabilized by the defect centers responsible for the 606 cm^{-1} band[Sha81]. The absence of the 490 cm^{-1} band in the spectrum of GeO_2-SiO_2 glass films indicates that the addition of GeO_2 to SiO_2 makes the four-membered rings of SiO_2 tetrahedra unstable. The instability of the four-membered ring structures may be due to elimination of defect centers in the SiO_2 glass by Ge atoms.

The ~430cm^{-1} band attributed to the Si-O-Si symmetric stretching mode shifts toward lower frequency with the increase of GeO_2 content in the glass. This band also shows a decrease in its halfwidth with increasing GeO_2 concentration in the glass, indicating that the structural fluctuation in the T-O-T bond angles in the network, where T=Si or Ge, decreases in GeO_2-rich glasses[Wal75].

As it has been suggested[Sha84], the presence of a single ν_s(T-O-T) stretch band in the spectra of binary GeO_2-SiO_2 glass indicates that the modes corresponding to ν_s(Si-O-Si), ν_s(Si-O-Ge) and ν_s(Ge-O-Ge) are strongly coupled. This experimentally supports the theoretical prediction of Bell and Dean[Bel72] that the vibrational modes in the low frequency region of the

vibrational spectra of the network of tetrahedral glasses are delocalized.

The formation of Si-O-Ge linkages in GeO_2-SiO_2 glass network in the films studied was supported by the observation of the formation of ~675 cm^{-1} band.

In the higher frequency region, i.e. 850cm^{-1}~1200cm^{-1}, because of the small amount of material present in the thin films and the superposition of many vibration modes in this frequency region, a conclusive analysis is difficult.

CHAPTER V

GeO_2-SiO_2 FILMS BY LPCVD METHOD

5.1 Introduction

The rapid acceptance of LPCVD in the microelectronic industry was due to its extremely favorable economics compared to the conventional CVD method. The major reason for this cost breakthrough is the very high packing density available with stand-up closely-packed substrate loading.

The use of a low pressure(0.1~1 torr) process results in a reactor condition such that mass transfer limitations at very close substrate spacing(0.1"≥0.3") are unimportant compared to the rate of the chemical reaction at the substrate surface. With the surface reaction rate controlling the deposition, the uniform temperature inherent in a resistance-heated furnace leads to excellent uniformity of film thickness and composition.

The current study is the first attempt at the preparation of planar waveguide of GeO_2-doped silicate glass film, using the LPCVD process. In this chapter, the processing conditions as well as the results of various characterization of the prepared films will be presented.

5.2 Results and Discussions

5.2.1 Film Formation

The LPCVD system and the deposition conditions used in the present study have been described in details in section 3.1.2. Conducting the CVD process at a low pressure has several advantages when compared to atmospheric CVD process[Tani71, Ros77]:

(1) The mean free path of a reactant molecule is longer and the diffusivity of gaseous species is greater.
(2) The homogeneous reaction(i.e. soot formation) may be depressed and heterogeneous reaction(or surface reaction) becomes dominant.

These features lead to the deposition of uniform thin films on the substrates.

The details of the surface reaction mechanisms and kinetics in LPCVD process are not fully understood. In general, the gas flow within the reactor was adjusted so that the chemical reaction is depressed in the vapor phase(i.e. depressed homogeneous reaction) and a laminar flow region(or boundary layer) with a thickness of ℓ is achieved next to the hot substrate, as shown in Figure 5.1. Within the laminar flow region, the molecules transport by diffusion due to the concentration gradient across the boundary layer and the flux of certain gas species toward the substrate can be expressed

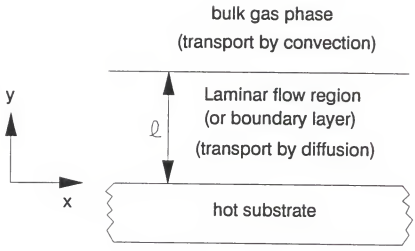

Figure 5.1 Different gas flow regions adjacent to a hot substrate in CVD process.

as follows:

$$J_i = -D_i\left(\frac{\partial c_i}{\partial Y}\right) \qquad (5.2.1)$$

where c is the concentration of molecular species i, and D_i is the diffusion coefficient of i. Assuming a linear concentration gradient across the boundary layer (5.1) yields

$$J_i = -D_i\ (\Delta c_i / \ell) \qquad (5.2.2)$$

where ℓ=thickness of the boundary layer. For a steady state Δc_i is constant. J_i is dependent upon ℓ and D_i. Due to the increase in the diffusivity of the gaseous species at low pressure condition, the diffusion flux is much higher compared to that of atmospheric CVD.

During the deposition, many reactions occur which can generally be illustrated as shown in Figure 5.2. For a temperature range between 350°C to 500°C the overall equations of the oxidation reactions are[Str68]:

$$SiH_{4(g)} + O_{2(g)} \Longrightarrow SiO_{2(s)} + 2H_{2(g)}$$
$$GeH_{4(g)} + O_{2(g)} \Longrightarrow GeO_{2(s)} + 2H_{2(g)}$$

According to the works of various researchers[Gra85, Hen72, Yu72] on the deposition of SiO_2 by CVD method, the

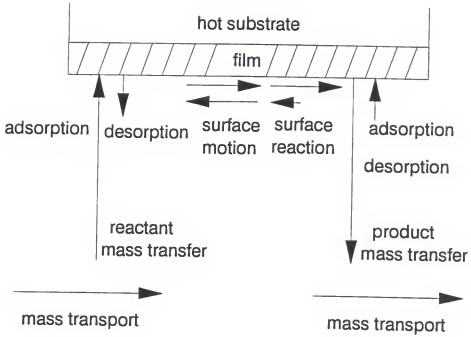

Figure 5.2 Various reactions occur during LPCVD film deposition.

hypothetical mechanisms for the surface reaction of silica film on pure silica substrate could be illustrated as shown in Figure 5.3. Since the difference in silicon and oxygen electronegativities is large(1.8 for Si against 3.5 for O[Pau60]), the Si-O bonds have a partially ionic character. At room temperature the Si bonds at the surface(dangling bonds) are saturated with hydroxyl groups. However, at temperatures above 300°C the surface undergoes a dehydration process[Sny66]. Therefore, the silicon dioxide surface consists of positively charged Si atoms and negatively charged O atoms. Grabiec and PrzyLuski hypothesized that silane reactions (i.e. adsorption(a) followed by dissociation(b), Oxygen reactions (i.e. adsorption(e) followed by dissociation(f)), and dehydration(c and g) occur independently. For the hydride LPCVD process to prepare GeO_2-doped SiO_2 films, the GeH_4 molecule behaves similarly to the silane molecule and forms a binary GeO_2-SiO_2 glass network. The various characteristics of the LPCVD films are summarized in Table 5.1.

5.2.2 Microstructure of the Film

Surface morphology of the LPCVD films was examined using SEM. Figure 5.4 shows the SEM micrographs of the films. All the films appear to consist of very fine particulates. The LP1 and LP3 films have similar morphology containing particulates of around 30nm size range, while the LP2 film

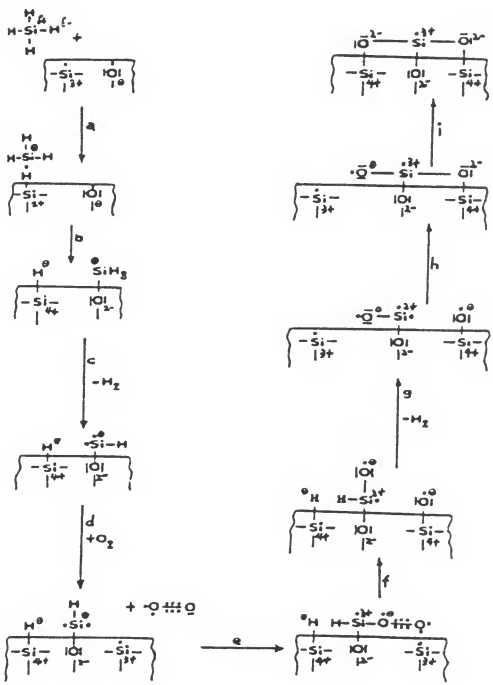

Figure 5.3 The hypothetical scheme of surface reactions in SiO_2 LPCVD process[Gra85].

Table 5.1 Characteristics of Thin Films Prepared by LPCVD Process.

Sample	Appearance	[Ge]/[Ge+Si]	Index	Thickness(um)	Abs. band	Defect structure
lp1	light brown	4.24	1.465	0.660	232nm 185nm	≡Ge-Ge≡
lp2	slightly cloudy	0.32	1.451	2.855	238nm	≡ Si-Si≡
lp3	clear	0.32	1.468	5.740	238nm	≡ Si-Si≡

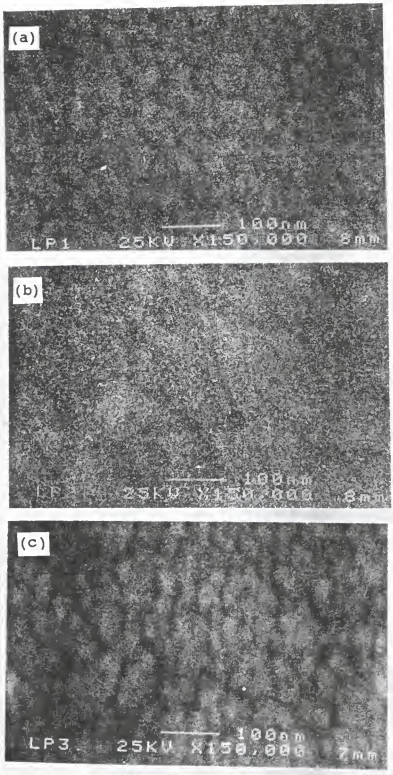

Figure 5.4 SEM micrographs of LPCVD films deposited using different processing conditions.

contains larger features around 100nm size range. The fact that the LP2 film contains larger particulates is believed to cause its slightly hazy appearance due to the increased scattering of visible light.

The microstructure of the LP3 film was investigated using TEM, and the results are shown in Figure 5.5. The film consists of much coarser particulates when compared to the film prepared by sol-gel method, see Figure 4.15. Some large inclusions in the film have also been observed, as shown in Figure 5.5(b). This particle size variation within the film could enhance the scattering loss for the light propagating in the film when it is used for waveguiding.

5.2.3 XPS Chemical Analysis

The composition of LPCVD films deposited using various conditions was analyzed by using XPS. Figure 5.6 shows the XPS spectrum of LP1 film. Only Si, O, small amount of Ge and surface carbon were detected in the sample. The atomic concentration of Ge and Si was determined by calculating the peak area of the Si2p and Ge3d peak respectively, as shown in Figure 5.7(a) and (b). The results of composition analysis of the various films are shown in Table 5.1. The LP1 film contains 4.24 at% Ge while LP2 and LP3 contain only 0.32 at% of Ge in the film. The reason for the low GeO_2 content in these films is believed to be due mainly to the use of very dilute germane gas (i.e. 0.2 wt% GeH_4/Ar) and pure silane gas

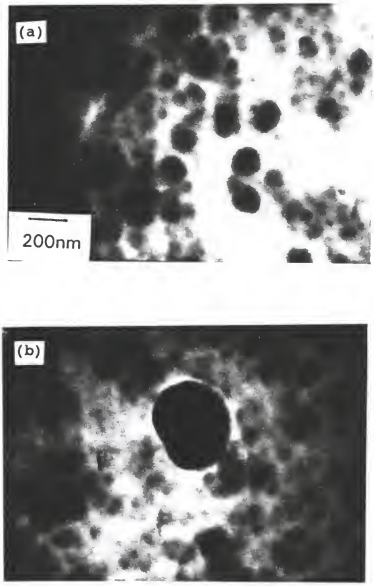

Figure 5.5 TEM micrographs of LP3 film. (a) The film contains fine particles typically around 100nm scale. (b) Large particle may be observed in some areas.

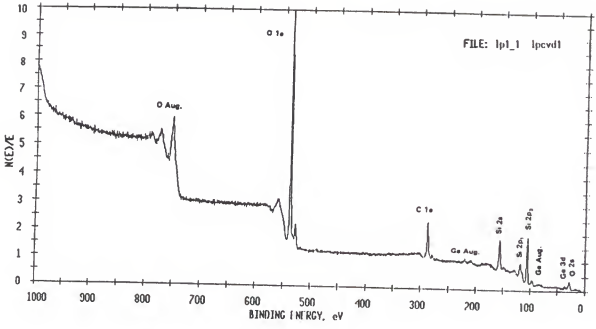

Figure 5.6 XPS composition analysis of LP1 film.

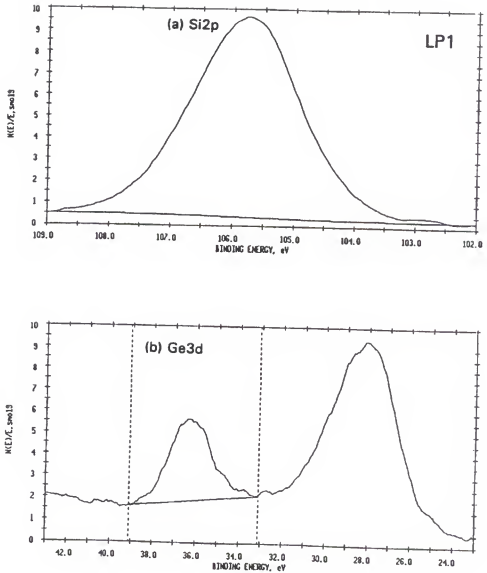

Figure 5.7 (a) Si2p and (b) Ge3d band in XPS spectrum are used to calculate the atomic concentration of the LP3 film.

as reactant gases. This result agrees with the observation reported by Huffman et al. [Huf86] that due to the differences in deposition rates in LPCVD process, higher GeO_2 content silicate films are difficult to obtain.

5.2.4 UV/VIS Spectroscopy

Optical losses in glass waveguides arise from absorption, Rayleigh scattering, and waveguide imperfections. Absorption may be caused by molecular transitions involving vibrational and electronic excitation of the intrinsic glass material and impurities or color centers that are incorporated in the processing. In general, electronic transitions are observed in the UV region, while the molecular vibrations dominate in the IR region. Absorption in the UV-Vis region(200~700nm) by GeO_2-doped silicate films, prepared by LPCVD method, was investigated in the current study. The spectra of the films are compared to those of Suprasil (Heraeous), after being normalized to the same thickness. The results are given in Figure 5.8. All the samples have an absorption band around 240nm, namely 238nm for LP2 and LP3 films, and 232nm for LP1 film. The origin of the absorption band at ~240nm is very complicated despite the fact that it has been observed for a long time[Mit56, Arn73, Gar58a]. Tohmon et al.[Toh89] studied pure SiO_2 samples using UV and vacuum UV optical absorption, photoluminescence(PL), ESR, and MO calculation. These authors found that there are two types of absorption bands near 245nm,

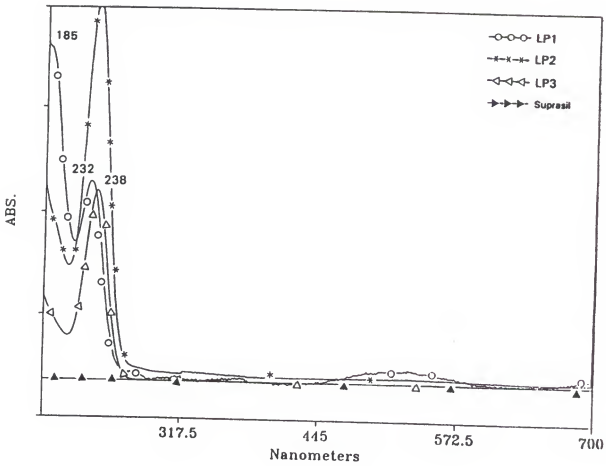

Figure 5.8 UV-Vis spectra of various LPCVD films and fused silica substrate(Suprasil). The spectra are normalized to the same thickness.

each with unique peak wavelength, halfwidth, PL spectra, and reaction to heat treatment. One of these is attributed to the oxygen vacancy defect(≡Si-Si≡). The existence of ≡Si-Si≡ can cause absorption at 245nm and 163nm due to different electronic transitions. Furthermore, Garino-Carina first studied extensively the band near 240nm observed in GeO_2 and GeO_2-SiO_2 glasses and attributed this band to the presence of GeO[Ga258]. This conclusion was supported by Cohen and Smith[Coh58]. Although it is agreed that the absorption at ~240nm in GeO_2 is related to an oxygen-deficient defect, the exact defect structure is still an issue under debate[Yue82, Rad86, Rau87, Gri90]. However, this band is more commonly refered to as an oxygen vacancy defect(≡Ge-Ge≡), and this oxygen deficient center in GeO_2 or GeO_2-SiO_2 glasses will cause the absorption at 242nm and 325nm[Row74, Lev81]. The intensity of the 242nm band has been reported to be nearly 1000 times more intense than the 325nm band[Yue82]. The absorption at ~185nm is attributed to GeO_2[Yue82]. Therefore, the absorption band for LP1 is assigned to oxygen deficient defects in GeO_2, because the tail of the absorption at ~185nm appears with the 232nm band. The absorption band(238nm) for both LP2 and LP3 film is attributed to oxygen deficient defect in SiO_2 because the tail of the absorption band appears to extend further down into vacuum UV range(most likely related to 163nm band).

5.2.5 Vibrational Spectroscopy

The refractive index and the film thickness of LPCVD samples were measured using ellipsometry and profilometry and the results are given in Table 5.1.

Infrared and Raman Spectroscopy were used to investigate the structure of GeO_2-doped silicate thin films. FTIR transmittance spectra of various films were obtained using an ATR stage, as shown in Figure 5.9. Because the Lp1 film is so thin(0.66μm) its spectrum doesn't show features corresponding to GeO_2. The spectra of both LP2 and LP3 have a broad and small absorption band between 515cm^{-1} to 585cm^{-1}, corresponding to Ge-O-Ge symmetric stretching mode[Bor69]. The formation of Si-O-Ge linkage in these GeO_2-SiO_2 films can be supported by the observation of the peak around 1000cm^{-1}(i.e. 960~1020cm^{-1}) which has been assigned to Si-O-Ge antisymmetric stretching[Bor69].

Raman spectroscopy was also used to study the distribution of tetrahedra in Lp3 waveguiding film. The result was shown in Figure 5.10. Compared to Suprasil pure silica and SiO_2 film(made by sol-gel method), LP3 film consists of structures that are very similar to those of SiO_2 after neutron irradiation, as shown in Figure 5.11[Sto70]. Basically there are some important features in LPCVD film:

(1). The major low-frequency band lies near 470cm^{-1} and is considerably narrower than in bulk SiO_2.

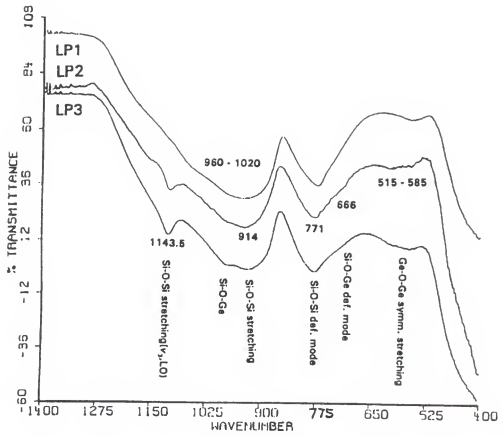

Figure 5.9 FTIR transmittance spectra of LPCVD thin films.

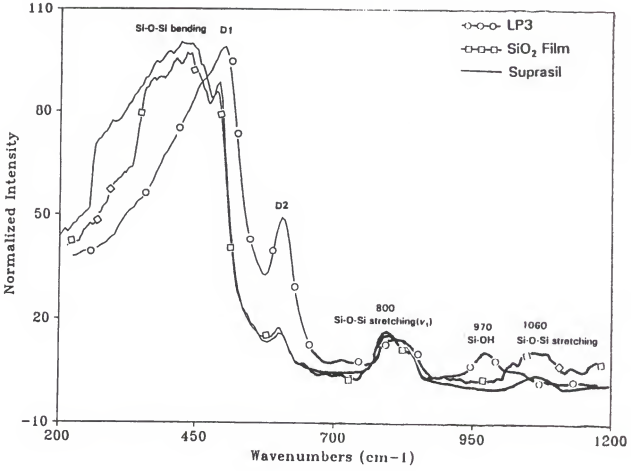

Figure 5.10 Comparison of Raman spectra of the LP3 film, the sol-gel SiO_2 film and the fused silica (Suprasil).

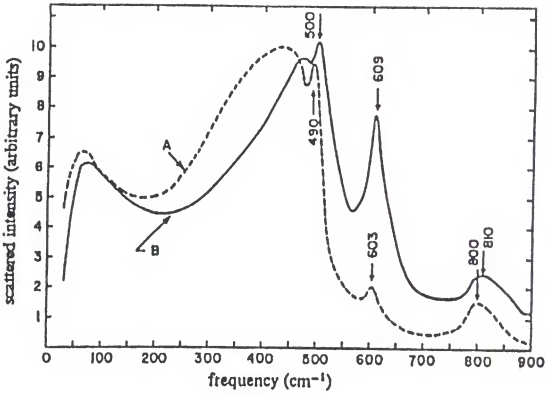

Figure 5.11 Room temperature Stokes Raman spectra for (A) unirradiated and (B) neutron-irradiated Optosil fused silica [Sto70].

(2). The defect bands at 490cm^{-1}(D1 band) and 606cm^{-1}(D2 band) appear to be the dominant structure.

(3). A peak appears at 970cm^{-1} corresponding to the Si-OH stretching mode.

The decrease of the halfwidth of the main peak indicates a narrower distribution of the T-O-T bond angles in the network, where T=Si or Ge[Wal75, Huf85].

Although the structural model for D1 and D2 defect bands are still controversial in the literature[Rev83, Sha81, Phi82, Sil84, Gal85], it is more commonly believed that D1 is related to the symmetric stretching mode of 4-membered ring of tetrahedra[Gal85] and D2 is related to the breathing mode of a planar 3-fold of bonds[Gal85]. The possible reason for the dominance of these defect structures in the LPCVD film is the low deposition temperature used in the process(e.g. 450°C far lower than 800~1150 °C used than in the sol-gel films). Therefore the material doesn't have enough energy to relax its defects to a structure that has a lower energy. According to Huffman and McMillan's work on deposition of SiO_2 by LPCVD method[Huff85], the structure of as-deposited SiO_2 may relax to near the bulk glass value and distribution on annealing at 900°C for 2 to 3 days.

The existence of SiOH in the LP3 film is believed to be caused by the reaction of hydrogen(H_2), which could be formed after the oxidation of hydride reactants, with SiO_2-GeO_2 glass

film. The formation of hydroxyl groups(SiOH and/or GeOH) in optical fibers due to the reaction with H_2 have been reported extensively in the literature[Ues83, Tan84, Ple84, Tani84, Pit84].

CHAPTER VI

PLANAR WAVEGUIDE CHARACTERIZATION

6.1 Introduction

Important waveguide characteristics such as mode index measurement, propagation loss as well as mode profile measurement are investigated by using a prism coupler as a light coupling technique as was described in section 3.2.10.

The planar waveguides used in the present study are prepared by using both sol-gel and LPCVD processes. The film properties, such as thickness, refractive index, refractive index difference(Δn) between film and substrate, and processing condition are reported in Table 6.1. The refractive index difference(Δn) is calculated by using the following equation[Nat82]

$$\Delta n = \frac{n_1^2 - n_2^2}{2n_1^2} \qquad (6.1.1)$$

where n_1= index of film(i.e. core layer), n_2= index of v-SiO_2 substrate(i.e. 1.457 for 632.8nm). The value Δn can be used to calculate an effective numerical aperture(NA) for the

Table 6.1 Planar Waveguides Fabricated Using Both Sol-Gel and LPCVD Method.

Sample	Process	Temp. (°C)	Number of dippings	Thickness (um)	Index (n_1)	Δn (%)
10GS	sol-gel	1110	72	2.615	1.485	1.87
30GS	sol-gel	900	56	1.570	1.502	3.01
50GS	sol-gel	700	22	0.667	1.550	5.82
LP3	LPCVD	450	---	5.74	1.468	0.75

waveguide with the following equation

$$NA = \sqrt{n_1^2 - n_2^2} \qquad (6.1.2)$$

6.2 Mode Index Measurement

If we represent the incident wave on the prism by a wave vector K_o, its propagation in the prism can be characterized by a magnitude $k_o n_p$ which can be decomposed into a horizontal component $k_o n_p \cos c$ and a vertical component $k_o n_p \sin c$, as shown in Figure 6.1. The boundary conditions of the electromagnetic fields at the prism base require that the field below and above the prism base have the same horizontal wave component. Therefore, maximum tunneling interaction takes place when the horizontal component of the wave vector(along the z direction) is equal to the propagation constant of a given mode among the many possible modes of the waveguide(i.e. phase matching condition is satisfied). Under this condition that particular mode gets excited[Ulr73].

Thus,

$$\beta = k_o n_p \cos c \qquad (6.2.1)$$

However,

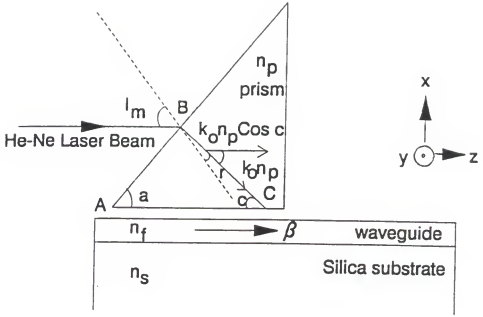

$$n_p > n_f > n_s$$

Figure 6.1 Ray diagram for the prism coupler.

$$\beta = k_o N \tag{6.2.2}$$

so that

$$N = n_p \cos c \tag{6.2.3}$$

where N is the mode index(or effective index) of a given mode, n_p= refractive index of the coupling prism. Now considering Δ ABC within the coupling prism, as shown in Figure 6.1.

$$\angle a + \angle c + \angle r + 90° = 180° \tag{6.2.4}$$

so

$$\angle c = 90° - \angle a - \angle r \tag{6.2.5}$$

and

$$n_p \cos c = n_p \sin(\angle a + \angle r) \tag{6.2.6}$$

From Snells' law at point B

$$\sin I_m = n_p \sin r \tag{6.2.7}$$

and

$$\angle r = \sin^{-1} (\sin I_m / n_p) \tag{6.2.8}$$

Thus,

$$N = n_p \sin [a + \sin^{-1} (\sin I_m / n_p)] \qquad (6.2.9)$$

The mode indices(N_m) of both 30GS and LP3 waveguides are calculated from the experimentally measured angle of incidence(I_m) for various modes and the results are given in Table 6.2 under the column I_m and N_m, respectively. By determining these strong coupling angles, we can find experimentally the characteristic propagation constants of various propagation modes in a given film, relative to the propagation constant of free space, $k_o = \omega/c$, according to the following relation[Tie71]

$$\beta = k_o N_m = k_o n_f \sin\theta \qquad (6.2.10)$$

where the θ is the ray propagating angle within the film as shown in Figure 6.6. This measurement will also lead to the determination of the phase velocity, v_m, of the various characteristic modes of propagation in the guide[Ulr73] by using the following equation

$$v_m = c/N_m = \omega/\beta \qquad (6.2.11)$$

For a planar waveguide, in order to guide the light in the structure the transverse resonance condition has to be met[Tie71, Kog79] as has been described in section 1.2.1. That is the total phase shifts introduced as the ray travels

Table 6.2 Characteristics of the SiO_2-GeO_2 Waveguides.

SAMPLE	MODE	I_m	N_m	$N_{calc.}$	A_{TE}	EF
30GS	TE0	19.833^{o}	1.494	1.493	7.947	0.970
	TE1	17.300^{o}	1.469	1.467	7.947	0.824
LP3	TE0	16.833^{o}	1.465	1.467	34.898	0.993
	TE1	16.417^{o}	1.461	1.465	34.898	0.969
	TE2	16.000^{o}	1.456	1.461	34.898	0.905

a full zig-zag cycle need to be an integral multiple of 2π, as shown below

$$2dk_o n_f \cos\theta = 2m\pi + 2\phi_s + 2\phi_c \qquad (6.2.12)$$

where $k_o = 2\pi/\lambda_o$ = propagation constant in free space,

λ_o= free space wavelength,

$k_f = k_o n_f \cos\theta$ = propagation constant in waveguide,

m= integer(or mode number)

ϕ_c= phase shift occurs at film/cladding interface,

ϕ_s= phase shift occurs at film/substrate interface.

For TE modes, the phase shift ϕ_c and ϕ_s can be expressed[Kog79] in terms of film parameters as

$$\phi_s = \tan^{-1}\left[\frac{\sqrt{(n_f^2\sin^2\theta - n_s^2)}}{n_f\cos\theta}\right] \qquad (6.2.13)$$

$$\phi_c = \tan^{-1}\left[\frac{\sqrt{(n_f^2\sin^2\theta - n_c^2)}}{n_f\cos\theta}\right] \qquad (6.2.14)$$

For a set of given film parameters of n_f, n_s, n_c, and d, and a given wavelength(λ_o) there may have different values of θ, corresponding to different mode numbers(m) for which the equation 6-14 is satisfied. For each value of θ there is a

corresponding value of incident angle(I_m) at which a given mode is excited in the waveguide[Kog74].

As mentioned in Equation (6.2.10), the propagation constant for a guided mode β is given as

$$\beta = k_o n_f \sin\theta \qquad (6.2.10)$$

and its value lies between the plane wave propagation constants in the substrate and the film[Kog74]

$$k_o n_s < \beta < k_o n_f$$

When $\beta = k_o n_s$, the mode is said to be cutoff. Mode results for slab waveguides are generally expressed in terms of normalized dimensionless parameters[Kog74] V and b. The V parameter is called the normalized frequency(or normalized film thickness) and is defined as

$$V = \frac{2\pi d\sqrt{n_f^2 - n_s^2}}{\lambda_o} \qquad (6.2.15)$$

and b is called the normalized mode index(or normalized propagation constant) and is defined as

$$b = \frac{N_m^2 - n_s^2}{n_f^2 - n_s^2} \qquad (6.2.16)$$

The index b is 0 at cutoff(i.e. $N_m = n_s$) and approaches 1 when far away from it(i.e. $N_m = n_f$).

A measure of the asymmetry of the waveguide structure is also defined[Kog74] for both TE and TM modes as follows

$$a_{TE} = \frac{n_s^2 - n_c^2}{n_f^2 - n_s^2} \qquad (6.2.17)$$

$$a_{TM} = \left(\frac{n_f}{n_c}\right)^4 \frac{(n_s^2 - n_c^2)}{(n_f^2 - n_s^2)} \qquad (6.2.18)$$

The value of a ranges from 0(i.e. perfect symmetry, $n_s=n_c$) to infinity(i.e. strong asymmetry $n_s \approx n_f$). Combining Equation (6.2.13)~(6.2.18) and substituting into Equation (6.2.12), the normalized dispersion relation may be expressed as[Kog74]

$$\sqrt{V(1-b)} = m\pi + \tan^{-1}\sqrt{\frac{b}{1-b}} + \tan^{-1}\sqrt{\frac{a+b}{1-b}} \qquad (6.2.19)$$

For a given value of m the normalized mode index b depends only on V and a. The calculated normalized film thickness as

a function of normalized mode index(or b-V characteristics) for the first four TE modes of 30GS sol gel waveguide(a_{TE}= 7.947) is given in Figure 6.2. According to the film parameters of 30GS film (n_f=1.502, n_s=1.454, n_c=1, d=1.566μm, and λ_o=0.6328μm), V parameter is calculated to be 5.845. A dotted line is drawn across the plot at constant value of V=5.845, the two intercepts with m=0 and m=1 curves give the expected b values for these two modes for 30GS waveguide which in turn may be used to obtain $N_{cal.}$ utilizing Equation (6.2.16). The calculated mode indices($N_{cal.}$) according to the step-index waveguide model, i.e. Equation (6.2.18), are listed in Table 6.2. The calculated mode indices($N_{cal.}$) are very close to the experimentally measured values(N_m).

Similarly, the normalized film thickness(V) versus normalized mode index(b) curves for the first four possible TE modes in LP3 waveguide(a_{TE}=34.898) are calculated and plotted in Figure 6.3. According to the LP3 film parameters (n_f=1.468, n_s=1.457, n_c=1, d=5.74 μm, λ_o=0.6328μm), the V parameter is calculated as 10.233. By drawing a line across the plot at constant value of V=10.233, the line intercepts first three curves(i.e. m=0,1,and 2), indicating the three possible TE modes that can propagate in LP3 waveguide. The calculated mode indices($N_{cal.}$) for LP3 sample can be obtained from the corresponding b values on the plot and using Equation (6.2.16). The results of $N_{cal.}$ are given in Table 6.2 and are very comparable with those obtained experimentally. This

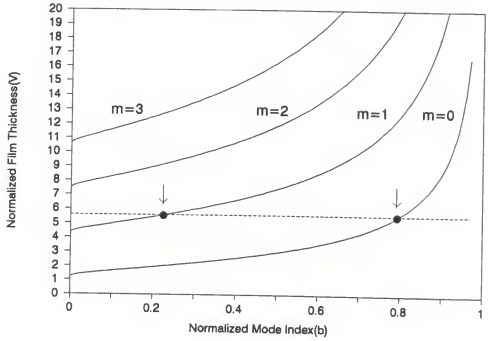

Figure 6.2 Normalized mode index(b) versus normalized film thickness(V) characteristics for the 30GS film, modeled as a step-index waveguide.

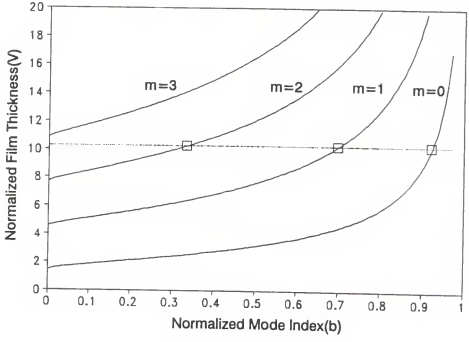

Figure 6.3 b-V characteristics of the LP3 film modeled as a step index waveguide.

indicates that the waveguides(both sol-gel and LPCVD samples) used in present study may possess approximately a step-refractive index profile.

6.3 Propagation Loss Measurement

In this study, a three-prism loss measurement method[Won80], in which the results are independent of the prism coupling coefficients, is used to measure the propagation loss in the waveguide. During the measurement, prisms 1 and 3 are fixed as shown in Figure 6.4, while prism 2 is moved along the guide in the z direction. The output power from prism 2 and 3 are detected by photodetectors.

Considering P_2 and P_3 as the output powers of prism 2 and 3, respectively, r_2 and r_3 are the coupling coefficients at the output prisms, then

$$P_2 = r_2 P(z_2) \tag{6.3.1}$$

$$P_3 = r_3 P(z_3) \tag{6.3.2}$$

where $P(z_2)$= power propagating at point z_2.

Let a be the attenuation coefficient in the waveguide, then

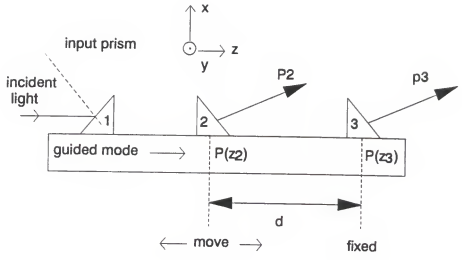

Figure 6.4 Three-prism method for propagation loss measurement.

$$P(z_3) = [P(z_2) - P_2]e^{-ad} \tag{6.3.3}$$

$$P_3 = r_3[P(z_2) - r_2P(z_2)]e^{-ad} \tag{6.3.4}$$

For the case that r_2=0, i.e. prism 2 is removed and the power output at prism 3 is P_{30}:

$$P_{30} = r_3[P(z_2)]e^{-ad} \tag{6.3.5}$$

$$\Delta P_3 = P_3 - P_{3o} = r_3r_2P(z_2)e^{-ad} \tag{6.3.6}$$

$$\frac{P_3P_{3o}}{\Delta P} = \frac{r_2P(z_2)r_3P(z_2)e^{-ad}}{r_2r_3P(z_2)e^{-ad}} = P(z_2) \tag{6.3.7}$$

From the last equation , it is seen that the expression for $P(z_2)$, the power propagating at z_2, has no r dependence in it. Therefore, $P(z_2)$ can be estimated without the knowledge of coupling coefficients, r_2 and r_3. Thus by moving the prism 2, i.e. by changing z_2, one can find the power along the different points in the waveguide. The loss rate was obtained from the plot of relative power(dB) vs. distance, and the relative power was calculated by using the following equation:

$$P_{rel}\ (dB) = 10\ \log\left(\frac{P}{P_o}\right) \qquad (6.3.8)$$

where P_0 is the propagating power level at the reference point, and P is the various propagating powers at different distances along the waveguide.

Figure 6.5 shows the plot of relative power level versus propagation distance for both 50GS and LP3 waveguide. The slope of each curve gives the propagation loss rate. The 50GS sol-gel glass waveguide has a loss rate of 3.31 dB/cm, and the LP3 LPCVD glass waveguide has a loss rate of 2.59 dB/cm. These loss rates are comparable to those have been reported in the literature for various thin films used as waveguides in integrated optics[Ostr78], as shown in Table 6.3.

The result from the sol-gel film is especially encouraging and open a new application for this multiple dip-coating approach. The film exhibits good optical quality and low loss, although each layer was prepared in an open environment without special substrate preparation, solution filtration, and clean room facilities.

There are two major types of losses which may contribute to the propagation loss in optical waveguides: absorption losses and scattering losses. The materials prepared in the present study are of very high purity and the major impurity ions are the hydroxyl ions, which don't absorb at 632.8nm. Moreover, the waveguide length used in the present study is

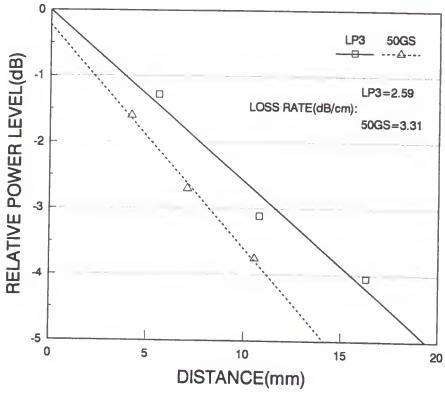

Figure 6.5 Propagation loss measurement for both the 50GS and the LP3 films at 632.8nm.

Material	Form	Fabrication technique	Index (6328 Å)	Loss at 6328 Å (dB/cm)
7059 glass	Amorphous	Sputtering	1.53–1.59	1 ~ 2
Barium silicate	Amorphous	Sputtering	1.57–1.67	1 ~ 5
Ta_2O_5	Amorphous	Sputtering	2.214	1
Nb_2O_5	Amorphous	Sputtering	2.276	1
ZnO	Polycrystalline	Sputtering	1.97	20
ZnS	Polycrystalline	evaporation	2.342	5
$LiTaO_3$	Polycrystalline	Sputtering	1.95–2.08	2
Glass	Amorphous	$AgNO_3$ exchange	1.52–1.65	0.1
Aluminosilicate glass	Amorphous	KNO_3 exchange	1.52–1.56	0.1
Silica	Amorphous	Li implantation	1.47	0.2

Characteristics of Organic Films

Material	Fabrication technique	Index 6328 Å	Loss at 6328 Å (dB/cm)
Polyurethane	Spin or dip coating	1.54–1.58	1
Epoxy (Araldite)	Spin or dip coating	1.581	0.3
KPR	Spin coating	1.615	7
Vinyltrimethylsilane	Plasma polymerization	1.537	0.01
Polyphenylsiloxane	Spincoating	1.56	1–2
Methylglycidyl methacrylate	Dip coating	1.515	0.2

much shorter compared to that usually used in optical fiber studies. Therefore, the major cause for the loss in these samples is attributed to scattering processes. Several types of scattering processes may contribute to the propagation loss in these cases:

(1). Intrinsic Rayleigh scattering(γ_{RS}) which is caused by the refractive index fluctuations(e.g. fluctuations in density, composition, or structure) that are small with respect to wavelength of light, and can be expressed in terms of fundamental material parameters[Tic90]

$$\gamma_{RS} \propto \frac{(B^2 Z_a^2 \beta T_g)}{\lambda^4 E_o^4} \qquad (6.3.9)$$

where Z_a is the anion valence, β is the isothermal compressibility, T_g the glass transition temperature, E_o the average energy gap, and B is a dimensionless structure factor given by

$$B = N_a d^3 \qquad (6.3.10)$$

where N_a is the volume density, and d is the first-neighbor bond length.

(2). Volume scattering which is caused by

inhomogeneities such as pinholes, micropores, and interfaces, within the volume of the waveguide, that introduce variations of refractive index along the path of the propagating light. The variation of refractive index causes the deflection of light, and the stray light may leak out of the waveguide because the change in propagation direction is no longer confined to the waveguide structure[Kin76].

(3). Surface scattering that is caused by irregularities in core/cladding boundary. When the boundary is not perfectly flat, the light traveling in the core is reflected irregularly. Some of the rays come off at different angles, giving rise to mode conversion, while others radiate away into the cladding because their angles of incidence exceed the critical angle for total reflection[Iga90].

According to the electron microscopy study, which was presented in last two chapters, the films prepared by both sol-gel and LPCVD method are composed of small particulates instead of containing a homogeneous and continuous phase. Therefore interfaces between particles, and surface irregularities have been observed. Moreover, pinholes and some large inclusions that were introduced into the film during film deposition may act as scattering centers in the waveguide.

6.4 Mode Profile Measurement

To calculate the field profiles, Maxwell's equations have

to be used under the appropriate boundary conditions. Considering a three-layer step-index planar waveguide with light propagating in yz plane along z direction with a propagation constant β (or with a phase velocity $v_p=\omega/\beta$), as is shown in Figure 6.6. By assuming the light wave in the film to be infinitely wide in the y direction so that $\partial/\partial y = 0$, the transverse electric field component for the TE mode E_y can be shown to satisfy the transverse Helmholz equation[Tie71]

$$\frac{d^2E_y}{dx^2} + (k_o^2n^2 - \beta^2)E_y = 0 \qquad (6.4.1)$$

The boundary conditions imposed by the waveguide structure demand that E_y(and thereby automatically H_x) and $\partial E_y/\partial x$(and thereby H_z) be continuous across the film boundaries at x=0 and x=d[Kog79]. For guided TE modes, the solution of Equ.(6.4.1) will be an exponentially decaying function for both x<0 and x>d, and an oscillatory function within d>x>0, which can be expressed as follows[Kog79]

$$E_{yc}(x) = E_f \cos\phi_c \; e^{\alpha cx} \qquad \text{for } x<0 \text{ (cladding)} \quad (6.4.2)$$

$$E_{yf}(x) = E_f \cos(kx-\phi_c) \qquad \text{for } 0<x<d \text{ (film)} \quad (6.4.3)$$

$$E_{ys}(x) = E_f \cos(kd-\phi_c) \; e^{-\alpha s(x-d)} \qquad \text{for } x>d \text{ (substrate)} \quad (6.4.4)$$

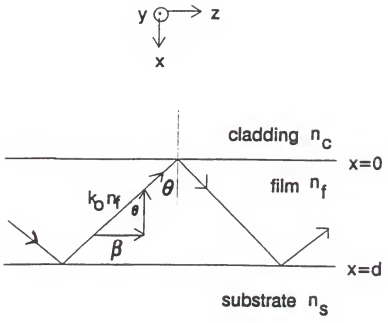

Figure 6.6 Ray path in a three layer step index waveguide.

where α_c= absorption coefficient of the cladding layer, and α_s= absorption coefficient of the substrate. The various constants may be expressed in terms of film parameters(n_f, n_s, n_c, d)[Ram89]

$$k = k_o\sqrt{n_f^2 - N^2} \tag{6.4.5}$$

$$\alpha_c = k_o\sqrt{N^2 - n_c^2} \tag{6.4.6}$$

$$\alpha_s = k_o\sqrt{N^2 - n_s^2} \tag{6.4.7}$$

Recalling the definition of various normalized parameters(i.e. b and V) and asymmetric parameter(a_{TE})

$$b = \frac{N^2 - n_s^2}{n_f^2 - n_s^2} \qquad 0 \le b \le 1 \tag{6.4.8}$$

$$V = k_o d\sqrt{n_f^2 - n_s^2} \tag{6.4.9}$$

$$a_{TE} = \frac{n_s^2 - n_c^2}{n_f^2 - n_s^2} \qquad 0 \le a \le \infty \tag{6.4.10}$$

and by defining x'=x/d and assuming E_f=1, the Equ.(6.4.2) ~(6.4.4) can be expressed as normalized field distribution equations in terms of these parameters(i.e. V, a, b, and x')[Ram89]

$$E_{yc}(x) = \cos\phi_c e^{V\sqrt{(a+b)}x'} \qquad for\ x'<0\ (cladding) \tag{6.4.11}$$

$$E_{yf}(x) = \cos(\phi_m x' - \phi_c) \qquad for\ 0<x'<1\ (film) \tag{6.4.12}$$

$$E_{ys}(x) = (-1)^m \cos\phi_s e^{V\sqrt{b}(1-x')} \qquad for\ x'>1\ (substrate) \tag{6.4.13}$$

Various phase shift terms(i.e. ϕ_m, ϕ_s, and ϕ_c) in Equ. (6.4.11)~ (6.4.13) may also be expressed in terms of film parameters[Ram89]

$$\phi_m = m\pi + \phi_s + \phi_c \tag{6.4.14}$$

$$\phi_s = \tan^{-1}[(1+q)\sqrt{\frac{b}{1-b}}\,)] \tag{6.4.15}$$

$$\phi_c = \tan^{-1}\left[\left(\frac{1+q}{1-aq}\right)\left(\sqrt{\frac{a+b}{1-b}}\right)\right] \qquad (6.4.16)$$

where q=0 for TE modes, and $q=(n_f^2/n_s^2)-1$ for TM modes. Therefore the normalized field distribution equations (6.4.11)~(6.4.13) can be expressed completely in terms of film parameters[Ram89]

$$E_{yc}(x) = \sqrt{\frac{1-b}{1+a}}\; e^{V\sqrt{(a+b)}\,x'} \qquad \textit{for } X'<0 \textit{ (cladding)} \qquad (6.4.17)$$

$$E_{yf}(x) = \left[\sqrt{\frac{1-b}{1+a}}\cos\left(V\sqrt{(1-b)}\;x'\right) + \sqrt{\frac{a+b}{1+a}}\sin\left(V\sqrt{(1-b)}\;x'\right)\right]$$

$$\text{for } 0<x'<1 \text{ (film)} \qquad (6.4.18)$$

$$E_{ys}(x) = (-1)^m\sqrt{1-b}\; e^{V\sqrt{b}\,(1-x')} \qquad \textit{for } x'>1 \textit{ (substrate)}$$

$$(6.4.19)$$

By inputing various film parameters(n_f, n_s, n_c, d, and λ_o), which may be obtained experimentally, the field distribution across the transverse direction(i.e. x direction), both within and beyond the waveguide structure can be calculated using Equ.(6.4.17)~ (6.4.19). The results of calculated field

distribution for TE0 and TE1 modes of 30GS waveguide are given in Figure 6.7.

The instantaneous power flux, both magnitude and direction, of electromagnetic energy is usually described by the Poynting vector(p_z)[Lee86]. For a step-index slab waveguide, the Poynting vector for TE mode can be expressed as

$$p_z = \frac{\beta}{2\omega\mu_o} |E_y|^2 \qquad (6.4.20)$$

which is basically taking the square of the field distribution functions and then multiplying with a constant.

The total power flow in a dielectric waveguide can be obtained by integrating from $-\infty$ to $+\infty$ in x direction,and it can be expressed as follows[Lee86]

$$P_z = \frac{\beta}{2\omega\mu_o} \left[\int_{-\infty}^{0} |E_{yc}|^2 dx + \int_0^d |E_{yf}|^2 dx + \int_d^{+\infty} |E_{ys}|^2 dx \right] \qquad (6.4.21)$$

The mode profile of the planar waveguide is measured using a near-field method, as described in section 3.2.10. This method consists of measuring the intensity distribution along the transverse direction (i.e. x direction) of the near-field image of a propagating mode, which was projected to the image plane from the end face of the waveguide by using a microscope objective. The results for the experimentally

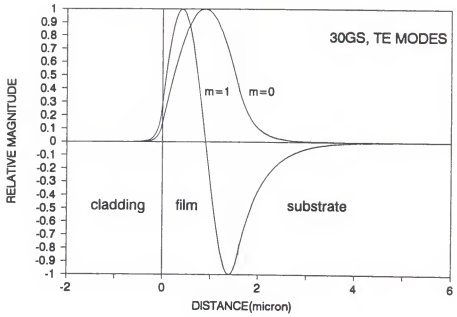

Figure 6.7 Calculated field profiles for m=0, and 1 TE modes of the 30GS film modeled as a step-index waveguide.

measured TE0 and TE1 mode are shown in Figure 6.8 and 6.9, respectively. The fluctuation of the intensity in Figure 6.8 near the edge of the waveguide is attributed to the scattering of light by the defect at the end face of the waveguide introduced during polishing. The intensity profile of TE1 mode, see Figure 6.9, contains two peaks as expected from the results of the calculated mode profile, as shown in Figure 6.10. However, the relative intensities of these two peaks are not comparable as predicted from Figure 6.10, which is based on a perfect step-index profile assumption. This indicates a slight variation of the index profile across the actual waveguide. The compositional uniformity across the 30GS film was analyzed by a Scanning Auger Electron Spectroscopy(AES), with Ar ion gun sputtering for depth profiling. The intensity of Si , Ge, and O were monitored with sputtering time. All the elements studied appear to be quite constant across the film even after five hours of sputtering, as shown in Figure 6.11. However, this analysis was complicated by the charging problem that is commonly encountered for dielectric materials, making extensive sputtering studies a difficult task. A possible reason for the deviation from a perfect step-index profile may be due to film microstructure, which may vary between the layers close to and far from the substrate. This could be examined by cross-sectional TEM. However, the problem was not considered

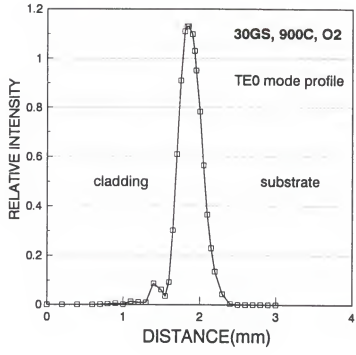

Figure 6.8 Experimentally measured TE0 mode profile(350x).

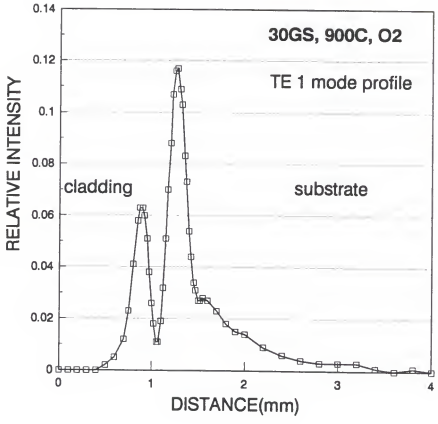

Figure 6.9 Experimentally measured TE1 mode profile(350x).

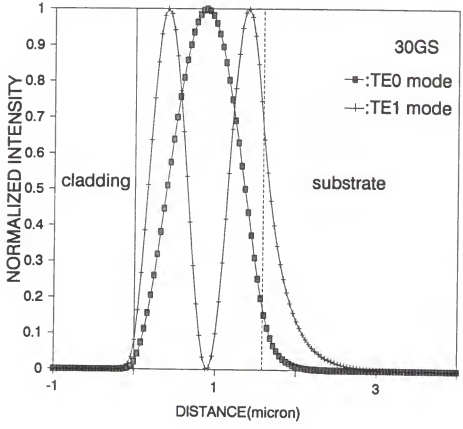

Figure 6.10 Calculated mode profiles for the 30GS film as a perfect step-index slab waveguide.

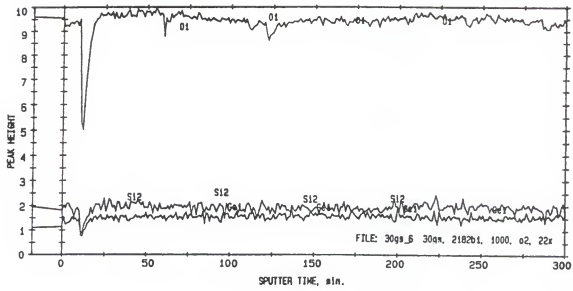

Figure 6.11 Scanning Auger (AES) composition profile analysis of the 30GS film.

significant.

Similarly, the field profile for TE0, TE1, and TE2 modes in LP3 film have been calculated and are shown in Figure 6.12. Each mode profile is experimentally measured and the results are given in Figure 6.13, 6.14, and 6.15 for TE0, TE1, and TE2 mode respectively. These mode profiles appear as predicted by calculated results of mode profiles, i.e. one peak for fundamental mode, two peaks for TE1 mode, and three peaks for TE2 mode as is shown in Figure 6.16. The relative intensity of the two peaks in TE1 mode profile are not comparable as predicted by the step-index model. Similar deviation is also observed in the measurement for TE2 mode, as shown in Figure 6.15.

The power confinement efficiency(EF) of each mode is obtained by calculating the ratio between the area below the intensity profile within the waveguide to that of the total intensity profile (i.e. including cladding, waveguide, and substrate) which may be expressed as

$$EF = \frac{\left(\int_0^d |E_{yf}|^2\, dx\right)}{\left(\int_{-\infty}^0 |E_{yc}|^2\, dx + \int_0^d |E_{yf}|^2 dx + \int_d^{+\infty} |E_{ys}|^2 dx\right)} \qquad (6.4.22)$$

The results are listed in Table 6.2 under the column EF.

The fact that EF decreases with increasing mode number is because more power is extending out beyond the boundaries of

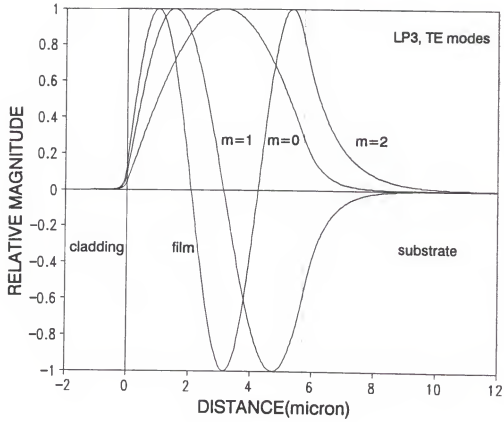

Figure 6.12 Calculated field profiles of TE0, TE1 and TE2 modes for the LP3 film as a step index waveguide.

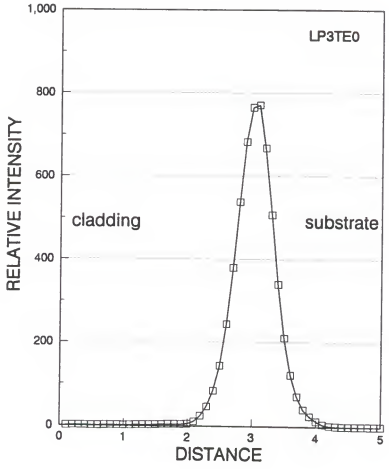

Figure 6.13 Experimentally measured TE0 mode profile(350x).

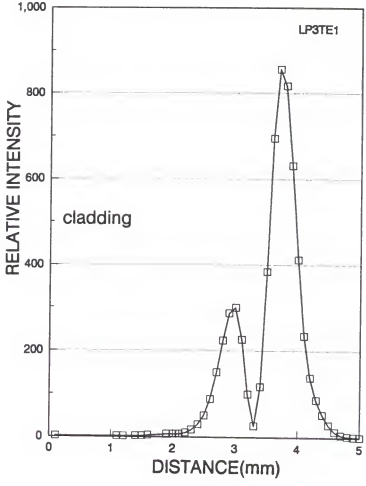

Figure 6.14 Experimentally measured TE1 mode profile(350x).

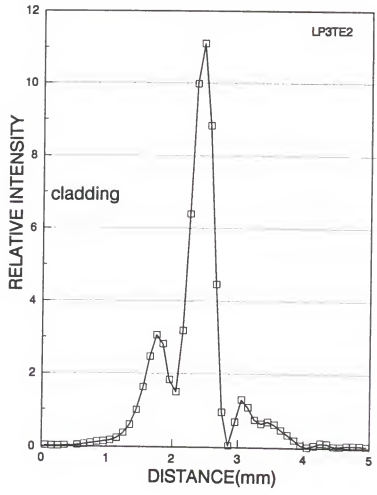

Figure 6.15 Experimentally measured TE2 mode profile(350x).

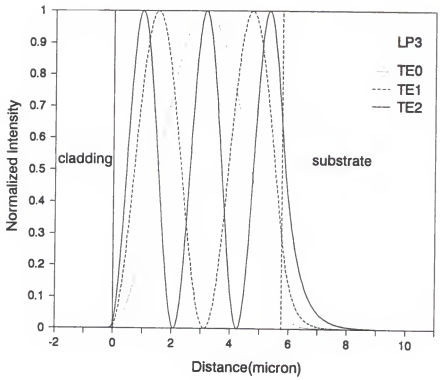

Figure 6.16 Calculated mode profiles for TE0, TE1, and TE2 modes of the LP3 film modeled as a perfect step-index slab waveguide.

the guiding film, which is clearly shown in the calculated mode profile plots in Figure 6.10 and Figure 6.16 for 30GS and LP3 waveguide, respectively.

CHAPTER VII

NONLINEAR OPTICAL MEASUREMENT

7.1 Introduction

The nonlinear properties of glasses are of paramount significance in areas where light intensities are in the order of 1 GW/cm^2. Two of these areas are high power laser-fusion(Fel73) and all-optical switching for information processing(Fri87). In the former the nonlinear properties have to be reduced (n_2 must be small) in order to limit the damage to optical glass components by self-induced focusing. For the latter case there is an increasing need for transparent materials in the 1-2 μm region with highly intensity dependent nonlinear refractive index coefficients which can withstand high optical peak powers.

The nonlinear optical phenomena in glasses may be divided into two categories. The first category includes phenomena in which the glass itself is responsible for the nonlinearity (intrinsic effect), such as nonlinear refractive index, multiphoton absorption, and stimulated Raman and Brillouin scattering. The other category includes glasses containing rare earth ions, semiconductor microcrystals, or organic dyes, where the nonlinearity is associated with the dopant and the

glass acts as a host(extrinsic effect) and its contribution is secondary. For intrinsic effects the composition and structure of the glass are of primary importance in controlling the nonlinearity.

In the present study, we investigate the optical nonlinearity of glass films with various compositions prepared by the sol-gel method. The samples used are listed in Table 7.1. The GeO_2-TiO_2 films were prepared by using a procedure similar to that for fabricating the SiO_2-GeO_2 system as described in section 3.1.1, except that titanium isopropoxide($Ti(OC_3H_7)_4$, Aldrich) and germanium 2-methoxy-ethoxide($Ge(OCH_2CH_2OCH_3)_4$) were used as precursors.

Both GeO_2 and TiO_2 are important oxide components used in various optical materials to increase the refractive index. By varying the amount of GeO_2 or TiO_2 added to SiO_2 we may span the linear optical properties, refractive index and Abbe number, from Crown glasses(ν_D>50) to Flint glasses(ν_D<50).

6.2 Semi-Empirical Model: BGO Equation

The most commonly used model for predicting the nonlinear third order optical susceptibility of transparent optical glass was developed by Boling, Glass and Owyoung(Bol78). This model assumes a single component which determines linear and nonlinear indices. For oxide glasses this component is oxygen. A semi-empirical equation(i.e. BGO equation) relating linear refractive index and dispersion to nonlinear index was

Table 7.1 Sol-Gel Thin Films for THG Measurement.

Sample	Temp.(°C)	Index(n_1)	Thickness(μm)
B30GS(22x)	700, O_2	1.44	1.327
C50GS(20x)	700, O_2	1.53	0.76
D30GT(22x)	200, O_2	1.86	0.25
E50GT(22x)	200, O_2	1.84	0.45

derived as follows

$$n_2(10^{-13}esu) = \frac{k(n_D-1)(n_D^2+2)^2}{\nu_D\sqrt{[1.517+(n_D^2+2)(n_D+1)\frac{\nu_D}{6n_D}]}} \quad (7.2.1)$$

where K=68, ν_D=Abbe number=$(n_D-1)/(n_F-n_C)$, λ_F=486nm, λ_D=587nm, and λ_C=656nm. The equation has proven accurate in predicting and describing the NLO coefficient of many materials(Ada87).

Figure 7.1(Sim91) shows the dependence of the nonlinear index on linear index and dispersion calculated from the BGO equation. The figure clearly shows a strong dependence on dispersion, indicative of the effect of a nearby resonance(e.g. possibly near 1/2 E_g or E_g).

In order to calculate n_2 using the BGO equation, both the linear refractive index(n_1) and the Abbe number(ν_D) must be known. An additive model developed by Huggins and Sun(Hug43) is applied to compute the material density, linear refractive index as well as Abbe number of the glass films we investigate in the present study.

In the Huggins method, the oxides composing a given glass are expressed in parts by weight(f_M) instead of weight percent(wt%), the former is defined as

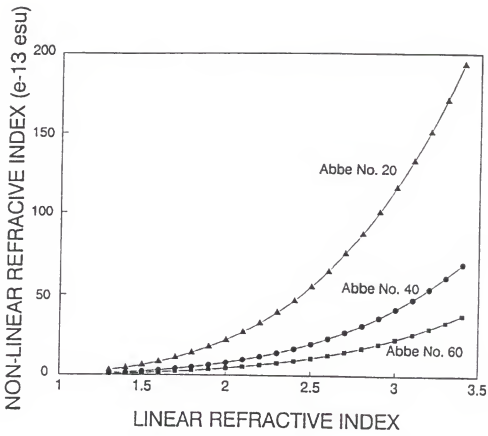

Figure 7.1 Nonlinear refractive index(n_2) versus linear refractive index(n_1) for various Abbe numbers, calculated using BGO equation[Sim91].

$$f_M = \frac{p_M}{100} \qquad , \sum f_M = 1 \tag{7.2.2}$$

A part by weight f_M is therefore equal to one hundredth of the amount of oxide expressed in weight percent, p_M.

The density(d) of the oxide glass of an arbitrary composition may be calculated from the following equation

$$\frac{1}{d} = \sum (v_M f_M) \tag{7.2.3}$$

where v_M is specific volume of each oxide component. In the present work it has been assumed that for the entire composition range of binary oxide glass(e.g. SiO_2-GeO_2, GeO_2-TiO_2, or SiO_2-TiO_2) the structural units remain unchanged and form a solid solution as has been described in section 4.2.5. Therefore the specific volume of each oxide component is assumed to be constant and is calculated from the reported density data in the literature, namely, d_{SiO2}=2.202 g/cm^3, d_{GeO2}=3.604 g/cm^3[Huan78], and d_{TiO2}=3.8 g/cm^3 [Vol88]. The v_M values which are calculated using the relation v_M=1/d are given in Table 7.2.

The linear refractive index n_λ for an arbitrary wavelength, λ, can be computed from the following equation(Hug43)

Table 7.2 Various Constants Used to Calculate the Refractive Index and the Abbe Number for SiO_2-GeO_2, GeO_2-TiO_2, and SiO_2-TiO_2 Sol-Gel Glass Systems.

Oxide	v_M	$e_M^* 10^{-8}$	$g_M^* 10^{-8}$
SiO_2	0.4541	29.81	145.69
GeO_2	0.2775	13.90	85.99
TiO_2	0.2632	11.49	39.6

* After Huggins and Sun(Hug43)

$$n_\lambda = 1 + d(\sum r_{M,\lambda} f_M) \qquad (7.2.4)$$

where $r_{M,\lambda}$ is defined for most of the oxides(except PbO, CaO, and BaO) as

$$r_{M,\lambda} = e_M[\frac{1}{g_M - \frac{1}{\lambda^2}} - 48x10^{-6}\lambda^2] \qquad (7.2.5)$$

The values of $e_M x10^{-8}$ and $g_M x10^{-8}$ are reproduced from Huggins and Sun's paper(Hug43) and listed in Table 7.2.

The Abbe number(or relative dispersion) of the glass can be obtained by using the following equation

$$\nu_D = \frac{n_D - 1}{n_F - n_C} \qquad (7.2.6)$$

where n_D=refractive index for sodium D line at 589nm, n_F and n_C are index for Hydrogen F and C lines at 486nm and 656 nm respectively, which can be computed using equation (7.2.4).

Figure 7.2 shows the calculated linear refractive index at 632.8nm(HeNe laser wavelength used in the ellipsometry measurements) by using the additive model for three binary oxide glass systems(e.g. SiO_2-GeO_2, GeO_2-TiO_2, and SiO_2-TiO_2) of various compositions. The curves are nearly linear for these

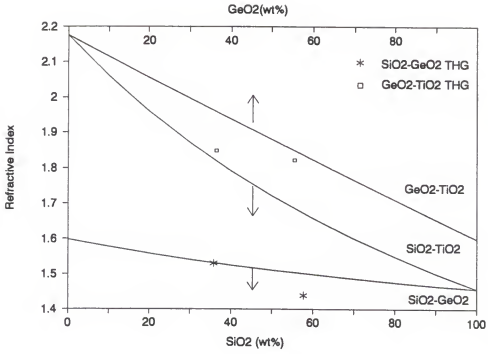

Figure 7.2 Calculated refractive indices for various binary oxide glass systems using an additive model; □: data for GeO_2-TiO_2 THG samples, *: data for SiO_2-GeO_2 THG samples.

binary systems with an index of 1.457 for pure glassy SiO_2, 1.60 for pure GeO_2 glass, and 2.176 for pure TiO_2 in a glassy state. Titania has the smallest specific volume among the oxides calculated, which results in a rapid increase of the density and therefore an increase in the linear refractive index with the addition of TiO_2 in the material.

The experimentally measured refractive index of the sol-gel binary glass film used in the THG measurements are shown in Figure 7.2 as asterisk symbols for GeO_2-SiO_2 samples and as hollow squares for 30GT and 50GT films. It appears that only 50GS film is close to the theoretical value, while the other samples exhibit indices lower than the predicted values, indicating that these samples (30GS, 30GT and 50GT) may not be fully densified. This is not unexpected considering that the heat treatment temperatures for these films are not high, especially for GeO_2-TiO_2 samples(only heated at 200°C).

The computed results of Abbe numbers of these binary oxides are shown in Figure 7.3. Titania has the largest dispersion which leads to a small Abbe number. The addition of TiO_2 into the material causes a rapid decrease of Abbe number. The computed Abbe number for pure glassy oxides are ν_{SiO2}= 67.86, ν_{GeO2}=41.88, and ν_{TiO2}=18.78.

6.3 Third Harmonic Generation(THG) Measurement

As mentioned in section 3.2.11, a Third-Harmonic-Generation (THG) interference fringe method was used to

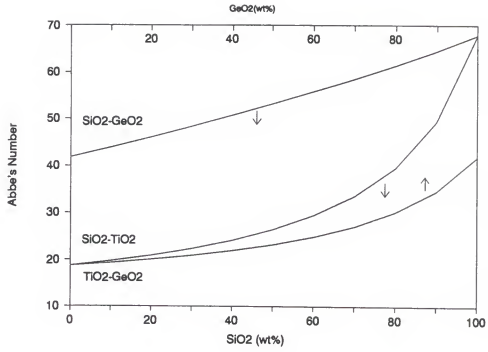

Figure 7.3 Calculated Abbe numbers for various binary oxide glass systems using an additive model.

measure the nonlinearity of the films. The measurement and the analysis of the THG fringes were conducted by Dr. W.E. Torruellas in Dr. G. Stegeman's group at the University of Arizona. To optimally use THG method it is desirable to have the product of the THG coherence length(l_c) of the substrate and the substrate nonlinearity be comparable to the product of the film thickness and its nonlinear susceptibility($\chi^{(3)}$). The coherence length in this case means the distance that the fundamental wave and the third harmonic wave may travel without coming out of phase, as the beginning of destructive interference diminishes the amplitude of the TH wave. Since the THG coherence length of fused silica at 1.579μm is approximately 15μm[Tor91a], the third harmonic optical fields for the film and the substrate are comparable for ~1μm films. Both the magnitude and the phase of $\chi^{(3)}$ could be measured from the shift and the offset of the interference fringes[Tor91a], an example of which for sample B30GS is shown in Figure 7.4.

Figure 7.5 shows the THG results measured at 1.579μm for various sol-gel film compositions. The data for SiO_2-TiO_2 are taken from Torruellas et al.'s recent work[Tor91b]. As can be seen, the results of the SiO_2-GeO_2 and SiO_2-TiO_2 films follows Boling's model appropriately. All the n_2 values measured are within the region between the curves corresponding to ν_D=20 and ν_D=60, which is the typical range of Abbe numbers for these binary oxide glasses.

The results of the calculated nonlinear refractive

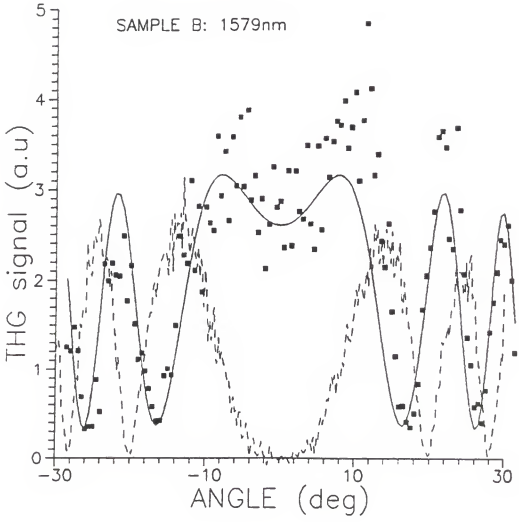

Figure 7.4 THG interference fringes of 30GS film at 1.579 μm. ---:the fringe of bare SiO_2 substrate, ■: the experimental data points, and the solid line is the best fit to the interference fringe[Tor91].

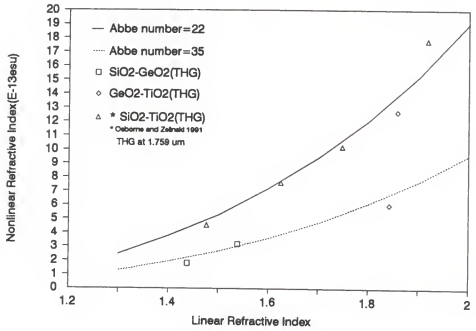

Figure 7.5 n_2 is plotted as a function of n_1. Solid line: calculated values, markers:the experimental data. n_1 for SiO_2-TiO_2 are calculated using the additive model.

index(n_{2B}) using the BGO equation and that from THG measurements for 1.579μm (n_{2THG}) are given in Table 7.3. The linear refractive index and Abbe number of each film are computed using the additive model described previously. The THG data for SiO_2(i.e. $0.85x10^{-13}$ esu) is taken from Weber et al.'s results measured at 1.064μm(Web78). The results of the THG/SiO_2 ratio are taken from Torruellas's work[Tor91a]. The comparison between the calculated n_2 values(n_{2B}) and the measured nonlinear indices(n_{2THG}) are plotted as shown in Figure 7.6. Although the measured values seems to follow the predicted values quite closely, in most of the cases the measured values are slightly higher than the calculated values, except 30GS and two GeO_2-TiO_2 samples. The fact that both GeO_2-TiO_2 films possess much lower values compared to the predicted ones is attributed to the possibility that these films are still quite porous, since they were only heat treated at 200 °C to prevent crystallization of the film. The measured values of n_2 for the SiO_2-TiO_2 system appears to be slightly higher than the predicted values by the Boling model. This can be due to the fact that the model assumes oxygen ions as the only dominant constituent for both linear and nonlinear indices. When the material contains heavy ions, especially ions with unfilled d-shells, the d-electrons will make a significant contribution to the linear and nonlinear polarizabilities[Bol78]. Therefore, the addition of titania to the glass may cause some deviation from the prediction of

Table 7.3 Comparison Between the Calculated Nonlinear Refractive Index(n_{2B}) Using BGO Equation and from THG Measurement (n_{2THG}).

SiO_2 (wt%)	GeO_2	TiO_2	n_d	υ_d	n_{2B}(esu)	*THG/SiO_2	@n_{2THG}(esu)
100	0	0	1.459	67.86	0.87×10^{-13}	1	0.85×10^{-13}
57.3	42.7	0	1.523	56.54	1.4×10^{-13}	2	1.7×10^{-13}
36.5	63.5	0	1.537	49.15	1.8×10^{-13}	4	3.4×10^{-13}
0	56.7	43.3	1.868	23.79	13×10^{-13}	7	6.0×10^{-13}
0	36.0	64.0	1.982	20.5	20×10^{-13}	15	12.7×10^{-13}
93.5	0	6.5	1.474	61.49	1.1×10^{-13}	5	4.2×10^{-13}
63.7	0	36.3	1.625	32.01	4.4×10^{-13}	9	7.6×10^{-13}
42.9	0	57.1	1.748	25.75	8.5×1^{-13}	12	10.2×10^{-13}
24.4	0	75.6	1.918	21.74	16×10^{-13}	21	17.8×10^{-13}

* Data reported by W.E. Torruellas. The SiO_2-TiO_2 samples were prepared at the University of Arizona(Z. Osborne and B.J. Zelinski)
@ Data calculated by J.H. Simmons.(Sim90)

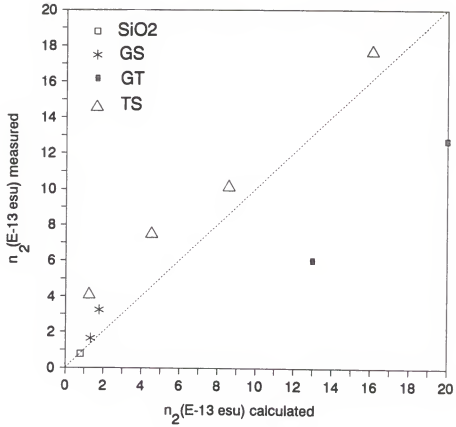

Figure 7.6 Comparison between the predicted n_2 values according to BGO model and that measured by THG measurement.

the model.

Figure 7.7[Tor91a] shows the relative magnitude of $\chi^{(3)}(3\omega)$ compared to pure fused silica at three different wavelengths in the near infrared for 50GT and 50ST films. In the case of the SiO_2-TiO_2 sample(whose bandedge is at ~350nm) the value for $\chi^{(3)}$ remains nearly constant until the frequency approaches a resonance at $3\omega_{0.953}$. Figure 7.8 shows calculated dispersion curves for the THG samples using the additive model. As can be seen in the Figure 7.8, all the TiO_2-containing glasses start to approach resonance at around 350nm while SiO_2-GeO_2 glasses resonate at frequencies below 200nm(unless some defect bands exist in the material e.g. 245nm, 325nm etc.). This can also be seen in the UV-VIS absorption spectra in Figure 7.9 for some of the films. The resonance enhancement on the measured $\chi^{(3)}$ has been observed in various measurements on organic films[Kaj83].

All the other samples containing GeO_2 in this study possess similar dispersion as film 50GT as are shown in Figure 7.10. Due to the fact that only a limited number of wavelengths were measured on these films, the reason(s) for the drop of $\chi^{(3)}$ at 0.953μm for all the GeO_2-containing samples is not known. It has been observed [Tor91a] that the GeO_2 based samples have a stronger tendency to damage at 0.957μm than the SiO_2-TiO_2 ones. The pump energy used for those samples thus was near the detection limit of the THG measurement at that wavelength. Therefore the error of the

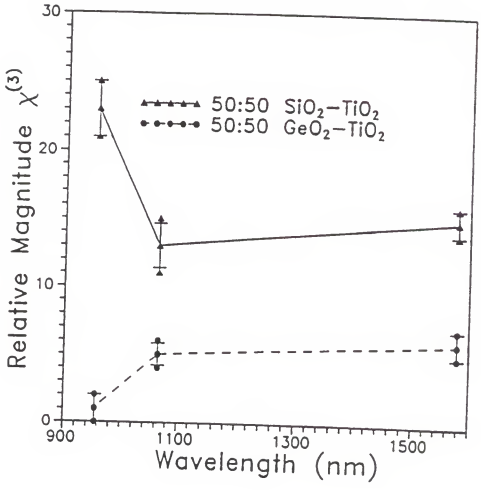

Figure 7.7 The relative magnitude of $\chi^{(3)}(3\omega)$ compared to pure fused-SiO_2 is plotted as a function of the fundamental wavelength for 50GT and 50ST samples, at 0.957μm, 1.064μm, and 1.597μm[Tor91].

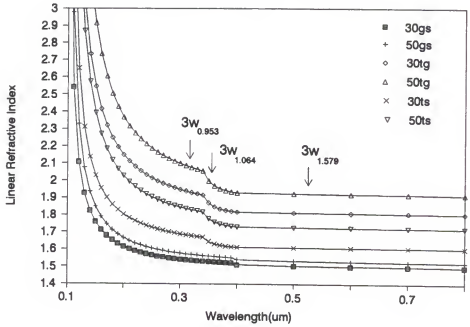

Figure 7.8 Calculated dispersion curves of various samples used in THG measurement using an additive model.

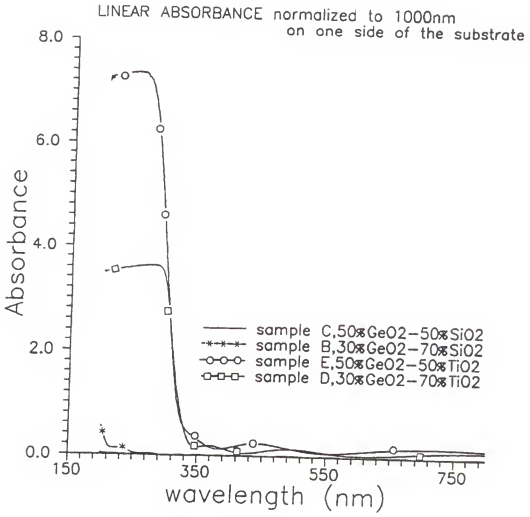

Figure 7.9 The linear absorbance for various THG samples measured by UV-Vis spectroscopy, spectra are normalized to the same thickness[Tor91c].

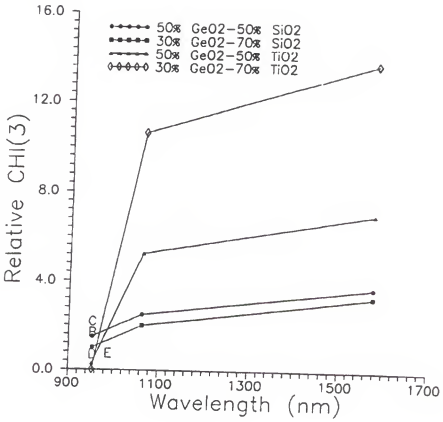

Figure 7.10 The relative magnitude of $\chi^{(3)}(3\omega)$ compared to pure fused silica is plotted as a function of the fundamental wavelength for various THG samples[Tor91c].

measurement at that wavelength may be large. If the drop of $\chi^{(3)}$ at 0.957 μm for GeO_2-containing samples is real, we speculate that it is possible that the THG process is exhibiting a similar nonlinear index oscillation near the resonance frequencies as seen in a two-photon-absorption process(see Figure 7.11[Sim91]), and we are measuring the dip in that dispersion curve. However, more complete dispersion studies need to be conducted in order to draw a final conclusion.

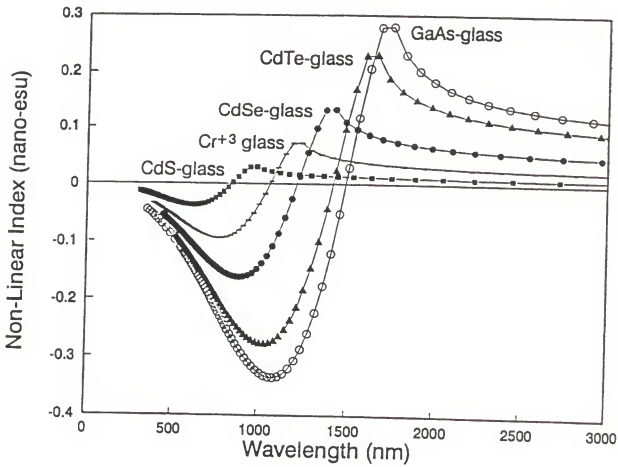

Figure 7.11 Plot of the two-photon-absorption induced nonlinearity for materials with different bandgap and impurity absorption energies [Sim91].

CHAPTER VIII

SUMMARY AND CONCLUSIONS

The present study has for the first time successfully demonstrated the feasibility of employing both sol-gel multiple dip-coating and low pressure chemical vapor deposition(LPCVD), in the production of high quality GeO_2-SiO_2 thin films with various germania contents. Planar view transmission electron microscopy has shown that the microstructure of the sol-gel film consists of very fine particles in the size range of 10nm, while the LPCVD films are composed of small particulates of around 30nm to 100nm size range depending upon the deposition condition.

In the sol-gel technique, several germanium alkoxides with higher alkyl groups have been synthesized from $GeCl_4$ using a combination of an ammonia method and an alcohol-interchange technique. Germanium 2-methoxy-ethoxide was routinely used in the current study to prepare stable binary GeO_2-SiO_2 sols for film deposition, with GeO_2 content between 10mol% to 50 mol%. A small amount of hydroxy-propyl-cellulose(HPC) was added to the sols as an independent viscosity adjusting agent to facilitate the multiple dipping process. This resulted in films of improved thickness

uniformity.

According to the thermal analysis of the organic additive in GeO_2-SiO_2 gels, the organics may be removed during heat-treatment in a temperature range of 200 to 600°C. Densification behavior of the films was followed by monitoring the change in refractive index as a function of the heat treatment temperature. All of the sol-gel samples exhibited an index decrease in the temperature range between 200 to 600°C due to the removal of the organics. This is then followed by an increase in the refractive index indicating densification of the film. The densification temperature appears to increase with decreasing GeO_2 content. The refractive index difference between the sol-gel films and the SiO_2 substrate may be tailored by controlling the film composition and the extent of densification. The refractive indices of the GeO_2-SiO_2 films span from 1.458 to 1.61, corresponding to pure SiO_2 and pure GeO_2 glass, respectively. Its composition dependence follows that predicted by the Lorentz-Lorenz model.

Both single and multimode waveguides have been fabricated by the sol-gel process. Using a three-prism loss measurement technique, the propagation loss of the $50GeO_2$-$50SiO_2$ single mode waveguide was found to be 3.31 dB/cm. These losses are attributed to various scattering processes, caused by surface roughness and pinholes in the film.

Vibrational spectroscopy revealed the existence of Si-O-

Ge linkages in GeO_2-SiO_2 glass network. The addition of GeO_2 in SiO_2 caused a decrease in the size of both the D1 and D2 defect bands in the SiO_2 Raman spectra. A preferential decrease of the 800 cm^{-1} absorption band in the FTIR spectra, due to the Si-O-Si stretching mode, was also observed.

In the LPCVD process, dilute GeH_4/Ar and pure silane(SiH_4) gasses were used as reactants. The GeO_2-SiO_2 film was deposited by an oxidation reaction with O_2 in the temperature range of 400~450°C . Appropriate film deposition conditions were found to produce waveguiding films using reasonable deposition rates. The GeO_2 content of the films prepared using this technique were limited due to the use of a very dilute GeH_4 reactant and an inherently low deposition rate of GeO_2 in this process.

Analysis of the UV-Vis spectra revealed that these films possess a high concentration of oxygen deficient centers compared to fused SiO_2. This has been extensively reported for oxide films deposited under vacuum.

Vibrational spectroscopic studies confirmed the existence of Si-O-Ge linkages in the binary glass network. The structure of the LPCVD films appears to be dominated by D1 and D2 defect structures, when comparing the Raman spectra of the LP3 film to those of SiO_2 after neutron irradiation. This is attributed mainly to the low deposition temperature used in the process.

The propagation loss of the LP3 waveguide is 2.59 dB/cm.

The scattering processes caused by surface roughness and some large particulate inclusions in the film are believed to be responsible for this loss.

The mode indices of the waveguides were measured using a prism coupling technique. In comparing the experimentally measured mode index to that calculated based upon a step-index profile assumption, good agreement was found. Thus the refractive index profile of the films prepared by both the sol-gel and the LPCVD process may be approximated by a step-index profile.

The theoretical electromagnetic field distribution profile for a step-index planar waveguide has been calculated. The propagating mode profile in the GeO_2-SiO_2 waveguide is experimentally measured, using a near field technique, and compared to the computed mode profiles. The analysis revealed that the measured mode profiles substantiate the step-index planar waveguide model. However, slight discrepancies in peak heights between the calculated and experimentally determined profiles have been observed. The deviations in the mode intensity may be caused by the surface scattering at the end face of the waveguide due to defects introduced during polishing and/or possible small index fluctuation across the deposited film.

The nonlinear refractive index of the sol-gel films (GeO_2-SiO_2, and GeO_2-TiO_2) was measured using a THG interferometry fringe technique in cooperation with Dr. W.E.

Torruellas and Dr. G. Stegeman at the University of Arizona. Analysis of both THG(n_{2THG}) and linear index(n_l) measurement results shows that the relation between n_{2THG} and n_l follows that predicted by the empirical BGO equation.

The BGO model has been used to predict the nonlinear refractive indices(n_{2B}) of various binary oxide glasses (i.e. GeO_2-SiO_2, GeO_2-TiO_2, and SiO_2-TiO_2). In order to compute n_{2B}, an additive model was used to calculate linear refractive indices and Abbe numbers of the materials, assuming a constant specific volume for each individual oxide component (i.e. SiO_2, GeO_2, and TiO_2). The deviation of the n_{2THG} values of TiO_2-containing glasses from the n_{2B} values is attributed to the high polarizability of Ti cations.

Based upon the limited measurement of the $\chi^{(3)}$ dispersion in these binary films, the SiO_2-TiO_2 films show a sharp increase of $\chi^{(3)}$ in the low wavelength side, which is attributed to a resonant enhancement of the third harmonic wave. This agrees with the calculated n_l dispersion curves using the additive model. It is also confirmed by the UV-Vis measurement which showed a large absorption band starting at around 350nm.

The unusual decrease of $\chi^{(3)}$ for both GeO_2-SiO_2 and GeO_2-TiO_2 systems on the short wavelength region is not understood. However, the THG process is speculated to exhibit a similar n_2 oscillation near resonance frequencies similar to that seen in the Two-Photon-Absorption process. Thus, the approach to

resonance can cause the measured dip in the n_2 dispersion curve. However, a more systematic dispersion study is required before a final conclusion can be drawn.

In conclusion, it is possible to form suitable optical waveguides in the GeO_2-SiO_2 system by both sol-gel multi-coating and LPCVD approaches. The sol-gel process offers a broad range of compositions and therefore numerical apertures while the LPCVD is limited to low GeO_2 concentrations. We have demonstrated that the sol-gel multiple coating process with up to 72 layers can be used to form films of reasonable uniformity when using an organic additive to control solution viscosity during dipping. The losses measured in waveguides made by the sol-gel process are mostly due to scattering and could be reduced by (1) processing under clean room conditions and (2) using a highly automated dip-coating process to maintain uniform thickness over the film. The losses in the LPCVD waveguide appear to result from scattering losses also, although hydroxyl content may also be a problem. Both may be reduced by high temperature anneals.

REFERENCES

Ada87 R. Adair, L.L. Chase, and S.A. Payne, J. Optical Soc. Amer., B4, 875, 1987.

Ait90 J.S. Aitchinson, A.M. Weiner, Y. Silerberg, M.K. Oliver, J.L. Jackel, D.E. Leaird, E.M. Vogel, P.W.E. Smith, Opt. Lett., 15, 471, 1990.

Alf86 R.C. Alferness, Science, 234, 825, 1986.

And89 D.Z. Anderson, Proc. SPIE, 1148, 186, 1989.

Arn73 G.W. Arnold, IEEE Trans. Nucl. Sci., NS-20, 220, 1973.

Azz77 R.M.A. Azzam and N.M. Bashara, Ellipsometry and Polarized Light, North Holland, NewYork, 1977.

Bar90 G. Barbarrossa, P.J.R. Laybourn, G. Maxwell, Proc. of the 2nd. Intern. Ceramic Sci. & Tech. Cong., Nov. 1990, Orlando, FL, USA.

Barr50 R.M. Barrer, and L. Hinds, Nature, 166, 562, 1950.

Bat72 J.B. Bates, R.W. Hendricks, and L.B. Shaffer, J. Chem. Phys., 56, 1910, 1972.

Bel72 R.J. Bell, and P. Dean, Discuss. Faraday Soc., 50, 55,1970.

Ben87 B.R. Bennett, J.P. Lorenzo, and K. Vaccaro, Appl. Phys. Lett., 50, 197, 1987.

Ber64 D.W. Berreman, Bell Syst. Tech. J., 43, 1469, 1964.

Blo65 N. Bloembergen, Nonlinear Optics, eds. Benjamin Pub. Co., 1965.

Blo89 K.L. Blow, N.J. Duran, and B.K. Nayer, Opt. Lett., 14, 754, 1989.

Bol78 N.L. Boling, A.J. Glass, and A. Owyoung, IEEE J. Quantum Electron., QE-14, 601, 1978.

Boo89 B.L. Booth, J. Lightwave. Tech., 7, 10, 1445, 1989.

Bor69 N.F. Borrelli, Phys. and Chem. of Glass, 10, 2, 43, 1969.

Boy82 P.K.Boyer, G.A. Roche, W.H. Ritchie, and G.J. Collins, Appl. Phys. Lett., 40, 716, 1982.

Bra53 D.C. Bradley, L.J. Kay, and W. Wardlaw, Chemistry and Industry, 746, 1953.

Bra56 D.C. Bradley, L.J. Kay, and W.W. Wardlaw, J. of Chem. Soc., 4916, 1956.

Bri80 T.J. Bridges, J.S. Hasiak, and A.P. Strand, Opt. Lett., 5, 85, 1980.

Bri88a C.J. Brinker, D.E. Clark, and D.R. Ulrich, Better Ceramics Through Chemistry III, Mat. Res. Soc. Symp. Proc., 121, MRS Pittsburg, PA, 1988.

Bri88b C.J. Brinker, A.J. Hurd, and K.J. Ward, in Ultrastructure Processing of Advanced Ceramics, ed. J.D. Mackenzie, and D.R. Ulrich, Wiley, New York, 1988.

Cal87 B. Carlson, Photonic Spectra, 152, 1987.

Chm89 A. Chmel, A.A. Kharohak, and K.N. Kuksenko, J. of Non-Crystal. Solids, 108, 194, 1989.

Cip74 J. Cipriani, S. Racine, R. Dupeyrat, H. Hasmonay, M. Dupeyrat, Y. Levy, and C. Imbert, Opt. Commum., 11, 70, 1974.

Coh58 A.J. Cohen, and H.L. Smith, J. Phys. Chem. Solids, 7, 301, 1958.

Con67 E.U. Condon, and H. Odishaw, Handbook of Physics, McGraw-Hill, New York, 1967.

Dia89 E.M. Dianov, P.G. Kazanskii, and D.V. Stepanov, Sov. J. Quant. Elec., 19, 575, 1989.

Die90 M.B.J. Diemeer, F.M.M. Suyten, E.S. Trommel, A. McDonach, J.M. Copeland, L.W. Jenneskens, W.H.G. Horsthnis, Electron. Lett., 26, 6, 379, 1990.

Eag62 C.C. Eaglesfield, Proc. IEE, 109B, 26, 1962.

Ebe46 M. Ebelmen, Ann. Chimie Phys., 16, 129, 1846.

Ebe47 M. Ebelmen, C. R. Acad. Sci., 25, 845, 1847.

Ewe35 R.H. Ewell, and H. Insley, J. Res. NBS, 15, 173, 1935.

Fel73 A. Feldman, D. Horowitz, and R.M. Waxler, IEEE J. of Quantum Electronics, QE-9, 1054, 1973.

Fra61 P.A. Franken, A.E. Hill, C.W. Peters, and C. Weinreich, Phys. Rev. Lett., 7, 118,1961.

Fri87 S.R. Friberg, and P.W. Smith, IEEE J. of Quantum Electronics, QE-23, 2089, 1987.

Gae86 Gaetner, User's Manual for Gaetner Manual Ellipsometer, 1986.

Gal78 F.L. Galeener, W.E. Stutius, in Proc. of the 6th Intern. Conf. on Raman Spect., 502, Bangalore, India, Sep. 1978.

Gal85 F.L. Galeener, J. Non-Crystal. Solids, 71, 373, 1985.

Gar58a V. Garino-Carina, Verres Refract., 6, 313, 1958.

Gar58b V. Garino-Canino, Comptes Rendus Acad. Sci., 247, 593, 1958.

Gar86 E. Garmire, in Electromagnetic Surface Excitations, ed. by R.F. Wallis and G.I. Stegeman, Springer,1986.

Gef51 W. Geffcken, Glastech. Ber., 24, 6, 143, 1951.

Gia73 T.G. Giallorenzi, E.J. West, R. Kirk, R. Ginther, and R.A. Andrews, Appl. Opt., 12, 1240, 1973.

Goe69 J.E. Goell, and R.D. Standley, Bell Syst. Tech. J., 48, 3445, 1969.

Gra85 P.B. Grabiec, J. PrzyLuski, Surface Tech., 25, 307, 1985.

Grah64 T. Graham, J. Chem. Soc., 17, 318, 1864.

Gri90 D.L. Griscom, in Glass:Science and Technology, 4B, 151, 1990.

Hal86 D.G. Hall, Photonic Spectra, 87, 1986.

Han80 F. Hanawa, S. Sudo, M. Kawachi, and M. Nakahara, Electron. Lett., 16, 699, 1980.

Han90 D.P. Hand, and P. St. J. Russell, Opt. Lett, 15, 102, 1990.

Hen72 J.M. Henis, G.W. Stewart, M.K. Tripodi, and G.P. Gaspar, J. Chem. Phys, 57, 389, 1972.

Hen90 L.L. Hench and J.K. West, Chem. Rev., 90, 33, 1990.

Hib90a Y. Hibino, V. Mizrahi, and G.I. Stegeman, Elect. Lett., 26, 1578, 1990.

Hib90b Y.Hibino, V. Mizrahi, and G.I. Stegeman, Appl. Phys. Lett. 1990 in press.

Hil78 K.O. Hill, Y. Fujii, D.C. Johnson, and B.S. Kawasaki, Appl. Phys. Lett., 32, 647, 1978.

Hua85 A.S. Huang, Y. Arie, C.C. Neil, and J.M. Hammer, Appl. Opt., 24, 4404, 1985.

Huan78 Y.Y. Huang, A. Sarkar, and P.C. Schultz, J. of Non-crystal. Solids, 27, 29, 1978.

Huff85 M. Huffman, P. McMillan, J. of Non-Crystal. Solids, 76, 369, 1985.

Huf86 M. Huffman, A. Navrotsky, F.S. Pintchovski, J. Electrochem. Soc., 133, 2, 431, 1986.

Hug43 M.L. Huggins, and K.H. Sun, J. of Amer. Ceram. Soc., 26, 4, 1943.

Hut88 L.D. Hutchson, Opt. News, 14, 8, 1988.

Iga90 K. Iga, Y.Suematsu, Introduction to Optical Fiber Communications, John Wiley & Sons, 1982, p 44.

Ile55 R.K. Iler, The Chemistry of Silica, Wiley, New York, 1955.

Iza72 T. Izawa, and H. Nakagome, Appl. Phys. Lett., 21, 584, 1972.

Iza79 T. Izawa, S. Sudo, and F. Hanawa, Trans. IECE Jpn., E62, 11, 779, 1979.

Jac85 J.M. Jackson, M.E. Wells, G. Kordas, D.L. Kinser, and R.A. Weesks, Appl. Phys., 58, 6, 2308, 1985.

Jcp88 JCPD-ICDD file, card number 36-1463, 1988.

Joh82 W.E. Johnson, and L.A. Schlie, Appl. Phys. Lett., 40, 798, 1982.

Kaj83 F. Kajzar, J. Messier, J. Zyss, and I. Ledoux, Opt. Commun., 45, 133, 1983.

Kaj86 F. Kajzar, and J. Messier, Electron. Lett., 22, 1230, 1986.

Kaj87 F. Kajzar, and J. Messier, in Nonlinear Optical Properties of Organic Molecules and Crystals, vol.2, ed. D.S. Chemla, J. Zyss, Academic Press, 51, 1987.

Kam74 I.P. Kaminow, and J.R. Carruthers, Appl. Phys. Lett., 22, 326, 1973.

Kas89 R. Kashyap, B.J. Ainslie, and G.D. Maxzwell, Elect. Lett., 25, 206, 1989.

Kaw83 M. Kawachi, M. Yasu, T. Edahiro, Electon. Lett., 19, 583, 1983.

Ker77 W. Kern, and R.S. Rosler, J. Vac. Sci. Tech., 14, 1082,

Ker79 W. Kern, G.L. Schnable, IEEE Trans. on Elect. Devices, Ed-2d, 4, 647, 1979.

Kim88 S.S. Kim, D.V. Tsu, and G. Lucovsky, J. Vac. Sci. Tech., A6, 1740, 1988.

Kin76 W.D. Kingery, H.K. Bowen, D.R. Uhlmann, Introduction to Ceramics, 2nd. ed., John Wiley & Sons, New York, 1976, p 666.

Kni76 Z. Knittl, Optics of Thin Films, Wiley, London, 1976.

Kog79 H. Kogelnik, in Integrated Optics, ed. by T. Tamir, Springer-Verlag, 1979.

Kog74 H.Kogelnik, and V. Ramaswamy, Applied Optics, 13, 1857, 1974.

Kom90 T. Kominato, Y. Ohmori, H. Okazaki, M. Yasu, Electron. Lett., 44, 222, 1990.

Lam81 D.K.W. Lam, and B.K. Garside, Appl. Opt., 20, 440, 1981.

Lan42 L.D. Landau, and B.G. Levich, Acta Phisiochim., URSS 17, 1942, 42.

Lee86 D.L. Lee, Electromagnetic Principles of Integrated Optics, John Wiley & Sons, New York, 1986, p 39.

Lev81 N. Levy, Appl. Opt., 20, 460, 1981.

Levy74 Y. Levy, C. Imbert, J. Cipriani, S. Racine, and R. Dupeyrat, Opt. Commun., 11, 66, 1974.

Les90 B. Lesche, J. Opt. Soc. Am. B, 7, 53, 1990.

Luc90 J.K. Lucek, R. Kashyap, S.T. Davey, and D.L. Williams, J. Mod. Opt., 37, 533, 1990.

Mac80 J.B. MacChesney, Proc. IEEE, 68, 10, 1181, 1980.

Mar64 E.A. Marcatili, and R.A. Schmeltzer, Bell Syst. Tech. J., 43, 1783, 1964.

Mat80 B. Mattson, Solid State Tech., 60, Jan., 1980.

Mat84 I. Matsuyama, K. Susa, S. Satoh, and T. Sugamura, Am. Ceram. Soc. Bull., 63, 1408, 1984.

Max89 G. Maxwell, R. Kashyap, G. Barbarrossa, Proc. of the 1st. Intern. Ceram. Sci. & Tech. Cong., Oct. 1989, Anahein, CA, USA.

McC71 B.J. McCarthy, R. Roy, and J.M. McKay, J. Am. Ceram. Soc., 54, 637, 1971.

McM88 P.F. McMillan, and A.M. Hofmeister, Reviews in Mineralogy, 18, 99, 1988.

Mea83 P. Meakin, Phys. Rev. Lett., 51, 1119, 1983.

Mim80 Y. Mimura, Y. Okamura, Y. Komazawa, and C. Ota, Jpn. J. Appl. Phys., 9, L269, 1980.

Mel89 G. Meltz, W.W. Morey, and W.H. Glenn, Opt. Lett., 14, 823, 1989.

Mil69 S.E. Miller, Bell Syst. Tech. J., 48, 2059, 1969.

Mit56 E.W.J. Mitchell, and E.G.S. Paige, Philos Mag., 1, 1085, 1956

Miz90a V. Mizrahi, Y. Hibino, and G.I. Stegeman, Opt. Comm., 1990 in press.

Miz90b V. Mizrahi, S. LaRochelle, G.I. Stegeman, and J.E. Sipe, submitted to Phys. Rev. A 1990.

Mor82 H. Mori, and N. Shimizu, IEEE J. of Quantum Electron., QE-18, 776, 1982.

Muk84 S.P. Mukherjee, Mat. Res. Soc. Symp. Proc., 32, 111, 1984.

Muk86 S.P. Mukerjee, and S.K. Sharma, J. of Am. Ceram. Soc., 69, 806, 1986.

Nat82 National Bureau of Standards Handbook, 140, Optical Waveguide Communications Glossary, U.S. Dept. of Commerce, 1982.

Nou86 N. Nourshargh, E.M. Starr, J.S. McCormack, IEE Proceedings, 133, Pt. J, 264, 1986.

Nou89 N. Nourshargh, E.M. Starr, T.M. Ong, Electrn. Lett, 25, 981, 1989.

Oka80 Y. Okamura, Y. Mimura, Y. Komazawa, and C. Ota, Jpn. J. Appl. Phys., 19, L649, 1980.

Ost86 U. Osterberg, and W. Margulis, Opt. Lett., 11, 516, 1986.

Ostr78 D.B. Ostrowsky, and C. Vanneste, Physics of Thin Films, 10, 227, 1978.

Pau60 L. Pauling, The Nature of the Chemical Bond, Cornell University Press, Ithaca, N.Y. 1960.

Pav86 C. Pavelescu, C. Cobianu, and E. Segal, Thin Solid Films, 140, 261, 1986.

Pay89 F.P. Payne, Elec. Lett., 25, 498, 1989.

Pha82 J. Phalippou, M. Prassas, and J. Zarzycki, J. Non-Cryst. Solids, 48, 17, 1982.

Phi82 J.C. Phillips, Solid State Phys., 37, 93, 1982.

Pit84 N.J. Pitt, and A. Marshall, Elect. Lett., 20, 512, 1984.

Ple84 K.W. Plessner, S.J. Stannard-Powell, Elect. Lett., 20, 250, 1984.

Poy90 P. Poyhonen, S. Honkanen, and A. Tervonen, Opt. Lett., 15, 21, 1206, 1990.

Puy82 R. Puyane, A.L. Harman, and C.J.R. Gonzalez-Oliver, Proc. 8th European Conf. on Optical Commun., Cannes, 623, 1982.

Pye72 L. Pye, H.J. Stevens, and W.L. LaCourse, Introduction to Glass Science, Plenum, New York, 1972, p 583.

Que88 F. Quellette, K.O. Hill, and D.C. Johnson, Opt. Lett., 13, 515, 1988.

Rad86 V.A. Radtsig, and A.A. Bobyshev, Phys. Stat. Sol.(B), 133, 621, 1986.

Ram89 V. Ramaswamy, Optical Fibers class notes, 1989.

Rau87 H. Rau, and W. Hermann, Ber. Bunsenges. Phys. Chem., 91, 833, 1987.

Rev83 A.G. Revesz, G.E. Walrafen, J. Non-Crystal. Solids, 54, 323, 1983.

Rie68 E.F. Riebling, J. of Am. Ceram. Soc., 51, 406, 1968.

Ros77 R.S. Rosler, Solid State Tech., 20, 63, 1977.

Row74 J.E. Rowe, Appl. Phys, Lett., 25, 576, 1974.

Roy56 R. Roy, J. Am. Ceram. Soc., 39, 4, 145, 1956.

Roy69 R. Roy, J. Am. Ceram. Soc., 52, 6, 344, 1969.

Sak80 S. Sakka, and Kamiya, J. Non-Cryst. Solids, 42, 403, 1980.

Sch68 E.R. Schineller, R.P. Flam, and D.R. Wilmot, J. Opt. Soc. Am., 58, 1171, 1968.

Sch74 R.V. Schmidt and I.P. Kaminow, J. Phys. Lett., 25, 258, 1974.

Sch69 H. Schroeder, Phys. Thin Films, 5, 87, 1969.

Sch73 J. Schroeder, R. Mohr, P.B. Mercedo, and C.J. Montrose, J. Am. Ceram. Soc., 56, 510, 1973.

Sch80 P.C. Schultz, Proc. IEEE, 68, 10, 1187, 1980.

sha81 S.K. Sharma, J.F. Mammone, and M.F. Nicol, Nature, 292, 140, 1981.

Sha84 S.K. Sharma, D.W. Matson, J.A. Philpotts, and T.L. Rough, J. of Non-Crystal. Solids, 68, 99, 1984.

Shi86 S. Shibata, T. Kitagawa, F. Hanawa, and M. Horiguchi, J. Non-Cryst. Solids, 88, 345, 1986.

Shin86 K. Shingyouchi, K. Konishi, K. Susa, and I. Matsuyama, Electron. Lett., 22, 2, 99, 1986.

Shr86 D.F. Shriver and M.A. Drezdzon, The Manipulation of Air-Sensitive Compounds, 2nd. ed., Wiley-Interscience, New York, 1986.

Sil84 A.R. Silin, P.J. Bray, and J.C. Mikkelsen, J. Non-Crystal. Solids, 64, 185, 1984.

Sim90 K.D. Simmons, S. LaRochelle, V. Mizrahi, and G.I. Stegeman, submitted to Opt. Lett. 1990.

Sim91 J.H. Simmons, R. Ochoa, and O.H. El-Bayoumi, to be published in Ultrastructure Processing, L.L. Hench and J.K. West, Eds., John Wiley and Sons.

Sim79 P.G.Simpkins, S. Greenberg-Kosinski, and J.B. MacChesney, J. Appl. Phys, 50, 5676, 1979.

Sku84 L.N. Skuja, A.N. Streletsky, and A.B. Pakovich, Solid State Comm., 50, 12, 1069, 1984.

Sny66 L.R. Snyder, Sep. Sci., 1, 191, 1966.

Sol81 R. Solanki, P.K. Boyer, J.E. Mahan, and G.J. Collins, Appl. Phys. Lett., 38, 572, 1981.

Sol83 R.Solanki, W.H. Ritchie, Appl., Phys. Lett., 43, 434, 1983.

Spr81 W.A. Sproson, K.B. Lyons, and J.W. Fleming, J. of Non-Crystalline, Solids, 45, 69, 1981.

Ste88 A.F. Stewart, D.R. Tallant, and K.L. Higgins, in Laser Induced Damage in Optical Materials, 362, National Bureau of Standards, 1988.

Sto68 W. Stober, A. Fink, and E. Bohn, J. Colloid. Interface Sci., 26, 62, 1968.

Sto70 R.H. Stolen, J.T. Krause, and C.R. Kurkjian, Disc. Faraday Soc., 50, 103, 1970.

Sto87 R.F. Stolen, and H.W.K. Tom, Opt. Lett., 12, 585, 1987.

Ston72 J. Stone, IEEE J. Quantum Electron., QE-8, 386, 1972.

Str68 K. Strater, RCA Review, 29, 618, 1968.

Suc88 P.G. Suchoski, T.K. Findakly, and F.J. Leonberger, Opt. Lett., 13, 11, 1050, 1988.

Sus82 K. Susa, I. Matsuyama, S. Satoh, and T. Suganuma, Electron. Lett., 18, 499, 1982.

Sus90 K. Susa, I. Matsuyama, S. Satoh, and T. Sugamura, J. Non-Crystal. Solids, 119, 21, 1990.

Tal88 D.R. Tallant, K.L. Higgins, and A.F. Stewart, Appl. Spectroscopy, 42, 326, 1988.

Tan84 S. Tanak, M. Kyoto, M. Watanabe, H. Yokota, Elect. Lett., 20, 283, 1984.

Tang80 G. Tangonan, A.G. Paster and R.C. Pastor, Appl. Opt., 12, 1110, 1980.

Tani71 E. Tanikawa, T. Okabe, and K. Maeda, Denki Kagaku, 41, 491, 1971.

Tani84 T. Tanifuji, M. Matsumoto, M. Tokuda, M. Miyauchi, Elect. Lett., 20, 13, 1984.

Tat86 A. Tate, K. Jinguji, T. Yamada, and N. Takato, J. Appl. Phys, 59, 932, 1986.

Tic90 P.A. Tick, P.L. Bocko, in Optical Materials: A Series of Advances, Vol. 1, ed. S. Musikant, Marcel Dekker, Inc., New York, 1990.

Tie71 P.K. Tien, Appl. Opt., 10, 2395, 1971.

Tie70 P.K. Tien, and R. Ulrich, J. of the Optical Soc. of Am., 60, 1325, 1970.

Tie72 P.K. Tien, G.S. Molinsky, and R.J. Martin, Appl. Opt., 11, 637, 1972.

Tie73 P.K. Tien, R.J. Martin, G. Smolinsky, Appl. Opt, 12, 1909, 1973.

Tob80 P.J. Tobin, J.B. Price, and L.M. Campell, J. Electrochem. Soc., 127, 10, 2222, 1980.

Toh89 R. Tohmon, H. Mizuno, Y. Ohki, K. Sasagane, K. Nagasawa, and Y. Hama, Phys. Rev. B, 39, 1337, 1989.

Tor91a W.E. Torruellas, The Optical Cubic Susceptibility Dispersion of Some Transparent Thin Films, PhD Dissertation, University of Arizona.

Tor91b W.E. Torruellas, L.A. Weller-Brophy, R. Zanoni, G.I. Stegeman, Z. Osborne, and B.J. Zelinski, Appl. Phys. Lett., to be published.

Tor91c The measurement and the analysis were conducted by W.E. Torruellas at the University of Arizona.

Tsa87 T.E. Tsai, D.L. Griscom, and E.J. Friebele, Diffusion and Defect Data, 53-54, 469, 1987.

Tsa89 T.E. Tsai, M.A. Saifi, E.J. Friebele, D.L. Griscom, and U. Osterberg, Opt. Lett., 14, 1023, 1989.

Ues84 N. Uesugi, Y. Murakami, C. Tanaka, Y. Ishida, Y. Mitsunaga, Y. Negashi, N. Uchida, Elect. Lett., 19, 762, 1983.

Uhl84 D.R. Uhlmann, B.J.J. Zelinski, and G.E. Wnek, in Better Ceramics Through Chemistry, ed. C.J. Brinker, D.E. Clark, and D.R. Ulrich, Elsevier, Sci. Pub., 1984.

Ulr70 R. Ulrich, J. of the Optical Soc. of Am., 60, 1337, 1970.

Ulr72 R. Ulrich, and H.P. Weber, Appl. Opt., 11, 2, 428, 1972.

Ulr73 R. Ulrich, and R. Torge, Appl. Opt., 12, 2901, 1973.

Vas72 M.J. Vasile, G. Smolinsky, J. Electrochem. Soc., 119, 45, 1972.

Vol88 M.B. Volf, Mathematical Approach to Glass, Elsevier 1988, p.223.

Wah75 G. Wahl, in Chemical Vapor Deposition, ed. J.M. Blocher Jr., H.E. Hintermann, and L.H. Hall, 5th Intern. Conf., 1975 Electrochem. Soc. Prinston, NY).

Wal80 K.L. Walker, F.T. Geyling, and S.R. Nagel, J. of Amer. Ceram. Soc., 63, 552, 1980.

Web78 M.J. Weber, D. Milan, and W.L. Smith, Opt. Eng., 17, 1978, 463.

Yin82 Z.Y. Yin, and B.K. Garside, Appl. Opt., 21, 4324, 1982.

Yin83 Z. Yin, P.E. Jessop, and B.K. Garside, Appl. Opt., 22, 24, 4088, 1983.

Yol75 B.E. Yoldas, Bull. Am. Ceram. Soc., 54, 286, 1975.

Yol80 B.E. Yoldas, Appl. Opt., 19, 1425, 1980.

Yu72 T.Y. Yu, T.M. Cheng, V. Kempter, and F.W. Lampe, J. Phys. Chem., 76, 3321, 1972.

Yue82 M.J. Yuen, Appl. Opt., 21, 136, 1982.

BIOGRAPHICAL SKETCH

Din-Guo Chen was born January 11, 1959, in Taipei, Taiwan. After graduating from I-Lan high school, he attended National Cheng-Kung University where he studied metallurgy and materials science. After he was awarded a B.S. in August 1981, he served in the army for 2 years.

He began his graduate studies at the University of Florida in the spring 1985 and earned a Master of Science degree in materials science and engineering in August, 1987. He continued to work for his doctorate degree since then and is now working to complete the final requirements necessary to obtain the PhD degree in materials science and engineering.

He is a member of the American Ceramic Society, the Materials Research Society, the Optical Society of America, and the Society of Photo-Optical Instrumentation Engineers.

I certify that I have read this study and that in my opinion it conforms to acceptable standards of scholarly presentation and is fully adequate, in scope and quality, as a dissertation for the degree of Doctor of Philosophy.

Joseph H. Simmons, Chairman
Professor of Materials Science
and Engineering

I certify that I have read this study and that in my opinion it conforms to acceptable standards of scholarly presentation and is fully adequate, in scope and quality, as a dissertation for the degree of Doctor of Philosophy.

David B. Tanner
Professor of Physics

I certify that I have read this study and that in my opinion it conforms to acceptable standards of scholarly presentation and is fully adequate, in scope and quality, as a dissertation for the degree of Doctor of Philosophy.

John J. Mecholsky
Professor of Materials Science
and Engineering

I certify that I have read this study and that in my opinion it conforms to acceptable standards of scholarly presentation and is fully adequate, in scope and quality, as a dissertation for the degree of Doctor of Philosophy.

David E. Clark
Professor of Materials Science
and Engineering

I certify that I have read this study and that in my opinion it conforms to acceptable standards of scholarly presentation and is fully adequate, in scope and quality, as a dissertation for the degree of Doctor of Philosophy.

Kevin S. Jones
Assistant Professor of Materials Science and Engineering

This thesis was submitted to the Graduate Faculty of the College of Engineering and to the Graduate School and was accepted as partial fulfillment of the requirements for the degree of Doctor of Philosophy.

August, 1991

for Winfred M. Phillips
Dean, College of Engineering

Madelyn M. Lockhart
Dean, Graduate School